# MODELING VALVELESS PUMPING MECHANISMS

Austin J Baird

A dissertation submitted to the faculty at the University of North Carolina at Chapel Hill in partial fulfillment of the requirements for the degree of Doctor of Philosophy in the Department of Mathematics.

Chapel Hill
2014

Approved by:

Laura Miller

David Adalsteinsson

Peter Mucha

Greg Forest

Brian White

Lindsay Waldrop

# ABSTRACT

Austin J Baird: Modeling valveless pumping mechanisms
(Under the direction of Laura Miller)

Several mechanisms of valveless pumping are studied numerically. The discussion begins with an introduction into the two well-known driving mechanisms of flow in valveless tubes: impedance pumping and peristalsis. Flow generated from peristalsis and impedance pumping is examined using the immersed boundary method. Previous research has shown that impedance pumping, also known as dynamic suction pumping, produces bidirectional flows. This change in direction is dependent upon pumping frequency, the position of the actuation point, and several other parameters. In this thesis, I investigate the direction and magnitude of flow as a function of the Womersley number and the diameter to length ratio of the flexible portion of the tube. The diameter to length ratio has a significant effect on the overall net flow rate and direction. This type of sensitivity is not seen in peristalsis where the average net flow is determined by direction and speed of the contraction wave. Variations in Womersley number are used to determine at what scales peristalsis and dynamic suction pumping are effective. For the parameters considered, valveless suction pumping does not generate significant flow for Womersley numbers less than 1.

In the second part of the thesis, the flow direction of impedance pumping as a function of tube diameter and pumping frequency is examined in more detail. Impedance pumping, is a mechanism that has been speculated to be the driving force behind the uni-directional flow present in the vertebrate embryonic heart. Although the bidirectional nature of this mechanism is something that has been described in experimental and computational studies, no well established explanation has been offered for why changes in flow direction are seen for certain parameters choices. We will address the bidirectional nature of this mechanism by investigating flow direction as a function of the ratio of the tube diameter to length and the elastic properties of the tube. Direct numerical simulations of the fully-coupled fluid-structure interaction problem will be used to determine the magnitude and direction of fluid flow as a function of these parameters. The diameter to length

ratio has a strong effect on the direction of flow when all other parameters are held fixed. The resonant frequency of the tube, based upon the elastic properties of the model and the added mass of the fluid, is also investigated. Resonance of two separate sections of the tube divided by the compression region can govern the resulting direction of flow if the tube is driven at the resonant frequency of one of the sections. Understanding the bi-directional nature of this popular pumping mechanism is important in the design of micro-fluidic pumps as well as the understanding of the structure and function of valveless hearts.

In the third part of the thesis more the surrounding structures and properties of actual tubular hearts are used to improve my model of valveless pumping. I will focus on the tubular, valveless heart of the chordate, *Clavelina picta.* These hearts operate at a Womersley number of about 0.3. We investigate traditional impedance pumping on these small scales and show computationally and experimentally that significant flow is not achieved. We propose a different pumping mechanism that couples traveling waves of depolarization to the contraction of the boundary. Active contractile waves replace passive elastic waves, but the resulting kinematics are similar to dynamic suction pumping. This pumping mechanism can be computationally shown to drive fluid flow at the low Womersley numbers found in *Clavalina picta* hearts.

To my mother.

## ACKNOWLEDGMENTS

I'd like to begin with an exceedingly large thank you for my thesis advisor Laura Miller. I still remember her calling me on the phone convincing me to attend the program at UNC. It's really that phone call which changed my life immensely. I would be lying to myself and others if I didn't mention that I wouldn't be able to be where I am today without her guidance and support throughout my five years as a graduate student. I'm also very grateful to all the support of Richard Mclaughlin and Roberto Camassa who both helped me pass my first major milestone at UNC. I'd also like to thank all the other teachers and faculty at UNC I've had the pleasure to learn from in my time here.

I'd also like to thank my entire committee: Bill Kier for his Biological guidance in my applied thesis, David Adalsteinsson who literally taught me how to program, Peter Mucha who helped me be a better teacher and mentor, Greg Forest who brought me here and believed in my abilities, and Brian White for being such a willing participant at such short notice. My mind has been shaped for the better through the guidance of these people and I cannot thank them enough for it.

My mom and family have also been a great and dear support for me though my time here at UNC. I think that my mom's struggles are what led me to where I am today. There's truly no perfect way to convey my gratitude towards her. She supported me in everything I've ever attempted in my life. I'd also like to thank the rest of my friends and family, too numerous to mention here, who have cheered for me every step of the way.

# TABLE OF CONTENTS

# LIST OF FIGURES

# LIST OF TABLES

# CHAPTER 1: INTRODUCTION

Several mechanisms of valveless pumping will be numerically investigated in this thesis with a focus on flow generation at small scales. In the first section, peristalsis will be compared to dynamic suction pumping over a range of scales relevant to tubular hearts. In the second section, the bidirectional nature of dynamic suction pumping will be investigated with a focus on driving the tube at the resonant frequencies. In the third section, the pumping models will be improved by the addition of structure such as the pericardium and by triggering contraction waves using models from electrophysiology.

Dynamic suction pumping, also known as impedance pumping has recently been preposed as the mechanism by which he vertebrate embryonic heart drives the flow of blood [11]. This mechanism has a long history of study as a general fluid dynamic mechanism. Numerous mathematical and experimental tidies have built the groundwork for its use as a valveless pumping mechanism [24; 26; 25; 2; 20; 19]. Impedance pumping essentially requires an elastic tube attached to a more rigid structure at each end with an off-center actuation site. Although recent work suggests that embryonic and other tubular hearts use this pumping mechanism, little work to date has explicitly addressed scaling effects relevant to the size of the actual tubular hearts. The primary focus of this thesis is to consider these scales and explore alternative pumping mechanisms.

## 1.1 Outline

To begin we will discuss previous research related to the fluid dynamics of impedance pumping and peristalsis in general. In chapter 2, a description of the numerical method used to solve the fully-coupled fluid-structure interaction problems considered in this thesis will be provided. In chapter 3 we begin by investigating impedance pumping for small scale (low Womersley number) fluid dynamics and analyze its viability as a mechanism for driving flow in ing tubular hearts. Net flows generated by impedance pumping will be compared to those generated by peristalsis at similar scales.

In chapter 4, we will further explore the bi-directional nature of the impedance pumping mechanism and determine how the flow directions depends upon geometry and elastic properties. Specifically we will consider how the direction of net flow depends upon the diameter to length ratio of the elastic tube and the resonant frequencies of various sections of tube.

In chapter 5, we integrate some of the neuromechanical properties of the actual heart into our numerical model. In doing so we will create a new type of pumping mechanism. We will test this mechanism at the low Womersley numbers found in invertebrate and embryonic vertebrate heart tubes. We will then add a rigid boundary around the pumping region to mimic the stiff pericardium that surrounds heart tubes in most chordates.

## 1.2   Impedance Pumping and Peristalsis

Valveless hearts play a crucial role in transporting fluid throughout the circulatory system. This transport of fluid and other materials happens on a large range of scales, from the embryonic heart on the order of microns to the salp heart on the order of millimeters or centimeters. In the early stages of cardiac morphogenesis, vertebrates use valveless pumping to transport blood through the developing circulatory system [4; 29]. Valveless tubular hearts are also found in many invertebrates, such as urochordates and cephalochordates [33]. This diversity of invertebrate and vertebrate tubular hearts leads to a large range of scales in which fluid is transported effectively. Two major valveless pumping mechanisms, peristalsis and dynamic suction pumping, have been proposed as methods by which blood is driven. these two mechanisms will be studied over a range variety of Womersley numbers, $Wo$, and tube diameters, $d$. Here we define the Womersley number to be $Wo = r\sqrt{\frac{\omega}{\nu}}$, or the ratio of unsteady affects to viscous affects in pulsatile flow.

Peristalsis has long been studied as a basic transport mechanism for many tubular smooth muscle structures [36]. This pumping mechanism is known to be robust over a range of scales and is used in many medical and biological applications. For example, peristalsis moves the contents of the ureters and gastrointestinal tract in humans [8]. In terms of nonbiological applications, medical drug administration devices also use peristaltic pumps to deliver fluid at consistent low flow rates. Peristalsis is most simply defined as an active wave of contraction traveling down the length of the tube. For many biological pumps, the compressed portion of the tube achieves almost complete

occlusion allowing the traveling contraction to force the contents down its length. Peristalsis typically moves the contents of the tube at an average velocity on the order of the speed of the contractile wave [23]. Various computational studies have also focused on the dynamics of peristaltic pumping. Fauci et al. has shown peristaltic transport to be effective at propelling solid particles through a channel when the compression wave is near full occlusion of the channel [9]. Others have simulated peristaltic pumping for an elastic tube filled with a viscoelastic fluid [16] and explored the parameter space of Weissenburg numbers and occlusion ratios [6].

Another prominent pumping mechanism which has garnered a great deal of interest is the dynamic suction pump which was first studied by Liebau [24; 26; 25]. This pumping mechanism is most simply defined by an isolated region of active contraction that is asymmetrically located in a section of flexible tube with stiffer ends. The flexibility of the tube allows the transport to be augmented by passive elastic traveling waves generated from the active contraction site. These traveling waves are reflected upon contact with the more rigid connections, see figure 1.3.1. Since Liebau's work, analytical models of dynamical suction pumping have been developed by Auerbach et al. [2] and Bringley et al. [3]. Physical experiments by Hickerson et al. [13] and Bringley et al. [3] support that this pumping mechanism can effectively transport fluid under certain conditions. Finally, numerical simulations by Jung and others [20; 19] show that this is a viable mechanism for certain parameters and detail the complex relationship between pumping frequency and flow direction. The vast majority of these studies, however, have focused on $Wo > 1$.

One of the characteristic properties of dynamic suction pumping is the nonlinear relationship between pumping frequency and volumetric flow rate. Other interesting properties include the directional dependence on the pumping frequency and the generation of bidirectional waves from the region of active contraction. Experimental studies by Forouhar et al. [11] suggest that the zebrafish embryonic heart is a dynamic suction pump since experimental data show a nonlinear frequency-flow relationship. Further support was due to the observation that a bidirectional wave of contraction emanates from the pacemaker region.

One of the primary purposes of this thesis is to explore the relationship between Womersley number and the magnitude and direction of flow, particularly for $Wo < 1$. The significance of this choice stems from the fact that biological applications of tubular pumping span a range of scales larger than what has typically been studied. For example, many invertebrates have tubular valveless
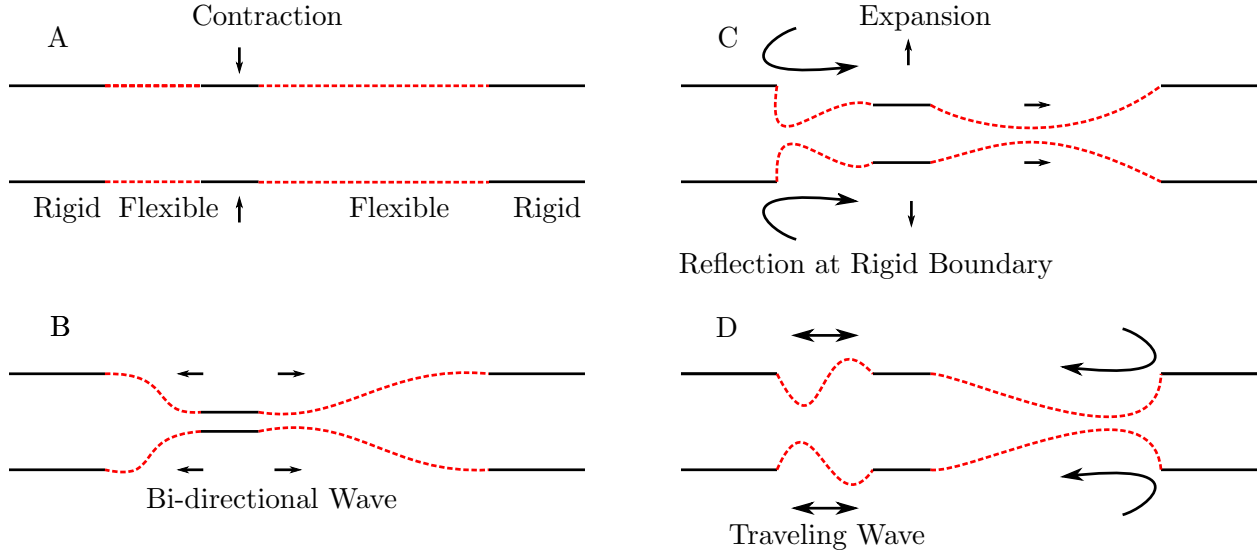
Figure 1.3.1: Impedance pumping shown in panels A-D. Compression begins in A and the bi-directional traveling waves are dispersed from the compression region at B. These traveling waves are reflected at each rigid boundary in panels C and D.

hearts [21], and these organisms span the range from small sea squirts with hearts on the order of tens to hundreds of microns ($Wo < 1$) to salps hearts on the order of millimeters ($Wo > 1$). The vertebrate embryonic heart grows from a valveless tube on the order of tens of microns ($Wo < 1$) to a large four chambered pump on the order of centimeters ($Wo > 1$) [35]. Diameters found in medical applications using peristaltic pumps also range from fractions of a millimeter to tens of centimeters. This range of Womersley numbers lends itself well to a numerical study of pumping mechanisms using the immersed boundary method.

## 1.3    Introduction to Impedance Pumping Reversals

One of the least understood properties of impedance pumping are the changes in the direction of the fluid flow. This phenomenon was first studied by Leibau [24], when he showed that a periodic contraction at a location antisymmetric with respect to a flexible tube generated net flow. In 2001 Jung and Peskin[20] used numerical simulations to show that the frequency of pumping had a dramatic effect upon the magnitude as well as the direction of fluid flow for a fixed tube geometry and fixed elastic properties. They also noted that the tube resonated at certain frequencies but did not calculate the resonant frequency. The effects of resonating the elastic section was further investigated by Gharib et al. [15; 22] using a numerical method to solve the fluid-structure interaction problem.

4

They fixed the tube geometry and calculated the resonant frequency by calculating the frequency of free vibration of the entire tube. Their model was matched to previous experimental investigations by Hickerson in 2006, where fluid velocity and pressure data was collected for various parameters including: location of actuation site, frequency of pumping, and amplitude of pumping [13]. For a fixed tube geometry and fixed elasticity of the tube, they found that the maximum flow rate occurred at the resonant frequency of the system and mentioned that flow reversals occur as a function of pumping frequency. Also using numerical simulations of the fluid-structure interaction problem, Baird et al. found that the $Wo$ and the ratio of the tube diameter to the length of the pumping region had a strong effect upon flow direction [1]. The $Wo$ number in their investigations was changed by altering the viscosity of the fluid and the elastic properties and pumping frequency remained fixed.

The direction of net flow has also been described using analytical models. Ottersen et. al. developed a one dimensional model of an impedance pump [30]. Like the studies from Jung and Peskin they were able to determine that flow direction was a function of pumping frequency but did not investigate the resonant properties of the elastic tube. A similar study done by Manopoulos et al. determined that flow direction was a function of frequency for fixed geometries and elastic properties [5]. They computed the natural frequency for the entire flexible tube through a free vibration experiment, exciting the tube and recording the damped vibrations. They noted that the fixed maximum flow rate was achieved near the resonant frequency of their experiment when all other parameters were fixed. They also found, similar to Jung and Peskin, that the flow direction was a function of compression location along the flexible tube for fixed pumping frequencies. Bringley et al. was not able to produce flow reversals in their analytical model, but did note that flow reversals existed in their experimental model [3].

Impedance pumping has been proposed as the driving mechanism of valveless tubular hearts such as the zebrafish embryonic heart [11]. It has also been used in engineering applications as a noninvasive microfluidics pump. A feature of this pump which has been difficult to predict is the presence of flow reversals for certain parameter choices. Some organisms rely on uni-direction flow in their vascular systems, and flow reversals can damage or even death. In an engineered system, changes in the direction of flow could cause catastrophic events. Medical pumps used for drug delivery are often in operation for long periods of time to administer a specific amount of drug.

Flow reversals due to changes in the system such as the pressure jump could result in an overdose of medicine, or an absence of the drug. To better understand how flow direction is determined, we will present a comprehensive numerical study investigating how the different resonant frequencies of the two separated elastic tube regions, $\alpha_1$ and $\alpha_2$, see figure 4.1.1, determine the resulting flow direction. We will also investigate how the non-dimensional length ratio $\hat{\mathcal{L}} = $ (elastic length)/(tube diameter) affects the flow direction. The immersed boundary method will be used to solve the resulting fluid-structure interaction problem.

## CHAPTER 2: NUMERICAL METHODS

To begin the discussion of some of the questions that will be addressed in this thesis, we need to first introduce the numerical method used to solve the fluid-structure interaction problem. Since we will be considering the effectiveness of various pumping mechanisms, it is necessary to model a flexible tube moving in a fluid, with the resulting movement driving the flow. This type of problem calls for a coupling of the boundary generated forces to the forcing term in the Navier Stokes equations. We will use the immersed boundary method to solve these fully-coupled fluid-structure interaction problems. In this section we will introduce some of the details of this method and discuss how to model a simple tubular pump. Full details of the method, can be found in appendix A with a full discussion of the numerical implementation in appendix B.

## 2.1   Scaling

Both the Reynolds number ($Re$) and the Womersley number ($Wo$) have been used to discuss scaling effects in fluid dynamics including mechanisms of fluid transport. Jaffrin and Shapiro [17] discuss analytical results of peristaltic pumping in terms of the $Re$, and Jung and Peskin [20] numerically studied dynamic suction pumping for $Re$ in the range of 0 to 160. For consistency, this thesis will focus on $Wo$, but the two dimensionless parameters can be related (see below).

The $Re$ appears in the non-dimensional form of the Navier-Stokes equations,

$$\frac{\mathbf{u}}{t} + \mathbf{u} \cdot \nabla \mathbf{u} = -\nabla p(\mathbf{x}, t) + \mu U l \rho \nabla^2 \mathbf{u} + \mathbf{f}(\mathbf{x}, t), \tag{2.1}$$

$$\nabla \cdot \mathbf{u} = 0. \tag{2.2}$$

Table 2.1: Tubular heart parameters. Here d.p.f stands for days post fertilization, HH represents the Hambuger-Hamilton stage of chicken embryo development, and d.p.c. stands for days post conception [12]. Peak flow rates and maximum diameters of the heart were used in the calculations. It was assumed that the dynamic viscosity of the blood was 0.003 N s/m2, and the density of the blood was 1025 kg/m3. Note that the calculation of the dimensionless numbers is sensitive to the choice of the characteristic length, velocity, viscosity, and density. These calculations may be different than those reported in the references.

| Species | Flow rate (mm/s) | Diameter (mm) | Frequency (Hz) | Wo | Re |
|---------|------------------|---------------|----------------|-------|-------|
| Zebrafish, 26 h.p.f. [11] | 1 | 0.05 | 2.3 | 0.111 | 0.017 |
| Zebrafish, 4.5 d.p.f. [18] | 10 | 0.1 | 2 | 0.207 | 0.342 |
| Chicken, HH15 [12] | 26 | 0.2 | 2 | 0.414 | 1.777 |
| Chicken, HH18 [12] | 170 | 0.14 | 2 | 0.172 | 4.82 |
| Mouse, 8.5 d.p.c. [7] | 3 | 0.075 | 2.8 | 0.184 | 0.077 |
| Mouse, 9.5 d.p.c. [7] | 4 | 0.125 | 2.1 | 0.265 | 0.171 |
| Mouse, 10.5 d.p.c. [7] | 4 | 0.15 | 2.4 | 0.340 | 0.205 |
| Ciona intestinalis [21] | 5 | 2 | 0.55 | 0.9 | 3.3 |

where $\mathbf{u}$ is the fluid velocity at position $x$ and time $t$, $p$ is the pressure, $\mu$ is the dynamic viscosity of the fluid, $l$ is the characteristic length scale, $U$ is the characteristic velocity, $\rho$ is the density of the fluid, and $f$ is the body force. Once the fluid equations have been non-dimensionalized the Reynolds number is identified to be

$$Re = Ul\rho\mu. \tag{2.3}$$

To study the scaling effects of pulsatile flows, it is generally more convenient to use the another dimensionless number that takes into account the frequency of pumping. Such a number number is the Womersley number, which characterizes the pulsatile nature of the flow [39]. The Womersley number $(Wo)$ is defined to be

$$Wo = a\sqrt{\omega\nu}, \tag{2.4}$$

8

where $a$ is the radius of the tube, $\omega$ is the frequency of the pulsatile flow, and $\nu = \mu\rho$ is known as the kinematic viscosity. In general, unsteady effects are significant for $Wo > 1$ and are negligible for $Wo < 1$. The $Wo$ can be directly related to $Re$ by choosing the characteristic velocity and length appropriately. We can define the characteristic velocity of the system to correspond to the velocity of the oscillating structure using the relation $U = \omega a$. Plugging this into the formula for the $Re$ results in $Wo \sim \sqrt{Re}$. Using this definition, we can see that $Wo$ is also proportional to the ratio of unsteady inertial forces to viscous forces. Note that as viscosity is increased, or the radius of tube becomes smaller, $Wo$ becomes smaller. For example, $Wo$ ranges from as large as 20 in the aorta to as small as $10^{-2}$ in the capillaries.

To have a better understanding of how scaling and geometry affect fluid flow, this thesis will investigate several orders of magnitude of $Wo$ using direct numerical immersed boundary simulations of peristalsis and dynamic suction pumping. We will also investigate how the ratio of tube diameter to length affects fluid transport in both pumping mechanisms. The need to have a broad understanding of these pumping mechanisms is important to all manor of applications involving valveless tubular fluid transport. Specific questions to be addressed include: 1) At what scales does dynamic suction pumping generate significant net flow? 2) What diameter to length ratio is the most effective at moving fluid for a given set of parameters? 3) What is the direction of flow across $Wo$ and for various diameter to length ratios?

## 2.2   Immersed Boundary Method

The immersed boundary method was first developed by Peskin [31] as a means to deal with the interaction between an elastic boundary and the fluid in which it is immersed. Since its original development, a number of other methods have been used to handle the fully-coupled fluid structure interaction problem in a similar way [28]. The method works well at a variety of scales found below the turbulent regime, making it useful in many biological applications. Some of these applications include swimming organisms in viscoelastic fluid [37], insect flight [27], and lamprey swimming [38].

The immersed boundary method handles the problem of having an elastic boundary immersed in an incompressible viscous fluid by using two separate but interactive coordinate frames. The incompressible fluid is discretized on a fixed Cartesian grid (Eulerian frame) and the moving elastic

boundary is discretized on a moving curvilinear mesh (Lagrangian frame). The deformation of the boundary generates a force which is imparted to the surrounding fluid. The fluid is then driven by this force, and the boundary moves at the local fluid velocity.

The governing equations for the fluid are defined by the full 2D Navier-Stokes equations given by

$$\rho \left( \frac{\mathbf{u}}{t} + \mathbf{u} \cdot \nabla \mathbf{u} \right) = -\nabla p(\mathbf{x}, t) + \mu \nabla^2 \mathbf{u} + \mathbf{f}(\mathbf{x}, t), \tag{2.5}$$

$$\nabla \cdot \mathbf{u} = 0, \tag{2.6}$$

Equation 2.5 is the momentum equation for a fluid, and equation 2.6 defines the incompressibility of a constant density fluid.

The forcing term $\mathbf{f}(\mathbf{x}, t)$ is particular to the application and may include resistance to bending, resistance to stretching, displacement from a tethered position, the action of virtual muscles, or external forces [31]. One of the simplest types of force is a penalty force that is proportional to the displacement of the immersed boundary from a target boundary or preferred position. This target boundary could be fixed or could move with a prescribed motion. The position in Cartesian coordinates of the immersed boundary that interacts with the fluid is given by $\mathbf{X}(s, t)$. Here $s$ describes the position of the boundary along its length. To move the boundary in a preferred motion, target points are given Cartesian coordinates that may change in time defined by $\mathbf{Y}(s, t)$. When the immersed boundary points deviate from the preferred position, a force is applied that is proportional to the distance between the target and actual boundaries. This force can be adjusted by changing the magnitude of $k_{target}$ so that the distance between the actual boundary and its preferred configuration is kept within some tolerance. Another way to think about the target boundary is to assume that springs of stiffness $k_{target}$ connect the actual boundary to the target boundary. The force that results follows Hooke's law, describing force generated by a linear spring, and is defined to be:

$$\mathbf{F}_{target}(s,t) = \kappa_{target}(\mathbf{Y}(s,t) - \mathbf{X}(s,t)). \tag{2.7}$$

In addition to the target force, forces may also be generated through the elastic properties of the boundary. For this application, every boundary point along the tube is connected by a series of beams and springs which resist bending and stretching, respectively. These additional forces can be calculated as

$$\mathbf{F}_{beam}(s,t) = \kappa_{beam}{}^4 \mathbf{X}(s,t) s^4, \tag{2.8}$$

$$\mathbf{F}_{spring}(s,t) = \kappa_{spring} \left\{ (|\mathbf{X}(s,t)s| - 1) \, \mathbf{X}(s,t)/s|\mathbf{X}(s,t)/s| \right\}. \tag{2.9}$$

Equation 2.8 is the beam equation which describes the force generated due to the resistance to bending, and $\kappa_{beam}$ is the corresponding coefficient of stiffness. Equation 2.9 describes the force resulting from the tube's resistance to stretching and compression, and $\kappa_{spring}$ is the corresponding spring coefficient. A summation of all three forcing terms is then used to describe the total force applied to the fluid due to the boundary. This force is defined to be

$$\mathbf{F}(s,t) = \mathbf{F}_{target}(s,t) + \mathbf{F}_{beam}(s,t) + \mathbf{F}_{spring}(s,t). \tag{2.10}$$

To spread this force to the surrounding fluid defined in the Eulerian frame, Equations 2.5 and 2.6 are coupled to the boundary equations using integral transforms with delta function kernels:

$$\mathbf{f}(\mathbf{x},t) = \int \mathbf{F}(s,t)\delta(\mathbf{x} - \mathbf{X}(s,t))ds \tag{2.11}$$

$$\frac{\mathbf{X}}{t} = \mathbf{u}(\mathbf{X}(s,t),t) = \int \mathbf{u}(\mathbf{x},t)\delta(\mathbf{x} - \mathbf{X}(s,t))d\mathbf{x}. \tag{2.12}$$

To numerically approximate these integral transforms, a regularized delta function, $\delta_h$, is used,

$$\delta_h(\mathbf{x}) = 1h^2\phi\left(xh\right)\phi\left(yh\right), \tag{2.13}$$

where $h = dx$ the numerical mesh width. Here we can define $\phi(r)$ as

$$\phi(r) = \begin{cases} 14(1 + \cos(\pi r2)) & |r| \leq 2 \\ \\ 0 & otherwise \end{cases} \tag{2.14}$$

A more detailed discussion of this function is found in Peskin [31]. The smoothed approximation to the force density is now defined in the Eulerian frame as $\mathbf{f}(\mathbf{x},t)$. The forces created through deformations of the boundary are now influencing the fluid. To numerically solve the fluid equations, equations 2.5 and 2.6 are discretized on a periodic $630 \times 630$ grid and solved using a fast Fourier transform fluid solver, details of which can be found in Peskin and McQueen [32]. Once the fluid velocity is calculated, a discretization of equation 2.12 with the regularized delta function is used to interpolate the local fluid velocity to the Lagrangian boundary points. This effectively enforces a no-slip condition at the boundary. Once the new position of the boundary is updated, one time-step of the immersed boundary routine is concluded.

## 2.3   Modeling

To effectively investigate the two pumping mechanisms at various scales, a numerical model of the tube must first be constructed. For comparison with previous analytical, numerical, and

experimental work, the computational immersed boundary will resemble a closed racetrack. The section of tube where the contraction occurs will be flexible, and the remainder of the racetrack will be relatively rigid, see figure 2.3.1. The racetrack is constructed by connecting two half circles to two straight portions of tube. These circles are off center with radii set so that the diameter of the channel is equal throughout. The circular sides and the top of the racetrack will be tethered to target points so that they are relatively rigid. The bottom straight portion of the racetrack resists bending and stretching with no tether points so that the boundary can move freely. To describe the curved regions of the tube, we will define the inner radius to be $R_2$, the outer radius to be $R_1$, and the horizontal shift as $r_i$, see figure 2.3.1. The half circles can then be constructed by setting the $(x, y)$ coordinates as

$$(x, y) = \begin{cases} (R_2 \cos(\theta), R2 \sin(\theta) \pm r_i) & r = R_2 \\ \\ (R_1 \cos(\theta), R_1 \sin(\theta) \pm r_i) & r = R_1 \end{cases} \tag{2.15}$$

With the $\pm$ indicating which side of the tube you are describing. Note that the horizontal shift is the same distance as to the bottom straight tube. Also note the $\theta \in (-3\pi 2, \pi 2)$ for the right hand portion of the tube and $\theta \in (\pi 2, -3\pi 2)$ for the left hand portion. The racetrack is immersed in a incompressible viscous fluid with constant density $\rho$ and viscosity $\mu$ in a periodic square domain.

With this configuration immersed in the fluid, peristalsis and dynamic suction pumping may be implemented as the mechanisms driving flow using moving target points in the active region of contraction as described in the next section. Relevant physical and numerical parameters are summarized in Tables 2 and 3.
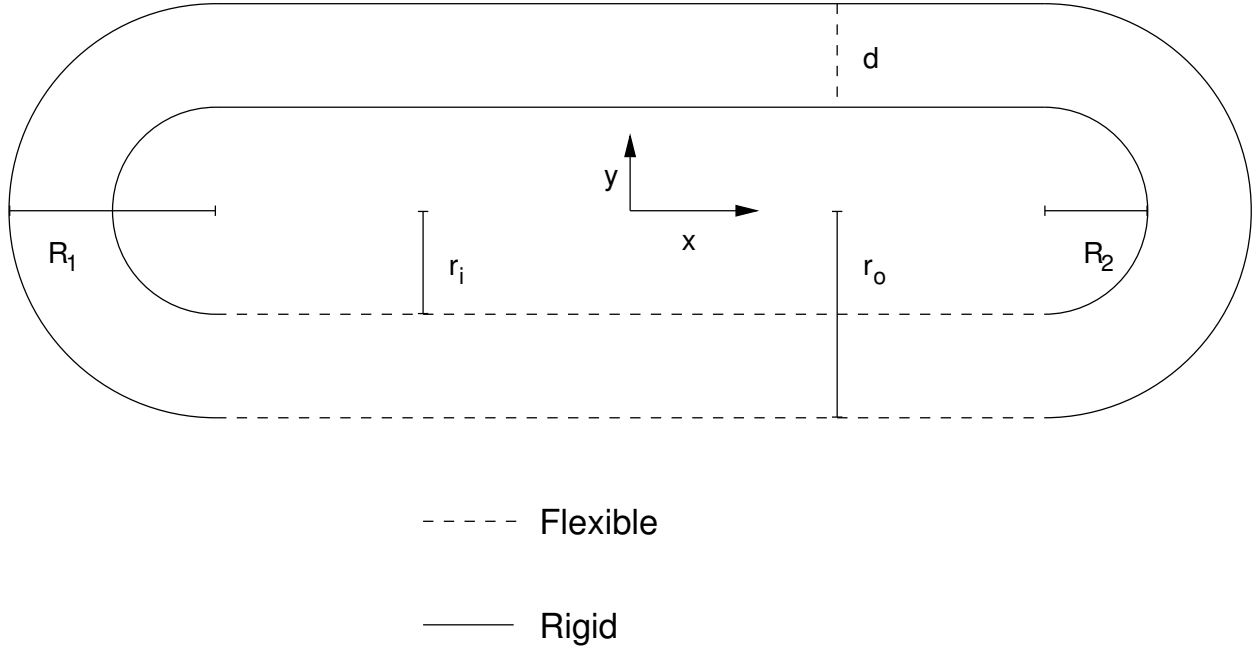
Figure 2.3.1: Model of a closed valveless racetrack. Dotted portions identify flexible regions and solid lines indicate rigid regions. Pumping mechanics are implemented along the flexible section denoted by dotted lines. $R_2$ is the inner radius, $R_1$ is the outer radius, $d$ is the diameter, $r_i$ is the distance to the inner straight tube from the origin (and also the distance to the center of the offset circular regions), $r_o$ is the distance from the origin to the outer straight portion of the tube.

Table 2.2: Spatial dimensions and numerical parameters for the heart tube simulations. These are dimensional parameters used to simulate impedance pumping and peristalsis to investigate scaling effects on pumping efficacy.

| Parameter | Value |
|---|---|
| Length of domain (m) | 0.0005 |
| Width of domain (m) | 0.0005 |
| Diameter of tube [$d$] (m) | prescribed |
| Outer radius [$R_1$] (m) | 0.0001 |
| Inner radius [$R_2$] (m) | R1 - diameter |
| Distance to inner straight tube [$r_i$] (m) | 0.000125 |
| Distance to outer straight tube [$r_o$] (m) | 0.000125 + d |
| Length of straight tube (m) | 0.00025 |
| Frequency of pumping ($1s$) | 2.3 |
| Percent of contraction | 0.8 |
| Pulse Period (s) | 0.43 |
| Final simulation time (s) | 4 |
| Time step [$dt$] (s) | 0.00003047619 |
| Velocity output time step (s) | 0.025 |
| Spatial step [$dx$] (m) | 8.33333333e-7 |
| Boundary step [$ds$] (m) | 4.16666667e-7 |

Table 2.3: Mechanical variables for the heart tube simulations.

| Parameter | Value |
|---|---|
| Density of the fluid $[\rho]$ $(kgm^3)$ | 1025.0 |
| Viscosity of the fluid $[\mu]$ $kgsm$ | prescribed |
| Bending coefficient of the boundary $[\kappa_{beam}]$ $(Nm^2)$ | 3240000 |
| Stretching stiffness of the boundary $[\kappa_{spring}]$ $(kgs^2)$ | 3240000 |
| Stretching stiffness of target points $[\kappa_{target}]$ $(kgs^2)$ | 3240000 |

**CHAPTER 3:   IMPEDANCE PUMPING VS. PERISTALSIS ACROSS RE**

Flow generated from peristalsis and dynamic suction pumping is examined using numerical simulations. Previous research has shown dynamic suction pumping to be bidirectional. This change in direction is dependent upon pumping frequency, the position of the actuation point, and several other parameters. This thesis investigates the direction and magnitude of flow as a function of the Womersley number and the diameter to length ratio of the flexible portion of the tube. The diameter to length ratio has a significant effect on the overall net flow rate and direction. This type of sensitivity is not seen in peristalsis where the average net flow is determined by contraction wave speed. Variations in Womersley number are used to determine at what scales peristalsis and valveless suction pumping are effective. For the parameters considered, valveless suction pumping does not generate significant flow for Womersley numbers less than 1.

## 3.1   Peristalsis

To simulate peristaltic motion, the tube is first tethered entirely to target points. All movement in the tube is prescribed and the peristaltic wave is created using three distinct motions: the initial contraction, the translation of the contracted region, and decompression. The contraction begins on the left hand side of the straight tube in the lower section of the racetrack, see figure 3.1.1. The $y$ values for the inner and outer sections of the tube are given by the functions:

$$Y_T^i(x,t) = r_i + \alpha g(x,t) 2 \sin\left(2\pi(x - \tilde{g}(t))\beta - \pi 2\right), \tag{3.1}$$

$$Y_T^o(x,t) = r_o - \alpha g(x,t) 2 \sin\left(2\pi(x - \tilde{g}(t))\beta - \pi 2\right). \tag{3.2}$$

Here, $Y_T^i(x,t)$ and $Y_T^o(x,t)$ correspond to the y inner and y outer target points respectively, $d$ is the diameter of the tube, $\alpha$ sets the percent contraction, $g(x,t)$ is a function between 0 and 1 that either contracts or expands a section of tube depending upon the position and time in the simulation. $\tilde{g}(t)$

is a function which translates the peristaltic wave down the length of the tube at a constant velocity.

Following figure 3.1.1 we are able to describe the movement of one peristaltic wave. At the beginning of the simulation the tube is at rest. As time increases, $g(x, t)$ increases to 1 and contracts the boundary at the left end of the bottom straight portion of tube. After the prescribed percent occlusion is achieved, the contraction site is translated via $\tilde{g}(t)$ from left to right along the length of the tube. Once translation is complete, $g(x, t)$ decreases to 0 to decompress the contraction site. This completes one pulse period.
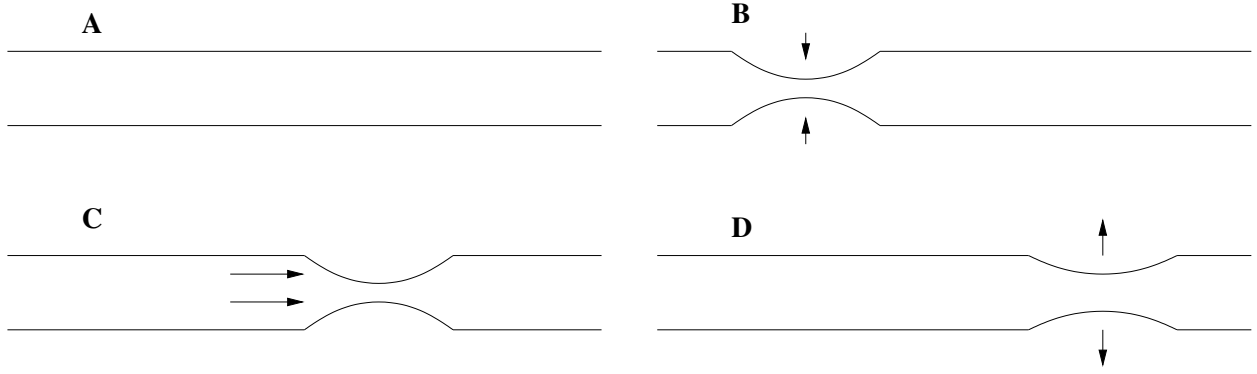


Figure 3.1.1: A) Tube is at rest. B) Contraction starts towards the left end of the flexible straight portion of the tube. This motion is determined by $g(t)$ C) Compressed section travels the length of the flexible tube via the function $\tilde{g}(t)$. D) Decompression is completed by decreasing the function $g(t)$. This ends one pulse cycle.

## 3.2   Dynamic suction pump

The dynamic suction pump includes an isolated region of active contraction which generates passive elastic waves down the flexible portion of the tube, see figure 1.3.1. The region of active contraction is off-center, and its position affects the direction and magnitude of the flow. Once the passive elastic wave encounters the more rigid section of the tube, the wave is reflected and travels in the opposite direction along the flexible boundary.

To implement this pumping mechanism, a section of moving target points are created along the inner and outer tube walls in the region of active contraction. The target points move in a prescribed sinusoidal motion. These target points have an $(x, y)$ position, but only the y-position of the target points will change in time. Denote the inner region of target points as $Y_T^i(x, t)$ and

the outer region as $Y_T^o(x, t)$. The region of points tethered for active contraction is generally much smaller than the overall number of points along the straight portion of the tube. The motion of the target points is then prescribed as

$$Y_T^i(x, t) = r_i + \alpha d2 \sin\left(2\pi t\beta - \pi 2\right), \tag{3.3}$$

$$Y_T^o(x, t) = r_o - \alpha d2 \sin\left(2\pi t\beta - \pi 2\right). \tag{3.4}$$

Here $\alpha$ sets the percent contraction, $d$ is the diameter of the tube, and $\beta$ is dependent upon the desired frequency of contraction. Note that $\alpha$ controls how much of the tube is compressed so that if $\alpha = 1$ the tube would completely contract.

## 3.3   Results

Immersed boundary simulations were run for a large range of Womersley numbers and tube diameter to length ratios for the cases of both peristalsis and dynamic suction pumping. Womersley number is the only dimensionless number computed for these simulations. Womersley, $Wo$, was changed by modifying the dynamic viscosity, $\mu$, for a set tube diameter, frequency of compression is held constant at 2.3hz for all simulations and the density of the fluid, $\rho$, is that of room temperature water. Numerical simulations spanned $Wo$ ranging from 0.1 to 50. This range covers the small scale biological applications, such as the vertebrate embryonic heart, to larger scale biological and engineering applications.

### 3.3.1   Peristaltic Pumping

Peristaltic pumping was simulated for $Wo$ ranging from 0.1 to 50 and with tube diameters ranging from 10 microns to 60 microns (for diameter to length ratios ranging from 0.04 to 0.24). Average instantaneous velocity over a cross section was calculated by taking the mean velocity in the direction parallel to the walls over a line perpendicular to the walls in the rigid section of the racetrack. This metric allows for direct comparisons to values reported by Jung and others [20; 19]. Net flow velocities were calculated by averaging the instantaneous velocities during the fifth to eighth pulse

18

cycles. For the $Wo$ considered, flow rates became periodic after three pulses. Net flow velocities are then reported for each $Wo$ to provide a broader sense of how $Wo$, magnitude of transport, and flow direction are related.

**Vorticity and instantaneous average velocity**  Figure 3.3.1 shows the first period of peristaltic pumping for $Wo = 0.2$. Notice that the fluid is initially at rest, and passive tracers denoted as black markers are positioned in the bottom portion of the tube. The tube compresses in the second frame and begins to translate in the third frame. In the fourth frame, the tube begins to decompress. Instantaneous vorticity is denoted in each color plot, with lighter colors corresponding to regions of positive vorticity and darker colors corresponding to regions of negative vorticity. Even at this small $Wo$, peristaltic transport produces positive net fluid flow. The passive fluid tracers are transported at about the speed of the peristaltic wave front.

Figure 3.3.2 shows the first period of peristaltic pumping for $Wo = 10$ where inertial effects are significant. The fluid is initially at rest in the first frame, the tube contracts in the second frame, the region of contraction begins to translate in the third frame, and the tube decompresses in the fourth frame. The vorticity plots show regions of significant mixing in the region behind the traveling wave of contraction. Both the continual movement of the passive fluid tracers and the average velocity vs. time plot, figure 3.3.3, indicate that the fluid continues to move even after the translation portion of the pumping period has finished.

Figure 3.3.3 provides a comparison of the instantaneous average velocity vs. time generated by peristaltic pumping at both high and low $Wo$. Here the average velocity is computed along a vertical cross section along the diameter of the tube for each time step. These results show that it is an effective mechanism of driving fluid across many scales. Recall that for $Wo = 0.1$, unsteady effects are negligible, and this scale is within the range of the vertebrate embryonic heart tube. For $Wo = 10$, unsteady effects are significant. The differences between small and large scale peristaltic transport are due to inertial effects, and oscillations in the average flow rate can be seen for $Wo = 10$. The initial acceleration from rest of the wave front imparts energy to the fluid resulting in spikes at the beginning of each period. For $Wo = 10$, the fluid continues to move after the translation of the compress regions ends. For $Wo = 0.1$, the flow briefly moves in the opposite direction as the contraction region decompresses and goes to zero before the beginning of the subsequent contraction.

19
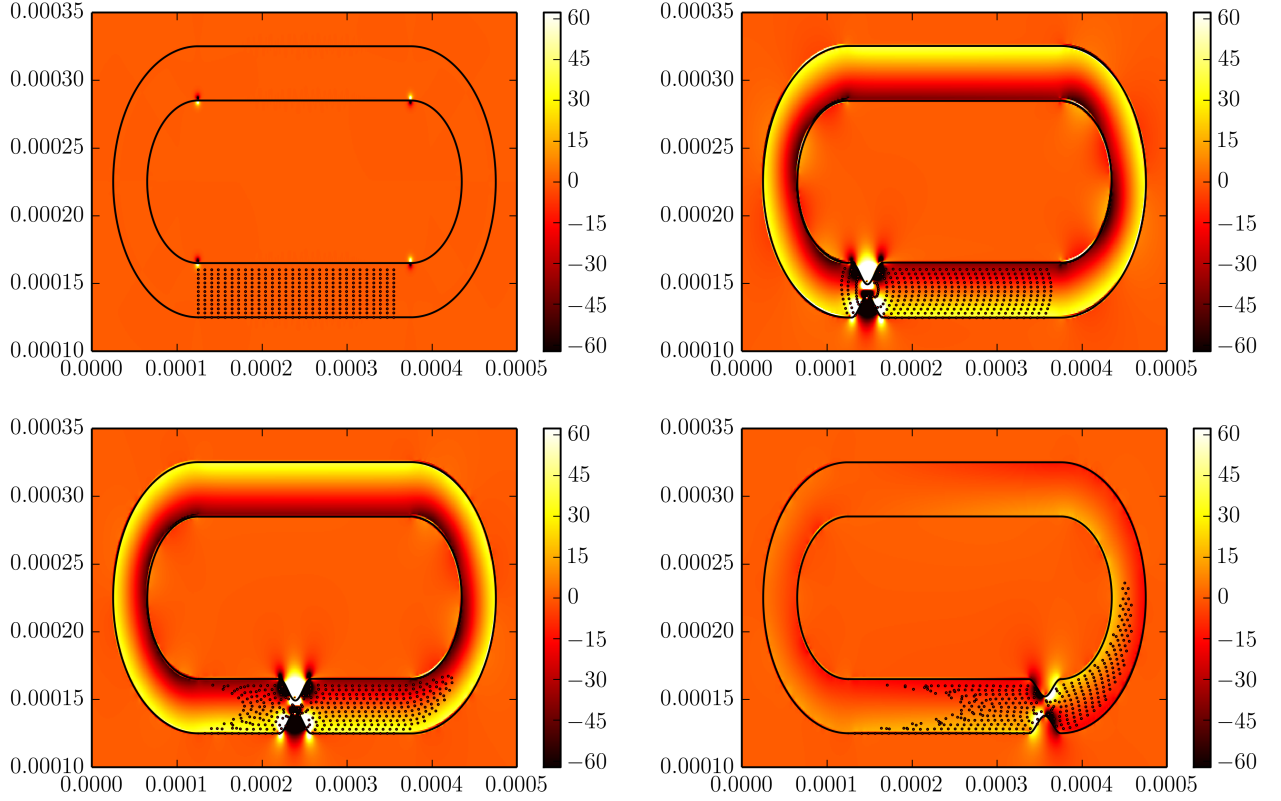
Figure 3.3.1: All images were taken from a peristalsis simulation with $Wo = 0.2$. The colorplot shows the magnitude of vorticity and $x$ and $y$ give the distance in meters. The top left frame shows the tube at rest with passive fluid tracers placed in the bottom section of the tube. The top right frame shows the vorticity and position of fluid tracers $0.05s$ into the simulation as the tube begins to compress. The bottom left frame is $0.2s$ into the simulation and shows the traveling contraction wave. Finally, the bottom right image was taken $0.4s$ into the simulation.

**Average velocity vs. Womersley number**   Figure 3.3.4 shows the average velocity for peristalsis with $Wo$ ranging from 0.1 to 50. Each data point is the velocity averaged over fifth to eigth pulse cycles (or the last $2s$). In addition to changes in $Wo$, the tube diameters were varied from 20 to 60 microns for tube diameter to length ratios ranging from 0.08 to 0.24. Peristalsis is shown to be effective at many different scales and across a range of tube diameter to length ratios. Recall that the $Wo$ is changed by altering the viscosity only, and the average velocities are relatively constant for $Wo < 1$. For $Wo > 1$, the average velocity increases linearly, presumably due to inertial effects and lowered resistance to flow.
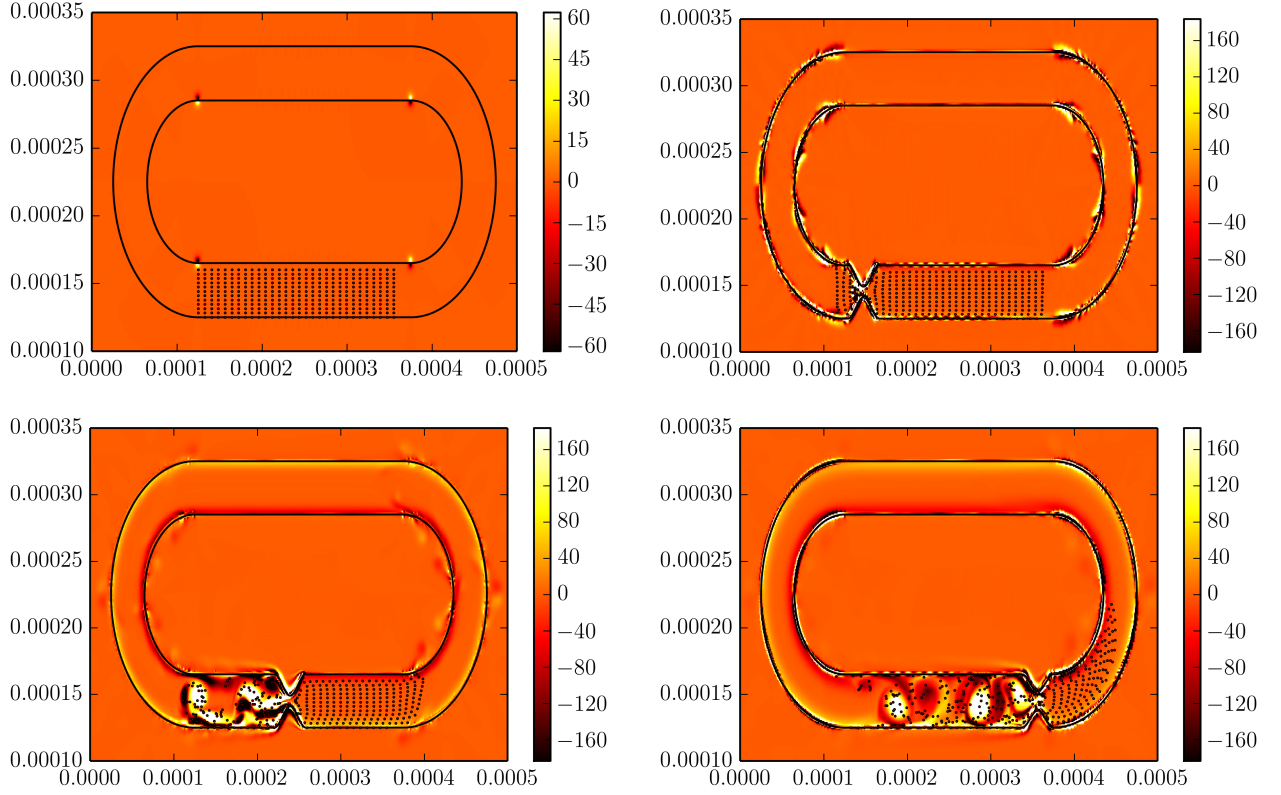
Figure 3.3.2: All images were taken from a peristalsis simulation with $Wo = 10$. The colorplot shows the magnitude of vorticity and $x$ and $y$ give the distance in meters. The top left frame shows the tube at rest. The top right frame shows $0.05s$ into the simulation as the tube begins to compress. The bottom left frame is $0.2s$ into the simulation and shows the traveling contraction wave. The bottom right image was taken $0.4s$ into the simulation and shows the decompression of the tube. Particles shown are passive fluid tracers that move with the fluid.

### 3.3.2 Dynamic suction pumping

Dynamic suction pumping was also simulated for $Wo$ ranging from 0.1 to 50 and for tube diameters ranging from 10 to 60 microns (for diameter to length ratios of 0.04 to 0.24). Average instantaneous velocities were again calculated by taking the mean flow velocity along a cross section of the rigid portion of the tube at each time step. Temporally averaged velocities were calculated over the fifth to eighth pulse cycles.

21
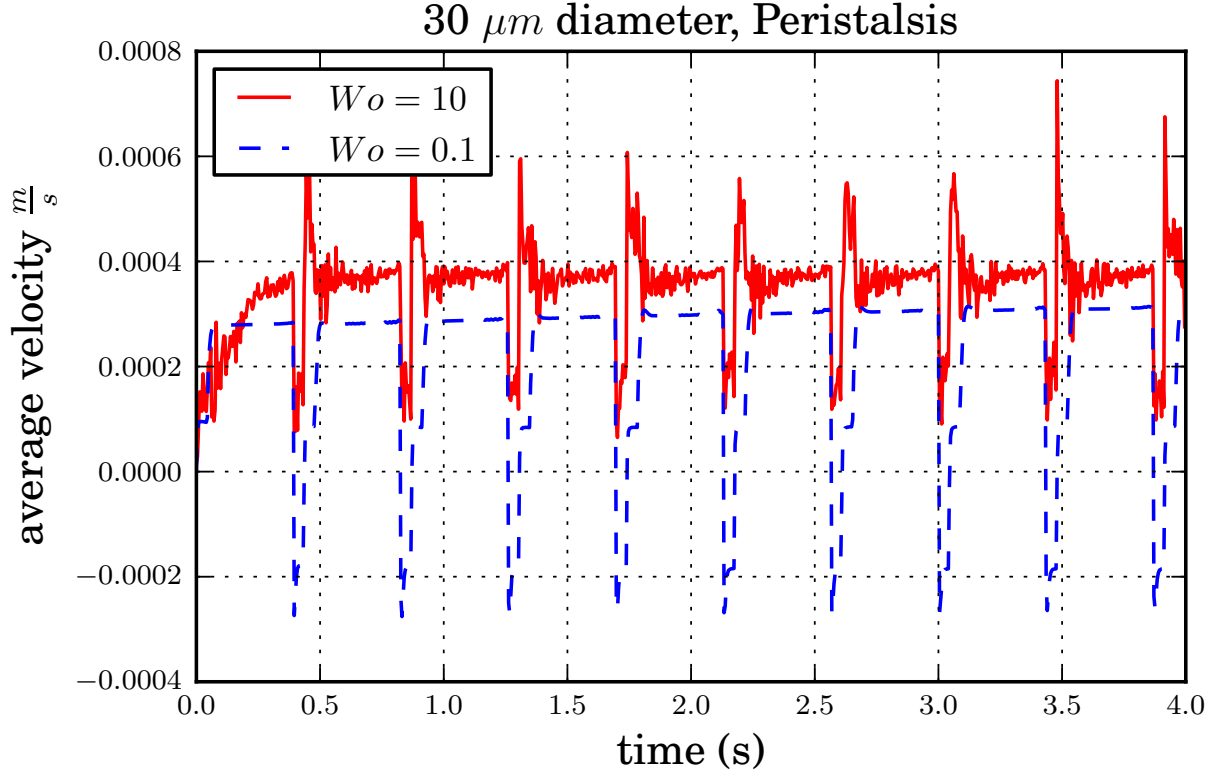
Figure 3.3.3: Instantaneous average velocity vs. time for peristaltic pumping for $Wo = 0.1, 10$. At both scales fluid is effectively transported. More inertial effects can be seen in the oscillations present at $Wo = 10$.

**Vorticity and instantaneous average velocity**   Figure 3.3.5 shows the first period of dynamic suction pumping for $Wo = 0.2$. Notice that the fluid is initially at rest, and passive tracers denoted as black markers are positioned in the bottom portion of the tube. Little net fluid flow is generated for $Wo = 0.2$ where inertial effects are negligible. Passive fluid tracers are displaced in both directions during the contraction and are pulled back close to their original positions during the expansion. It is clear that, although some motion is present for this frequency, significant positive transport of fluid is not present. Instantaneous vorticity is denoted in each color plot, with lighter colors corresponding to regions of positive vorticity and darker colors corresponding to regions of negative vorticity. Passive elastic traveling waves are not created due to the high viscosity of the fluid in which the tube is immersed.

Figure 3.3.6 shows the first period of dynamic suction pumping for $Wo = 10$. Although not much net flow is generated during this initial pulse cycle, there is positive net flow after a few pulses
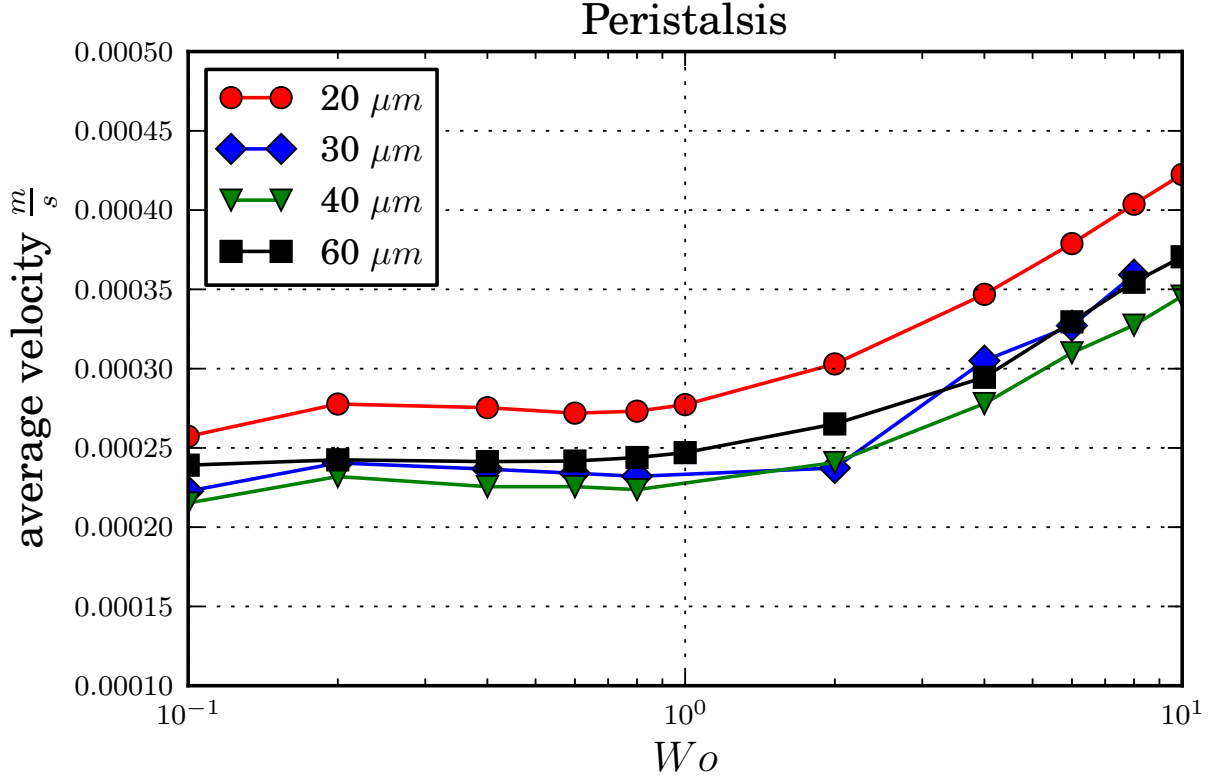
Figure 3.3.4: Average velocity vs. $Wo$ for peristaltic pumping for tube diameters of 20, 30, 40 and 60 microns. Significant average velocities are achieved for a variety of scales. For $Wo > 1$, average flow velocities increase steadily due to the inertial effects of the fluid at these larger scales.

for higher $Wo$. In addition, vortices are generated near the region of contraction that result in more mixing of the fluid, as seen from the positions of the passive fluid tracers. The presence of passive elastic waves emanating from the active contraction site may also be observed.

Instantaneous average velocities vs. time computed along a cross section of tube are shown in figure 3.3.7 for $Wo = 0.1$ and 10. Recall that the $Wo$ was changed only by altering the viscosity, and this difference in the magnitude of $Wo$ shows the dramatic difference in effectiveness of this pumping mechanism in the inertial and viscous regimes. Large peak flows are observed for $Wo = 10$. Even though flow rates do become negative at the end of the cycle, the net flow over the entire period is positive. In contrast, the magnitude of the flow velocity for $Wo = 0.1$ is significantly smaller, and the net flow over the entire pulse cycle is close to zero. One key feature of dynamic suction pumping is that inertial effects drive the generation of passive elastic waves which enhance transport. For $Wo = 10$, the maximum fluid velocity increases with each pumping period, but
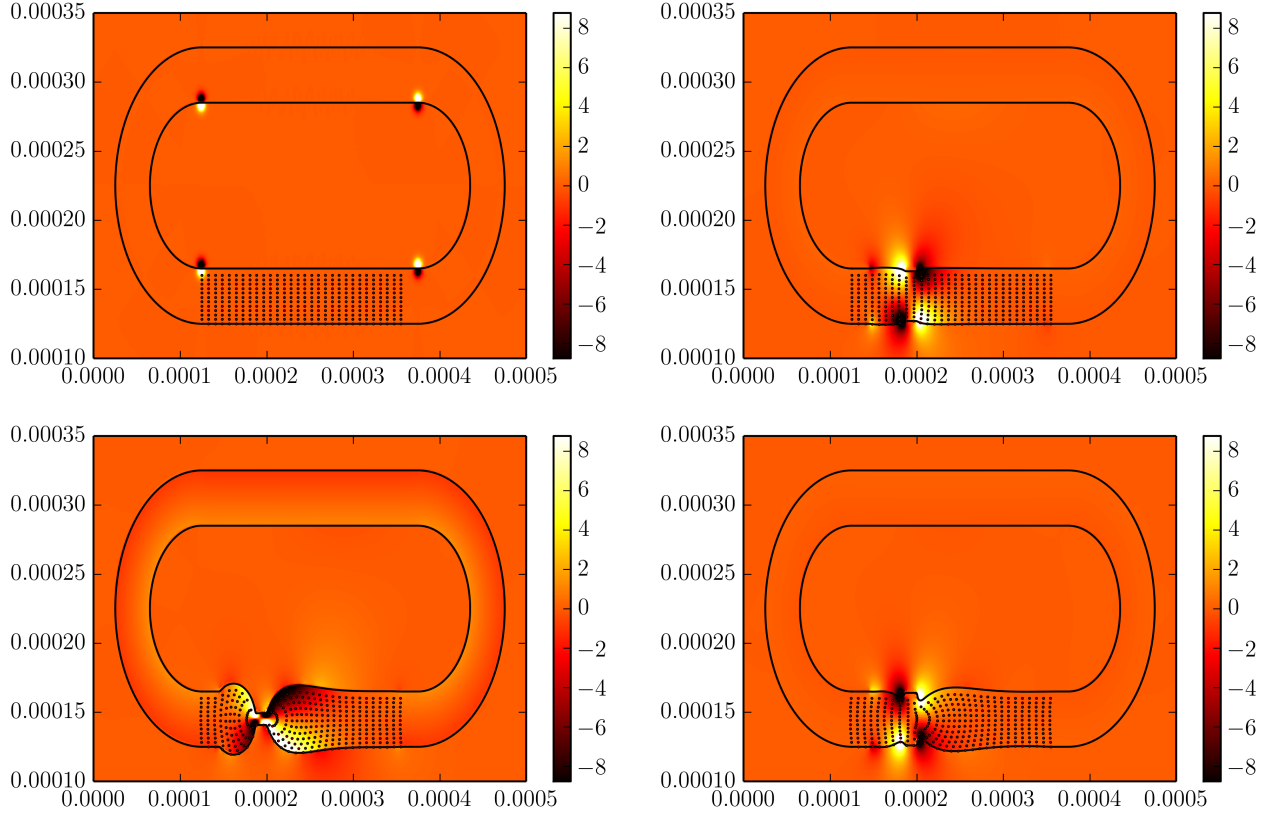
Figure 3.3.5: All images were taken from a dynamic suction pumping simulation with $Wo = 0.2$. The colorplot is based upon magnitude of vorticity, and the $(x, y)$ axis shows distance in meters. The top left frame shows the tube at rest at $t = 0$. The top right frame is $0.05s$ into the simulation and shows the beginning of tube compression. The bottom left frame is $0.2s$ into the simulation, and the bottom right image is taken $0.4s$ into the simulation. The black dots are passive fluid tracers that move with the fluid.

becomes periodic after about 10 cycles.

**Average velocity vs. Womersley number**  Figure 3.3.8 shows the velocity averaged over the fifth to eighth pulse cycles as a function of $Wo$ for dynamic suction pumping. The diameter of the tube is varied from 20 microns to 60 microns (tube diameter to length ratios of 0.08 to 0.24). In general, nearly zero net flow is generated for $Wo < 1$ for all cases studied here. Another interesting feature is the appearance of flow reversals for intermediate $Wo$ in the range of about $10^0$ to $10^1$.

24
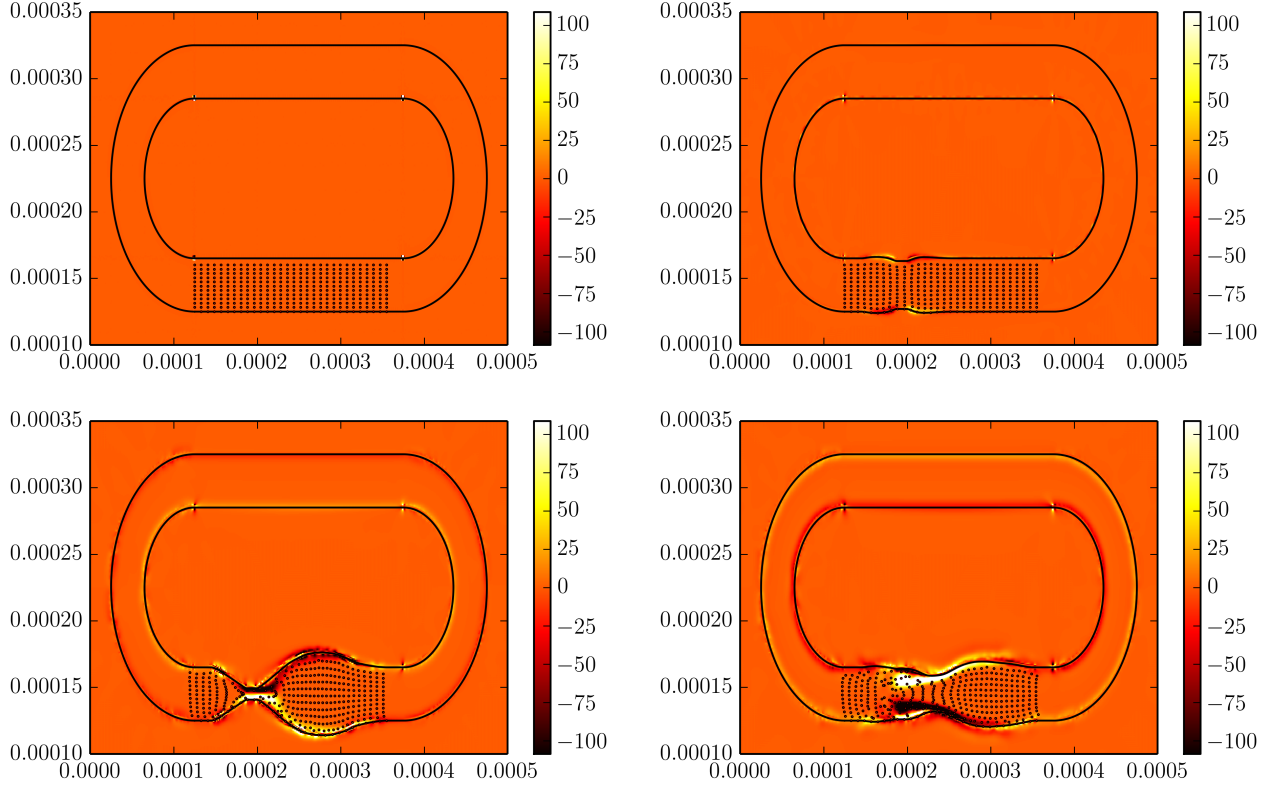
Figure 3.3.6: All images were taken from a dynamic suction pumping simulation with $Wo = 10$. The colormap is based upon magnitude of vorticity, and the $(x, y)$ shows distance in meters. Top left picture is $0.0s$ into the simulation. The top right frame is $0.05s$ into the simulation and shows the initial compression of the tube. The bottom left frame is $0.2s$ into the simulation, and the bottom right image was taken for simulation time equal to $0.4s$ and shows the decompression of the tube. The black dots are passive fluid tracers that move with the fluid.

Such flow reversals have been observed in numerical simulations and physical models [20]. The sharp transitions in directions for intermediate $Wo$ could have significant implications for biological systems.

Another notable and interesting feature involving this pumping mechanism is its sensitivity to the ratio of tube diameter to length. This ratio clearly affects both the magnitude of the flow as well as its direction. The sensitivity to this parameter could have a very significant effect in regards to biological applications which span a very diverse range of tube geometries. There have been many studies examining dynamic suction pumpings' effectiveness in regards to pumping frequency, location of pumping, and amplitude of contraction[20]. The results indicate that the effect of the diameter to length ratio should be investigated further.

25
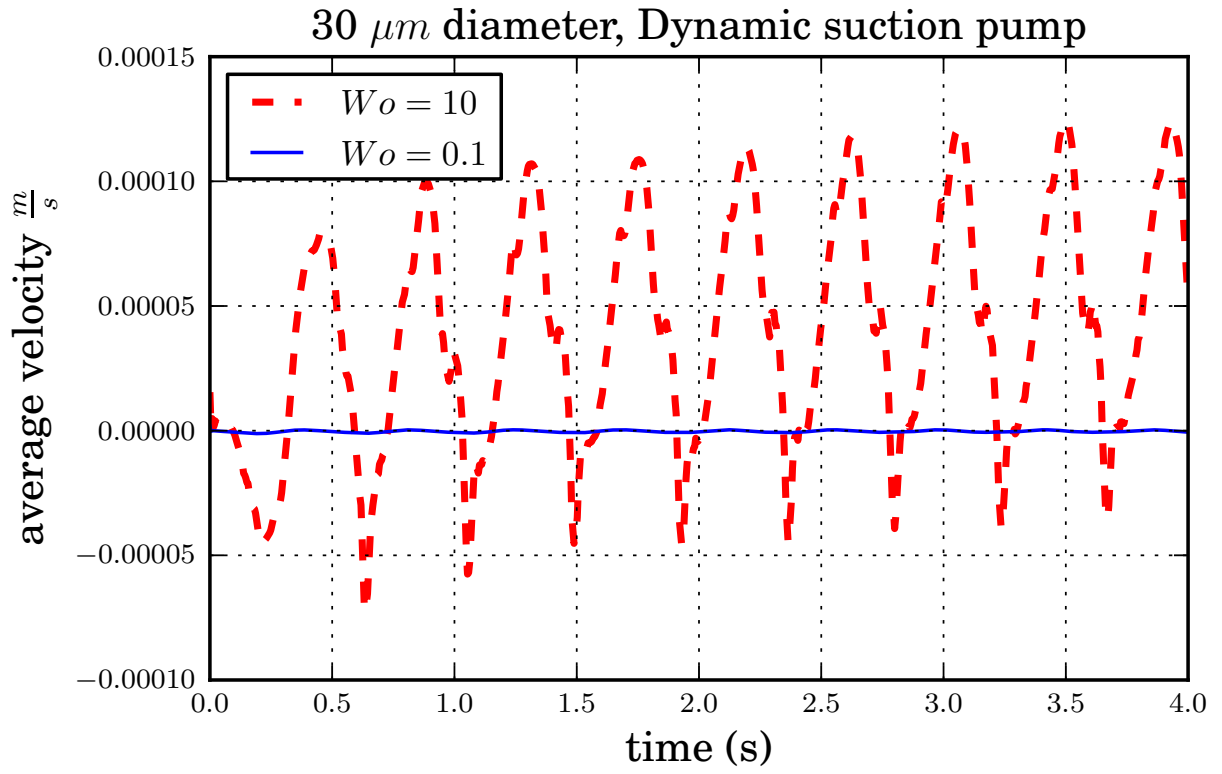
Figure 3.3.7: Instantaneous average velocity vs. time for dynamic suction pumping for $Wo = 0.1, 10$. Note that the $Wo$ was varied only by changing the fluid viscosity and that the flow is significant stronger for the $Wo$ case when inertial effects are significant.
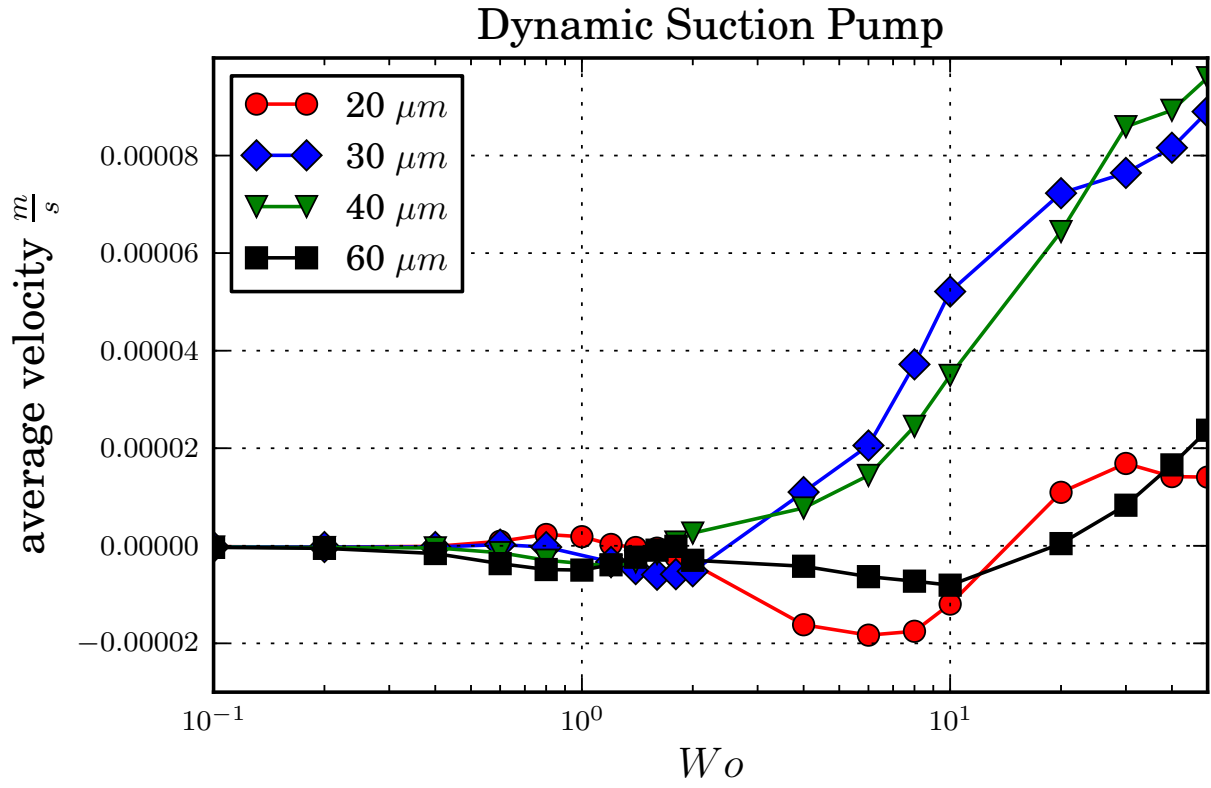
Figure 3.3.8: Average velocity vs. $Wo$ for dynamic suction pumping for tube diameters of 20, 30 , 40 and 60 microns. Each diameter has near zero flow for $Wo \leq 1$. Significant net flow is generated for $Wo > 1$. As tube diameter increases, average velocity increases.

**CHAPTER 4: IMPEDANCE PUMPING AND FLOW DIRECTION**

Dynamic suction pumping, or impedance pumping, is a mechanism which has been speculated to be the driving force behind the uni-directional flow present in valveless tubular hearts. Impedance pumping has been shown to be an effective valveless pumping mechanism over a range of scales and studies have shown that flow magnitude and direction are coupled to the pumping position and frequency of contraction. Although the bi-directional nature of the mechanism is something which has been observed both numerically and physically, no well established explanation has been offered. Understanding the bi-directional nature of this pumping mechanism is important in the design and use of valveless tubular pumps and also has implications for the biological function of valveless hearts. In this thesis we will address the bi-directional nature of impedance pumping by investigating flow direction as a function of tube diameter and the elastic properties which govern the resonant frequency of the system. Direct numerical simulations of the fully-coupled fluid-structure interaction problem will be used to determine the magnitude and direction of fluid flow as a function of the non-dimensional ratio of elastic tube length to tube diameter. It can be seen that this ratio can directly determine both the magnitude and direction of fluid flow. The resonant frequency of the tube, based upon the elastic properties of the model and the added mass of the fluid is also investigated. Resonance of two separate sections of the tube divided by the compression region are shown to govern the resulting direction of flow.

## 4.1 Impedance pumping

To numerically simulate impedance pumping a region of target points was connected to a portion of flexible tubing which began a distance $\alpha_2$ from the left most rigid boundary of the bottom straight portion of the flexible tube, figure **??**. These target points oscillate in a prescribed motion, creating a force on the boundary that causes movement. The collection of target points along the inner wall

Table 4.1: Non-dimensional spatial dimensions and numerical parameters for the impedance pumping simulations. All spatial parameters were non-dimensionalized using the characteristic length scale: $\mathcal{L} = 0.00025$, the length of the bottom pumping region, see figure 4.1.1. The time parameters $\hat{dt}$ and $\hat{t}$ were non-dimensionalized using the characteristic time scale: $t_{final} = 4.0s$.

| Parameter | Value |
|---|---|
| Length of domain | 2.0 |
| Width of domain | 2.0 |
| Tube length scale $[\frac{\mathcal{L}}{d}]$ | 4.0-8.0 |
| Outer radius $[\hat{R}_1]$ | 0.4 |
| Inner radius $[\hat{R}_2]$ | R1 - diameter |
| Length of straight tube $[\mathcal{L}]$ | 1.0 |
| Frequency of pumping $[\omega]$ | 1.5-12.0 hz |
| Percent of contraction | 0.8 |
| Pulse Period | $1f$ |
| Final simulation time $[\hat{t}]$ | 1.0 |
| Time step $[\hat{dt}]$ | 7.62e-6 |
| Spatial step $[\hat{dx}]$ | 3.33e-3 |
| Boundary step $[\hat{ds}]$ | 1.67e-3 |

Table 4.2: Non-dimensional mechanical variables for impedance pumping simulations. The characteristic length scale is defined to be the length of the straight pumping region $\mathcal{L}$ and the characteristic velocity is defined to be: $\mathcal{U} = \frac{\mathcal{L}}{T}$, where $T$ is the pumping period.

| Parameter | Value |
|---|---|
| Bending coefficient of the boundary $[\hat{\kappa}_{beam} = \kappa_{beam}\rho_0\mathcal{U}^2\mathcal{L}^3]$ | 5.31e25 |
| Stretching stiffness of the boundary $[\hat{\kappa}_{spring} = \kappa_{spring}\mathcal{U}^2\rho_0\mathcal{L}]$ | 3.24e15 |
| Stretching stiffness of target points $[\hat{\kappa}_{target} = \kappa_{target}\mathcal{U}^2\rho_0\mathcal{L}]$ | 3.24e15 |
| Womersley Number $[Wo = r\sqrt{\omega\nu}]$ | 5-10 |

of the tube is given by: $Y_T^i(x,t)$ and the collection of target points along the outer tube is given by: $Y_T^o(x,t)$. We can then define the motion of the pumping mechanism as:

$$Y_T^i(x,t) = \gamma + |\alpha d2\sin(2\pi t\beta - \pi 2)|, \tag{4.1}$$

$$Y_T^o(x,t) = (\gamma + d) - |\alpha d2\sin(2\pi t\beta - \pi 2)|. \tag{4.2}$$

The absolute value allows the mechanism to only pump into center axis of the tube. $\gamma$ shifts the pumping location to the straight boundary, $\beta$ controls the frequency of the pumping mechanism and $\alpha$ controls the amplitude of compression. For the numerical experiments described here, $\alpha$ was always set to $0.4d$, which provides an 80% contraction.
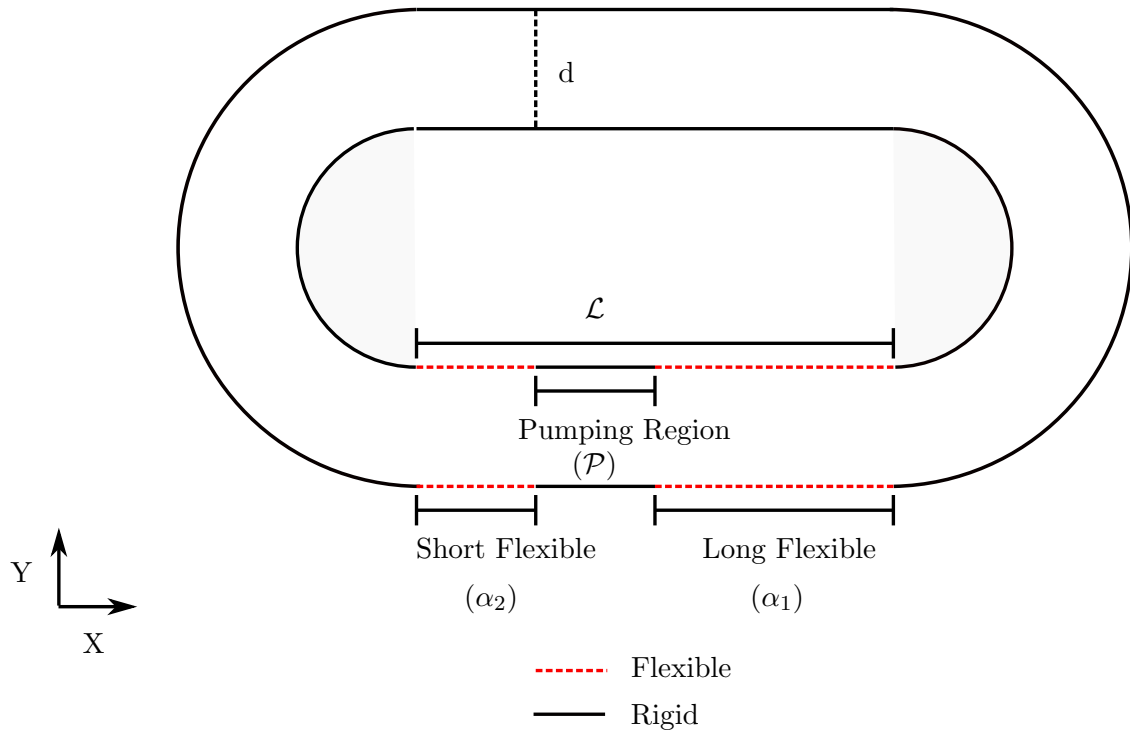
Figure 4.1.1: A digram of the computation model is shown here. The tube is a connected racetrack with diameter $d$, and total pumping region length $\mathcal{L}$. The lengths of the long and short sections of the elastic tube are denoted as $\alpha_1$ and $\alpha_2$, respectively. These two lengths change depending on the pumping location, and the total length of this region is denoted as $\mathcal{P}$.
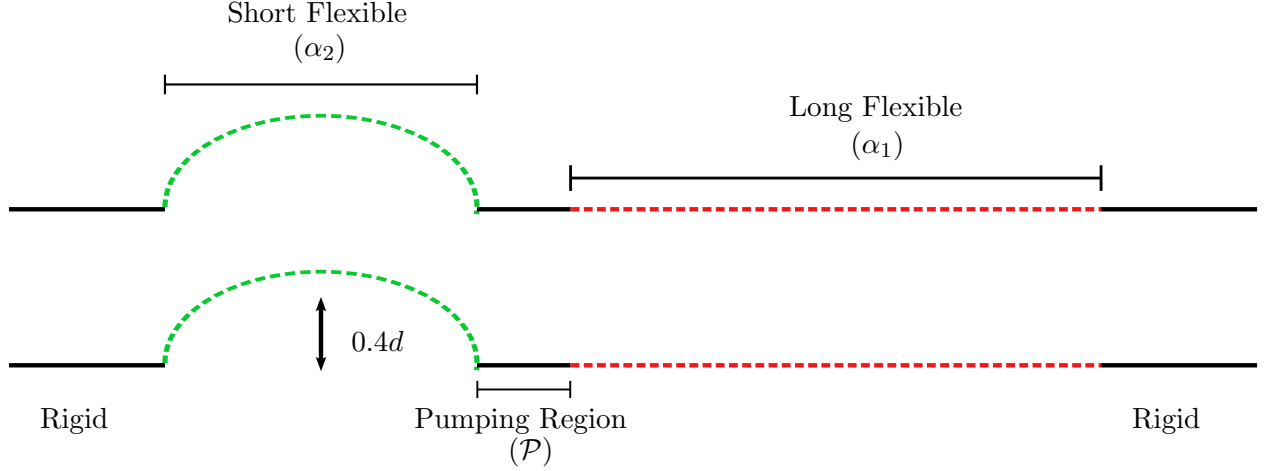
Figure 4.2.1: A model diagram detailing the resonance experiments performed. The flexible tube of the short and long sections were displaced using a sine function with amplitude $0.4d$. The elastic walls of the tube were then allowed to oscillate in free vibration. This numerical experiment was done for four separate pumping locations.

## 4.2    Resonance experiments

The flexible portion of the tube at the bottom of the racetrack can be divided into two smaller sections to the left and the right of the contraction region. Each of these sections will have different resonant frequencies. Impedance pumping relies upon elastic properties of the tube to translate the waves generated from the pumping site down its length. Travel times and amount of fluid being displaced by the boundary are different for each section due to the length. To quantify this effect, the resonant frequency of each section was calculated separately. Resonant behavior has been investigated numerically in 2008 by Gharib et al. and it was shown that the resonant frequency of the tube corresponded to the maximum flow rate computed for that experiment[22]. Results from other experimental, analytical and numerical papers suggest that frequency is one determining factor in flow direction and that the resonant frequency computed from the elastic properties of the tube corresponds to the maximum bulk flow rate. In this thesis we do not compute the resonant frequency from the material properties of the entire tube but instead calculate the frequency of free vibration of the long and short sections independently. This approach takes into account the nonlinear effect of the entrained fluid.

From figure 4.2.1 we displace the short and long sections of the boundary by:

$$X_{short}(s,t) = (0.4d)\sin\left(\pi\beta_1(s)\right) \tag{4.3}$$

$$X_{long}(s,t) = (0.4d)\sin\left(\pi\beta_2(s)\right). \tag{4.4}$$

Here $\beta_1(s)$ and $\beta_2(s)$ are both functions of the the Lagrangian boundary position $s$. For these experiments the pumping location is moved to the five different pumping positions considered in this thesis. We define these positions by the non-dimensional length of the short flexible section bordering the pumping region ($\alpha_2 = \{0.25, 0.29, 0.33, 0.39, 0.43\}$). We can then calculate the movement of the boundary using the immersed boundary. The peak displacement of each section is tracked in time. The dominant frequency of free vibration is computed via a discrete Fourier transform.

## 4.3 Results

There were three variables tested in this study to investigate flow direction in impedance pumping: diameter to length ratio of the model racetrack, pumping location, and frequency of contractions. We began from the results in Baird et al. [1] where flow direction was seen to change for Womersley numbers in the range of $1 \leq Wo \leq 10$. Expanding these results we first investigated the non-dimensional length ratio defined to be $\hat{\mathcal{L}} = \frac{\mathcal{L}}{d}$ by altering the diameter of the tube. These simulations have a fixed frequency of pumping ($f = 2.5hz$), pumping location $\mathcal{P}$, viscosity $\mu$ and non-dimensional spring and bending stiffness ($\kappa_{beam}$, $\kappa_{spring}$), see table 2.The effects of pumping frequency on flow direction were quantified by performing simulations for a fixed non-dimensional length scale $\hat{\mathcal{L}}$ while varying the frequency of pumping $1 \leq f(hz) \leq 11$. This range of pumping frequencies was applied to the tube using four different pumping locations. The pumping location had the effect of changing the non-dimensional lengths of the two different pumping regions. The lengths of these regions are given as: $\alpha_1$ and $\alpha_2$ for the long and short sections of the flexible tube respectively. All numerical experiments were performed for constant non-dimensional stretching and bending stiffness.

### 4.3.1 Non-dimensional Length Scale

We begin by looking at the flow direction as a function of the non-dimensional length scale parameter, $\hat{\mathcal{L}} = \frac{\mathcal{L}}{d}$. Here $\mathcal{L}$ is the length of the elastic region and $d$ is the tube diameter. The diameter $d$ was

varied to quantify how $\hat{\mathcal{L}}$ affects on flow direction in impedance pumping. Each data point was obtained by applying a fixed pumping frequency of 2.5 Hz and calculating the average instantaneous flow velocity along a cross section in the upper straight tube region. These velocities were then averaged over the second half of the simulation time to get a steady state average velocity.
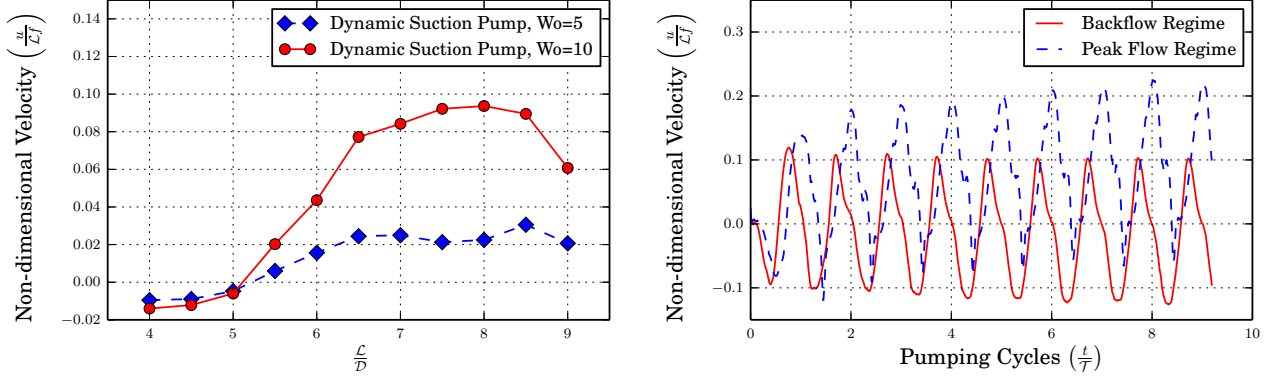


Figure 4.3.1: Average dimensionless velocity as a function of the diameter to length ration, $\hat{\mathcal{L}}$, (left) and dimensionless velocity vs. time for the peak flow cases (right). The averaged velocity shows the same trend for $Wo = 5$ and $Wo = 10$, where $Wo$ was changed by altering the viscosity and holding all other parameters fixed. The magnitude of the average velocity is diminished in the lower $Wo$ case. On the right is the average velocity as a function of $\hat{t}$ for $Wo = 10$. Here the characteristic time is $\mathcal{T} = \frac{1}{f}$, where $f = 2.5 hz$.

The results from figure 4.3.1 show that the flow direction of impedance pumping is a function of the parameter $\hat{\mathcal{L}}$. As this parameter is increased, the diameter of the tube $d$ is decreased since the length $\mathcal{L}$ remains fixed, and the flow direction changes from clockwise to counter clockwise. Also of note is the fact that the magnitude of the velocity is maximized for $7.0 \leq \hat{\mathcal{L}} \leq 8.5$. The simulations are also run for a lower $Wo$ and similar dynamics are seen, figure 4.3.1. The magnitude is reduced due to the increase in the resistance to shear due to increasing the viscosity $\mu$. The reduction in the magnitude of flow due to lowered $Wo$ is consistent with results seen in other studies[1]. For the remainder of the results the geometry of the tube will be set to $\hat{\mathcal{L}} = 8.0$, which produced maximum flow. In the next section, the effects of the wave forms generated from the pumping region on the direction of bulk flow will be considered.

### 4.3.2 Resonance of the Boundary

To begin the study of how the resonant frequency of the short and long sections of tubing ($\alpha_2$ and $\alpha_1$) affect the flow direction of impedance pumping, $\hat{\mathcal{L}}$ is set to 8.0 and the resonant frequency of the first mode of the short section (defined by the non-dimensional parameter $\alpha_2$) is estimated by creating an open tube immersed in fluid with all the boundary points fixed except for the short section of tube. This section of tube was then initially displaced in the form for a section of a sine function and allowed to oscillate in free vibration until it came to rest. The $(x, y)$ positions of the tube walls were recorded and the maximum displacement along the short flexible section was analyzed using an FFT. Due to the nonlinear properties of the wall under large deformations the frequency spectrum was large. The local maximum were computed from the FFT data and are shown in the figures 4.3.3,4.3.2,4.3.5.

We did completed free vibration experiments for the first mode of the long flexible tube section. We determined that more the dynamics may be encapsulated in analysis of the second mode of the long tubing since observations showed that only half of the long flexible tubing had a large enough compression amplitude for significant fluid transport. These experiments were carried out in the same manner as the short section's first mode but with the necessary changes to the prescribed displacement of tube, see figure 4.3.2. Note that the second mode structure of the boundary can also be seen in the pumping simulations which generated maximal flow in the counter clockwise direction, figure4.3.7.

We now plot the average bulk flow for each pumping frequency to create a graph of average velocity as a function of pumping frequency. The velocity is non-dimensionalized by dividing by the characteristic velocity, defined to be: $\mathcal{U} = \frac{\mathcal{L}}{\mathcal{T}}$ where $\mathcal{T}$ is period of pumping and $\mathcal{L}$ is the length of the straight pumping region in the computational model, see figure 4.1.1. Note that for each data point $\mathcal{T}$ changes depending on the frequency of compressions. We then compare the average bulk flow to the local maximum frequencies computed through the Fourier analysis of the oscillating boundaries. We then preform this analysis for five different pumping locations, defined by the non-dimensional length of the short flexible tube region bordering the pumping mechanism, $\alpha_2$. It can be seen that, in many of the various pumping locations, the resonance of the short section of tubing corresponds well with the maximum clockwise flow generated, or flow traveling towards this
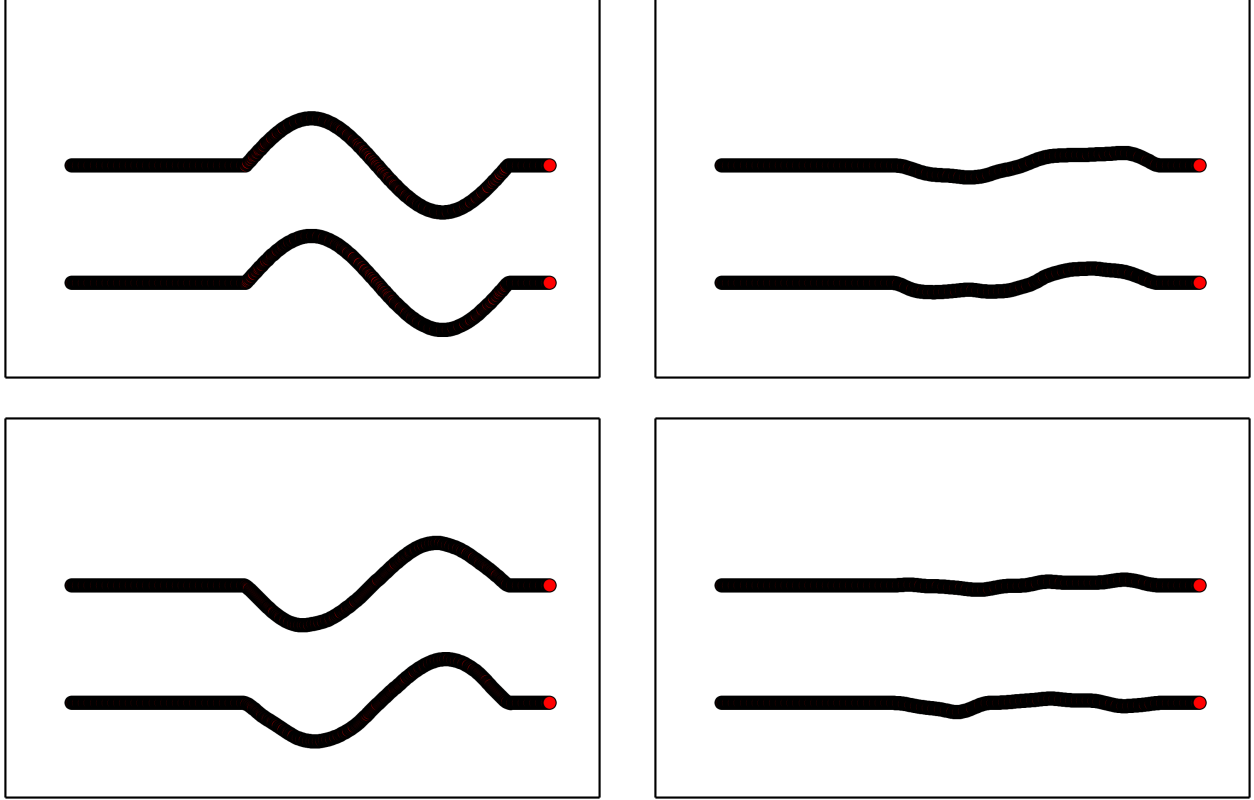
Figure 4.3.2: Resonance experiment for the second mode of the long section of flexible tube are shown here. The top left image shows the tube subjected to the displacement before the simulation begins, and the other frames follow the oscillation of the boundary as it is allowed to freely vibrate. Due to complications in the forces generated from this prescribed displacement, it was necessary to allow the tube to open up into the entire domain rather than connecting it to a racetrack.

section of tube. Similarly the maximum flow generated in the counterclockwise direction seems to be attributed to the resonance of the second mode of the long section for $\alpha_2 = \{0.25, 0.29, 0.33\}$, although some pumping locations don't follow this trend.

The problems seen in some of the results could be attributed to two things: change in the model for resonance analysis and the lengths of the flexible tube regions. The resonant experiments were preformed on an open ended tube not a closed racetrack which was the geometry used to preform the average bulk flow results in the top plot of each of figures 4.3.3, 4.3.2, 4.3.5. This change in geometry was done counteract the forces generated from the displacement of the long section of tubing for the resonant experiments. These forces essentially stuck the tube in place and didn't allow for natural oscillations of the boundary, which are needed to effectively talk about the resonance of
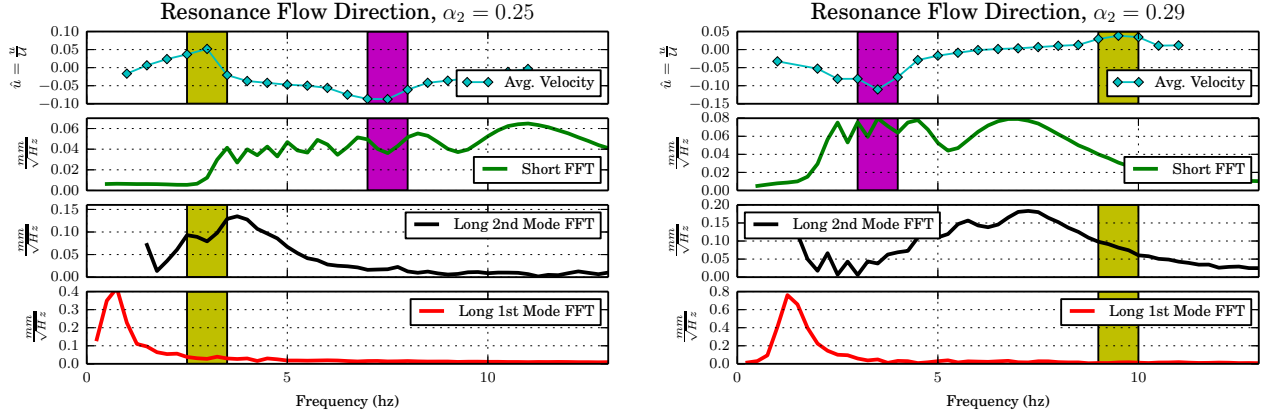
Figure 4.3.3: Each figure is composed of four graphs: average dimensionless velocity over the second half of the simulation, power spectra of the short section excited at its first mode, the power spectra of the long section excited at its second mode and the power spectra of the long section excited at its first mode as functions of the pumping frequency $f(Hz)$. Regions of strong clockwise and counterclockwise flow are highlighted, and local maxima are tagged in the FFT graphs for the free vibration experiments. The left and right graphs correspond to two different pumping regions indicated with the dimensionless length of the short flexible section ($\alpha_2$). Note that $\alpha_2 = 0.25$ indicates the short section is 25% of the bottom straight length of tube.
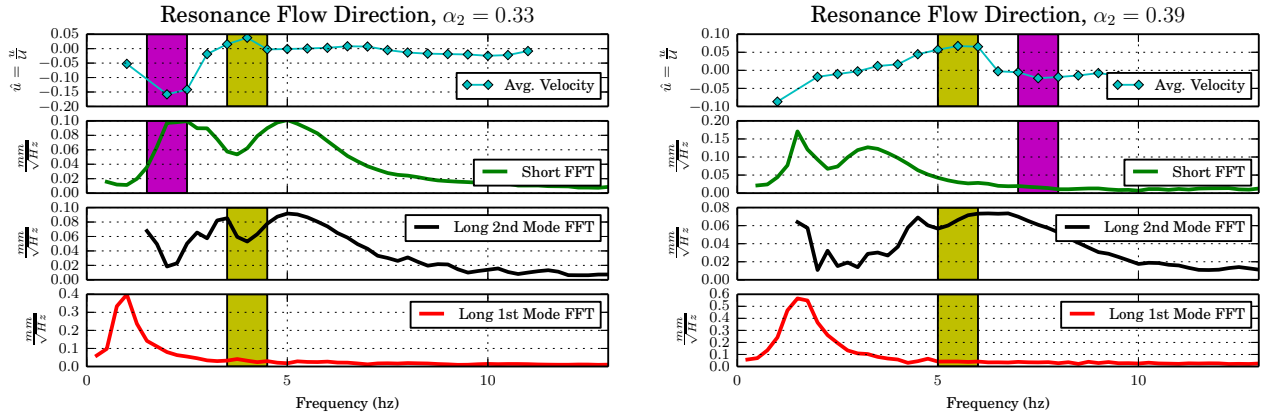


Figure 4.3.4: Each figure is composed of four graphs: average dimensionless velocity over the second half of the simulation, power spectra of the short section excited at its first mode, the power spectra of the long section excited at its second mode and the power spectra of the long section excited at its first mode as functions of the pumping frequency $f(Hz)$. The left figure shows maximum clockwise and counterclockwise flow corresponding to the peaks found during free vibration of each flexible section. The figure on the right follows the previous results for the counterclockwise flow, but the short sections resonant peaks overlap with a no-flow regime.

the immersed boundary. This change could lead to an offset of the peaks computed in the Fourier analysis of the oscillating boundaries and also could be attributed to some of the issues seen in

the results for pumping regions: $\alpha_2 = \{0.39, 0.43\}$. The extremely different results found in figure 4.3.5 is thought to be due to the location of the pumping location. When $\alpha_2 = 0.43$ the pumping location is almost completely centered which causes $\alpha_2 \approx \alpha_1$. Each sections length being near equal doesn't follow our separation of the flexible tubing into two distinct regions: short and long. They are now nearly the same length and, as such, cannot be prescribed the same analysis. It is seen that a completely centered pumping region does not generate any significant flow, but it does seem that slight perturbations to this centered location could generate flow. This type of experimentation could be useful and would likely need a separate approach to the problem.

### 4.3.3 Maximal Flow

An analysis of the mechanical dynamics seen in the pumping experiments which generated maximal flow shows revealing wave dynamics. We show the results for two separate simulations which describe two maxima, one clockwise and one counter clockwise. The maximum clockwise flow is shown for the pumping region $\alpha_2 = 0.29$ with 3.5 hz. pumping frequency. Arrows are show in figure 4.3.6 describing the traveling wave generated from the pumping region. When looking closely at the wave dynamics it becomes clear that for the right pumping frequency the synchronization of the passive elastic traveling wave and the compression of the pumping region allows traveling, near fully occluded, wave form traveling in clockwise direction. These very special wave dynamics are able to achieve some of the highest non-dimensional pumping velocity amongst all the simulations run. This high performance is done with a fairly low pumping frequency, 3.5 hz., compared to the higher frequencies needed to produce similar velocities in the counter clockwise direction. From figure 4.3.3 it can be seen that this pumping frequency corresponds to one of the maximal peaks found in the Fourier analysis of the resonant data for the short flexible tubing.

In the other figure the wave form is slightly more complex due to the longer flexible tubing acting as the wave medium. The non-linear affects of the fluid and the material properties of the boundary more complicated picture. In figure 4.3.7 we try and detail the wave form generated from the pumping region and speculate as to the dynamics which enact maximal flow in the counter clockwise direction. It's can be seen in the first three frames in figure 4.3.7 that there is a traveling wave emitted from the pumping region which almost completely occludes the tube. After the traveling wave propagates a small ways down the long flexible section it interacts with a prior wave which has
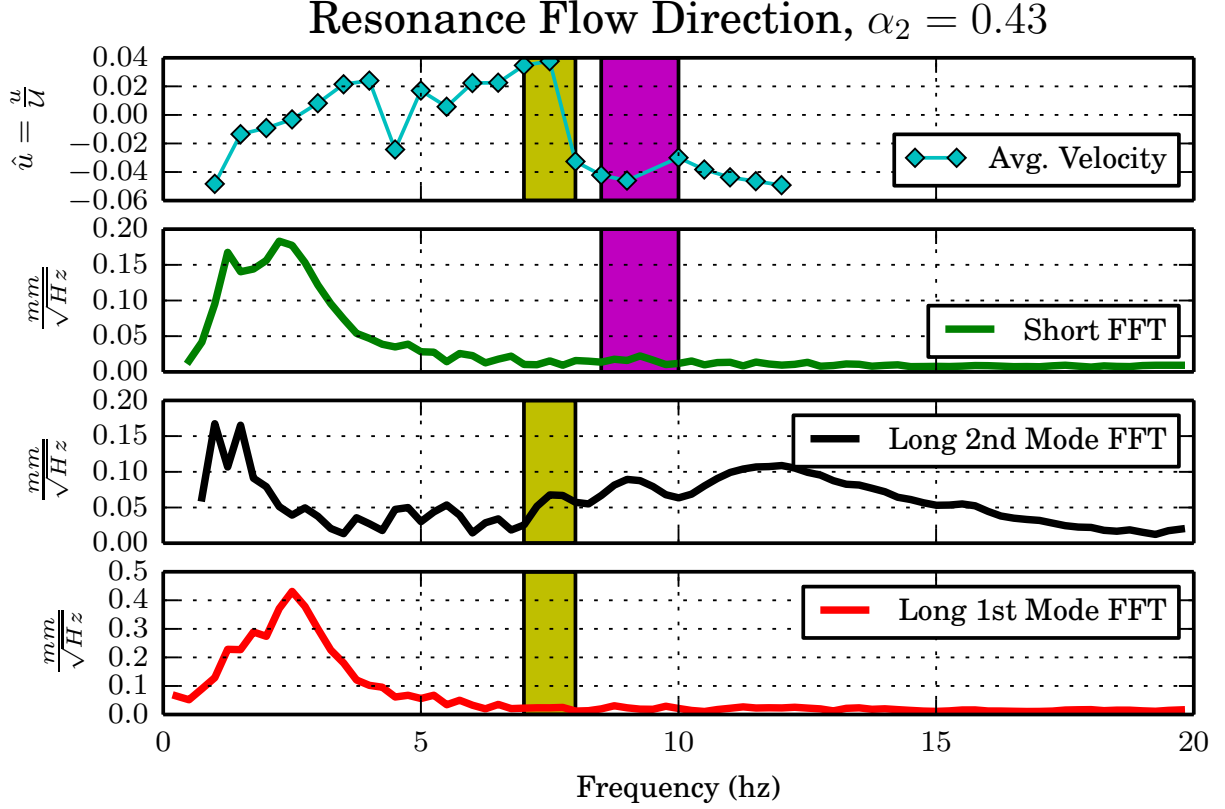
Figure 4.3.5: Each figure is composed of four graphs: average dimensionless velocity over the second half of the simulation, power spectra of the short section excited at its first mode, the power spectra of the long section excited at its second mode and the power spectra of the long section excited at its first mode as functions of the pumping frequency $f(Hz)$. Substantial net flow is not observed for the lower pumping frequencies. This high frequency regime could correspond to the second mode of the short section of flexible tube or possibly the third and fourth modes of the long section. There is some overlap between the resonant peaks of the second mode of the long section and the strong net flow in the clockwise direction, although this result is markedly different from the results seen the previous figures. Extension to higher frequencies and higher modes is needed to get a full understanding of the dynamics when $\alpha_1 \approx \alpha_2$.

been reflected creating a restoring wave form which travels back towards the pumping region briefly.

The wave form of the tube resembles the second mode resonance experiments which leads to the

belief that the second mode of resonance for the long flexible tubing is determining the pumping

frequency in the maximal counter clockwise direction. This can be seen in figure 4.3.2 where the

resonant frequencies from the second mode align with the maximal counter clockwise flow, at 6.0

Hz.
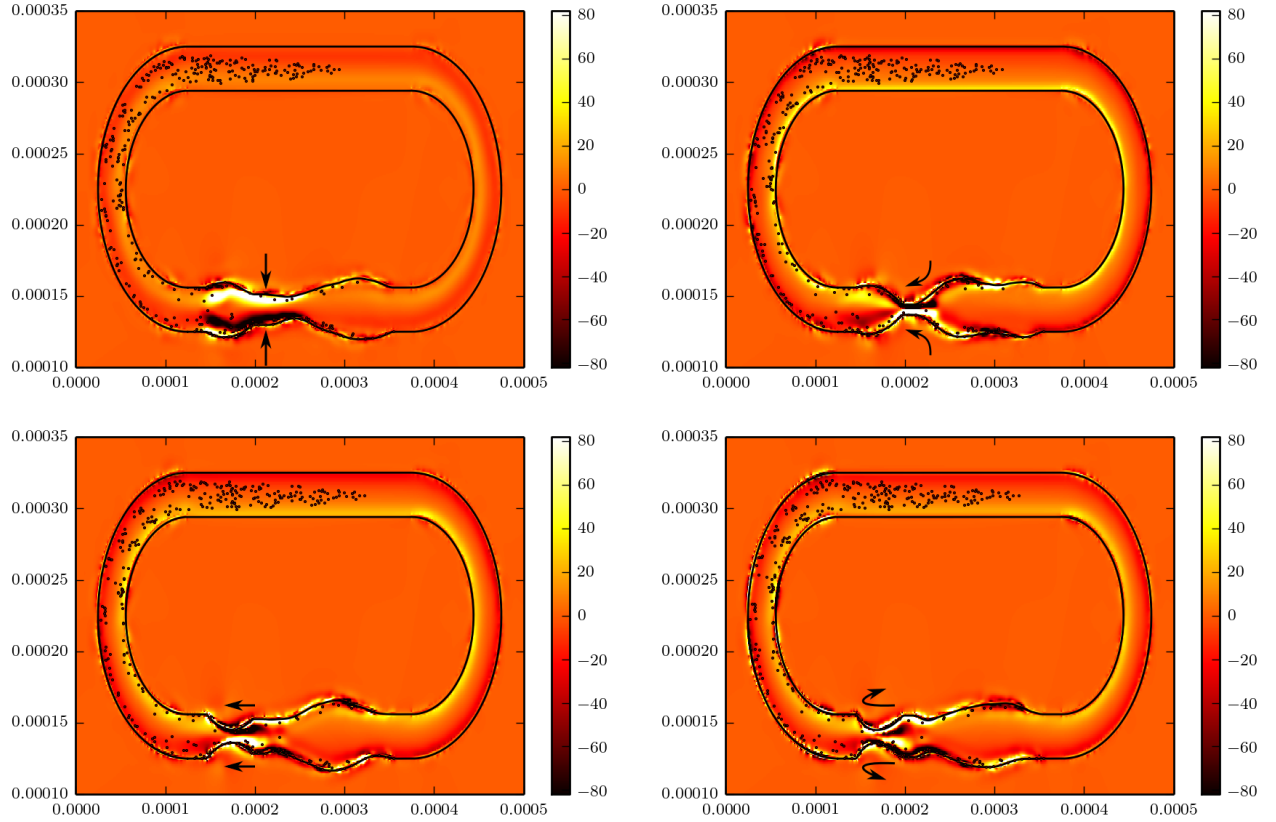
Figure 4.3.6: Vorticity plots showing four snapshots in time over one pumping cycle. The black dots are passive tracers that move with the fluid. These frames display the synchronized traveling wave contraction for the pumping location $\alpha_2 = 0.29$, with a pumping frequency of 3.5 hz. which corresponds to the maximal clockwise flow.
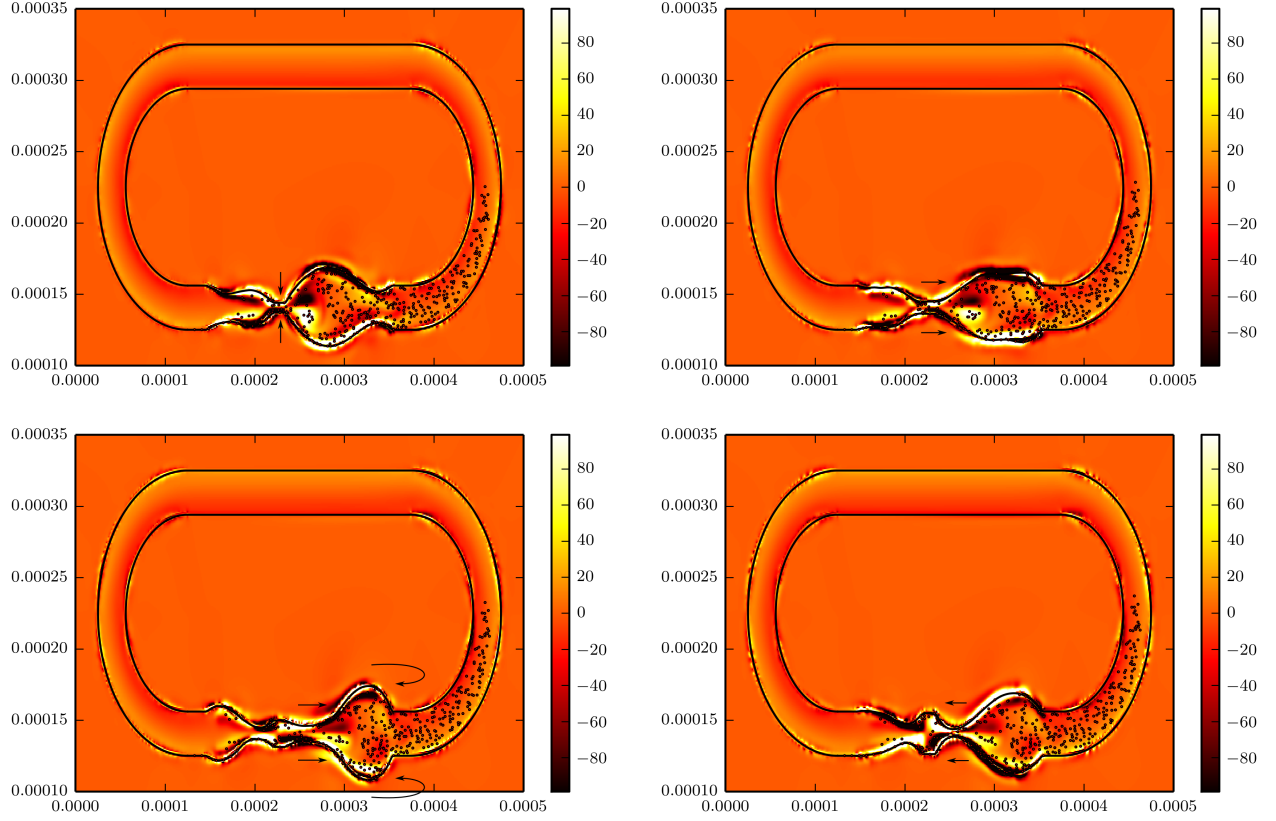
Figure 4.3.7: Vorticity plots showing four snapshots in time over one pumping cycle. The black dots are passive tracers that move with the fluid. The location of the contraction region is set to $\alpha_2 = 0.39$, and the pumping frequency for this simulation is 6.0hz. This parameter choice corresponds to the maximum net flow generated in the counterclockwise direction. The upper right figure shows that the active contraction creates a traveling wave which propagates down the first half of the long flexible section. Upon encountering the rigid wall, the reflected wave interacts with the wave generated by the contraction region causing a slight recovery wave in the clockwise direction, completing one cycle.

40

## CHAPTER 5: ELECTRO-DYNAMIC SUCTION PUMPING

## 5.1 Introduction

Dynamic suction pumping is characterized by a bidirectional passive elastic wave and a non-linear relationship between pumping frequency and volumetric flow rate. This pumping mechanism has been proposed as the driving mechanism for the vertebrate embryonic heart at the tubular stage. Peristalsis has also been preposed as the mechanism by which embryonic tubular hearts drive the flow of blood. In this study, we consider the tubular, valveless heart of Ascidians (sea squirts). Ascidians are invertebrate chordates, and we will be focusing on the species *Clavelina picta* and *Ciona intestinalis*. These hearts operate at a Womersley numbers ranging from 0.1-5. We investigate traditional dynamic suction pumping on these small scales and show computationally and experimentally that significant flow is not achieved. We propose a different pumping mechanism that couples traveling waves of depolarization to the contraction of the boundary and is similar to peristalsis. Active contractile waves replace passive elastic waves, but the resulting kinematics are similar to dynamic suction pumping. This pumping mechanism can be computationally shown to drive fluid flow at the low Womersley numbers found in Ascidian hearts. We can then improve upon this mechanism by adding a rigid boundary which surrounds the elastic pumping region. This boundary is a simple model of the pericardium, a rigid, pressurized, fluid filled structure which encloses most chordate hearts. We see that this added structure reduces back flow and aneurysms created by traveling wave of contraction driving the motion of a viscous dominated fluid.

## 5.2 Neuromechanical pumping

This pumping mechanism is a means to numerically model the actual tubular valveless heart found in Asicdians: *Clavelina picta* and *Ciona intestinalis*. In previous numerical models of these pumping mechanisms attention has been made to parameters inherent in numerically modeling an ideal valveless pumping mechanism, but no work had previously been done to accurately model the
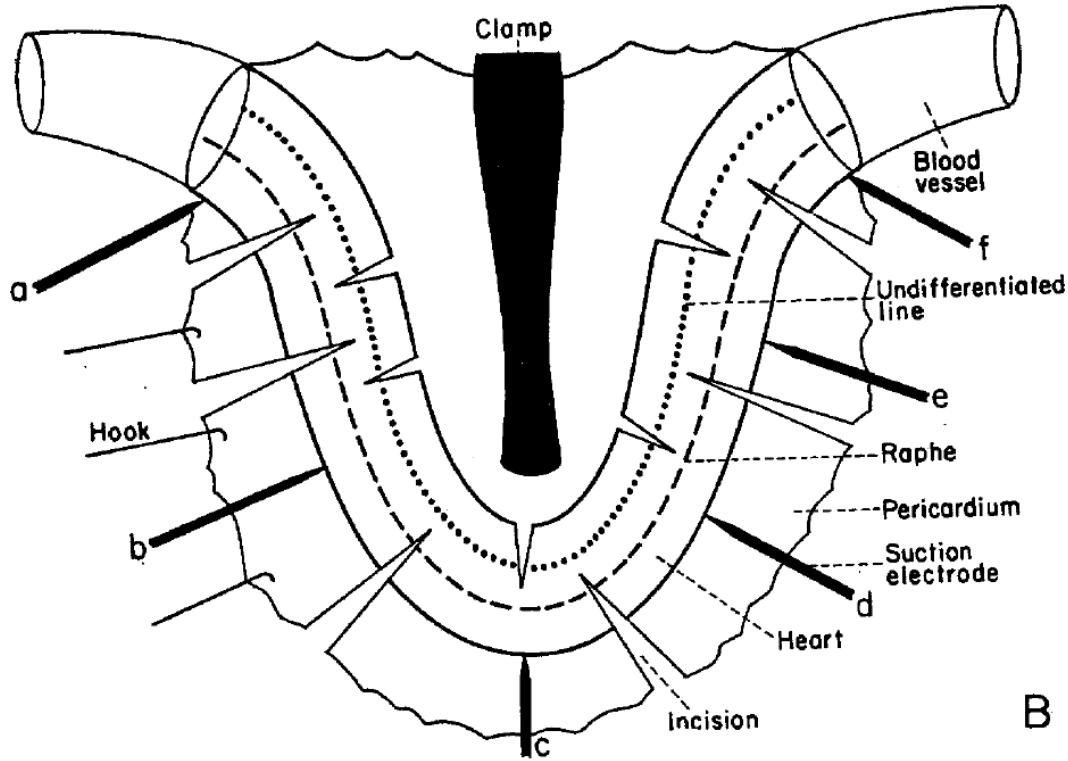
Figure 5.2.1: A figure detailing the experiments used to measure traveling action potential in the *Ciona intestinalis* heart tube. The heart is dissected out of the body and the top pericardium removed. Electrodes are then inserted at each point a-f and used to measure the traveling action potential along the length of the heart tube.[21]

organisms heart tube. Dynamic suction pumping is characterized by a singular active contraction region, passive traveling waves, and a non-linear frequency volumetric flow rate relationship. Peristalsis is characterized instead by active contractions down the length of the pumping domain and a linear frequency volumetric flow rate relationship. We wanted to combine some of the characteristics of both these pumping mechanisms, namely: active contractions of peristalsis and non-linear frequency volumetric flow rate relationship found in dynamic suction pumping. Traveling actions potentials have been recorded in *Ciona intestinalis* hearts in previous studies by Kriebal et al.[21], see figure 5.2.1. These traveling action potentials are known to cause muscle contractions, and this provides support for the idea that that active contractions along the length of the heart tube can augment the movement of blood. A complete mathematical model of the Ascidian heart should then incorporate both the fluid dynamics, elastic properties of the tube, and the activation of contractile muscles along its length. The goal of this chapter of the dissertation is to test the

ability of this pumping mechanism to transport fluid at the $Wo$ scales found in Ascidian hearts.

To begin modeling this system, we first need to describe how to best model traveling action potentials in a heart tube. The Hodgkin-Huxley equations were the first quantitative model of propagation of an electrical signal along excitable cells, such as cardiac muscle cells found in the Asicdian heart tubes[14]. The essential dynamics of this model have since been captured by the dimensionless FitzHugh-Nagumo equations[10], given by:

$$\frac{\partial v}{\partial t} = \mathcal{D}\nabla_x v + v(v - a)(v - 1) - \omega - \mathcal{I}(t) \tag{5.1}$$

$$\frac{\partial \omega}{\partial t} = \epsilon(v - \gamma\omega), \tag{5.2}$$

where $\mathcal{D}$ = diffusion rate of potential, $v(x, t)$ = membrane potential, $\omega(x, t)$ = blocking mechanism, $a$ = threshold potential, $\gamma$ = resetting rate, $\epsilon$ strength of blocking, and the initial condition $\mathcal{I}(t)$, which is a function of time and represents the applied current in the system generated from the pacemaker. Here $v$ repressents the fast variable (potential) and $\omega$ represents the slow variable (sodium gating), the kinetics of which are controlled by the parameter: $\epsilon << 1$. Phase portraits of this non-linear system have been shown to capture the dynamics of cardiomyocytes.
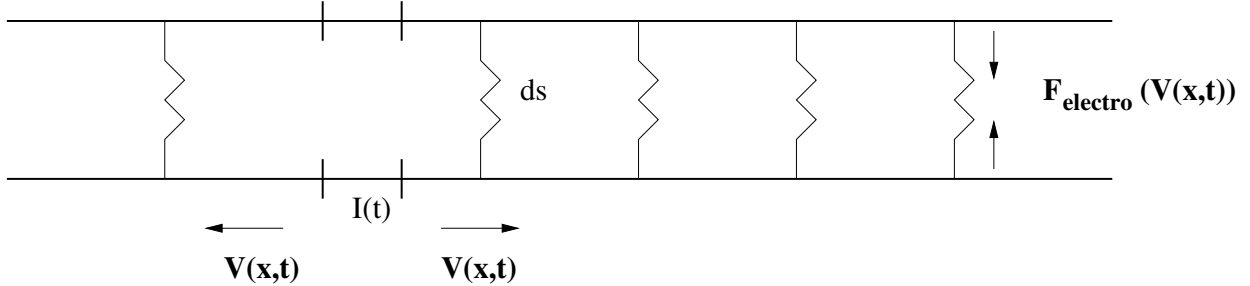


Figure 5.2.2: This diagram shows our numerical model of the coupled dynamics problem. We attach springs to to the top and bottoms elastic walls of the tube to and a force proportional to the traveling action potential, $F_{electro}(V(x,t))$. We then inject a current, $I(t)$, at a location of the pacemaker periodically throughout the simulation. The FitzHugh-Nagumo equations are solved along the tube walls to determine the electropotential at each position and at each time. The force is generated by changing the stiffness of these springs, and results in contractions down the length of the tube wall.

To couple the applied force that drives the movement of the boundary to the electropotential given by the FitzHugh-Nagumo equations, please refer to figure 5.2.2. To begin we create a model
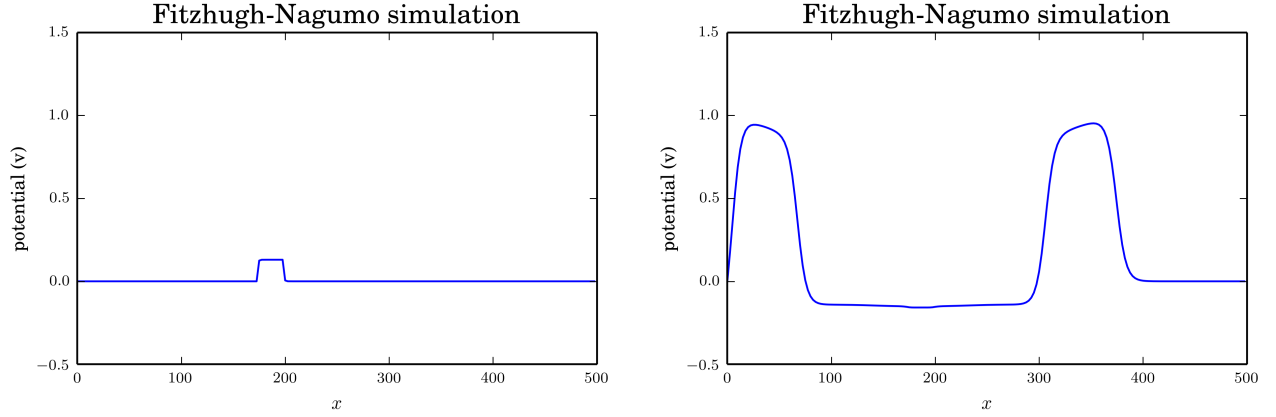
Figure 5.2.3: The figure on the left shows an initial current begin initiated in the pacemaker region. The figure on the right shows the bi-directional propagation of the action potentials down the length of the domain. All parameters are dimensionless for this figure.

racetrack with an active pumping region along the bottom straight elastic portion of the track. We then connect springs with variable stiffness that depend on the action electropotential to the top and bottom of the elastic section of tube. The stiffnesses are function of the traveling electropotential which varies in time due to the current applied to the pacemaker region. At each time step we solve for these potentials by discretizing the FitzHugh Nagumo equations as follows:

$$v_i = v_{i-1} + dt_f (\mathcal{D}(\frac{v_i - 2v_{i-1} + v_{i-2}}{dx_f^2}) - v_{i-1}(v_{i-1} - 1)(v_{i-1} - a) -_{i-1} + \mathcal{I}_i \tag{5.3}$$

$$_i =_{i-1} + \epsilon dt_f (v_{i-1} - \gamma \omega_{i-1}). \tag{5.4}$$

Here we use a forward Euler time step integrator and a centered differencing scheme to represent the spatial diffusion operator. Dynamics of this system can be seen in figure 5.2.3. The other parameters are prescribed to capture the associated dynamics observed in the Ascidian heart tubes.Time is scaled in order to match the dynamics of the generated action potentials to the desired active wave of contraction and is given by:

$$dt_f = \frac{dt\mathcal{F}}{\mathcal{T}}, \tag{5.5}$$

where $\mathcal{F}$ is a non-dimensional scaling parameter and $\mathcal{T}$ is the desired pumping period. The spatial location, x, is also scaled in order to match the desired dynamics of the active wave of contraction. Once we calculate the electropotential, at a given point in space, we can determine the spring stiffness at time t using the equation

$$\kappa_e(x,t) = \kappa_m(v^4(x,t)). \tag{5.6}$$

In this model, $\kappa_m$ is the scaled spring stiffness and $v(x,t)$ is the traveling action potential. This new spring stiffness will then be used to calculate the force generated by the springs that connect the bottom and top of the elastic tube, generating a wave of active contraction.

Table 5.1: Non-dimensional parameter values used for solving the FitzHugh Nagumo equations and constructing the pericardium. Parameters were tuned to match the dynamics of the Ascidian heart.

| Parameter | Value |
| --- | --- |
| Threshold potential ($a$) | 0.1 |
| Strength of blocking ($\epsilon$) | 0.1 |
| Diffusion coefficient ($\mathcal{D}$) | 100 |
| Resetting rate ($\gamma$) | 0.5 |
| Current injection ($\mathcal{I}$) | 0.5 |
| freq (f) | 0.1-2.1 Hz. |
| Pericardium width ($\hat{\mathcal{P}}$) | 1.5-2.5 |

### 5.2.1 results

The goal of this section of work is to compare our neuromechanical pumping model with active contractions to traditional dynamic suction pumping for the scales found in our recorded Ascidian hearts: $Wo \leq 1$. Immersed boundary simulations of neuromechanical pumping and dynamic suction pumping were conducted, and the Wo was changed by carrying the viscosity of the fluid. The actuation site used for dynamic suction pumping coincided with the placement of the pacemaker used for neuromechanical pumping. The pacemaker is modeled as a periodic applied current $\mathcal{I}(t)$ that triggers the propagation of action potentials along the heart tube. This is distinctly different

from dynamic suction pumping and our model of peristalsis where the pumping dynamics are due to: the elastic properties of the tube (passive), or due to the active contraction of our model muscles that are triggered by changes in the local electropotential.

The first simulations presented are matched to the $Wo$ of *Clavalina picta* ($Wo = 0.3$) and a pumping frequency of 2.5Hz. To compare the performance of the pumping mechanisms, the average velocity is taken along a cross section of the diameter of the tube in a non-contracting region. This is then related to the volumetric flow rate by a constant scale factor. Comparing the average velocity over the simulation time, it is clear that neuromechanical suction pumping outperforms dynamic suction pumping, see figure 5.2.4. At $Wo = 0.3$, the passive elastic traveling wave characteristic of dynamic suction pumping is damped by the shear forces encountered from the high viscosity of the fluid. Passive tracer particles inserted into the tube also show that the flow is close to reversible. The particles are moved away from the actuation site during contraction but are pulled back towards the actuation site during expansion. The near-reversibility of the flow due to the lack of significant inertial effects means that dynamic suction pumping is not very effective at low Wo. The use of active contractions implemented as an applied force due to the action of cardiomyocytes greatly enhances the average flow rates at the scales found in *Clavalina picta*, figure 5.2.4

It is also worthwhile to compare the neuromechanic pumping to prescribed peristalsis. In these simulations, the motion of the peristaltic contraction is prescribed using target points. Due to the number of target points passive elastic waves are prevented. An inspection of figure 5.2.6 shows that the magnitude of flow produced by both pumping mechanisms is similar. Also of note is that the neuromechanic pump produces significant back flow which isn't apparent in our peristalsis model. From figure 5.2.6, neuromechanic pumping displays a non-linear frequency volumetric flow rate relationship. This is different than the linear relationship possessed by peristalsis.

## 5.3   Pericardium

We now look to add more biological structure to our model by including relatively stiff pericardium that encloses the heart of most chordates. The motivation for adding the pericardium is do to some differences between the experimentally observed and numerically generated resulting flows. These differences include: the presence of significant back flow and the presence of aneurisms and
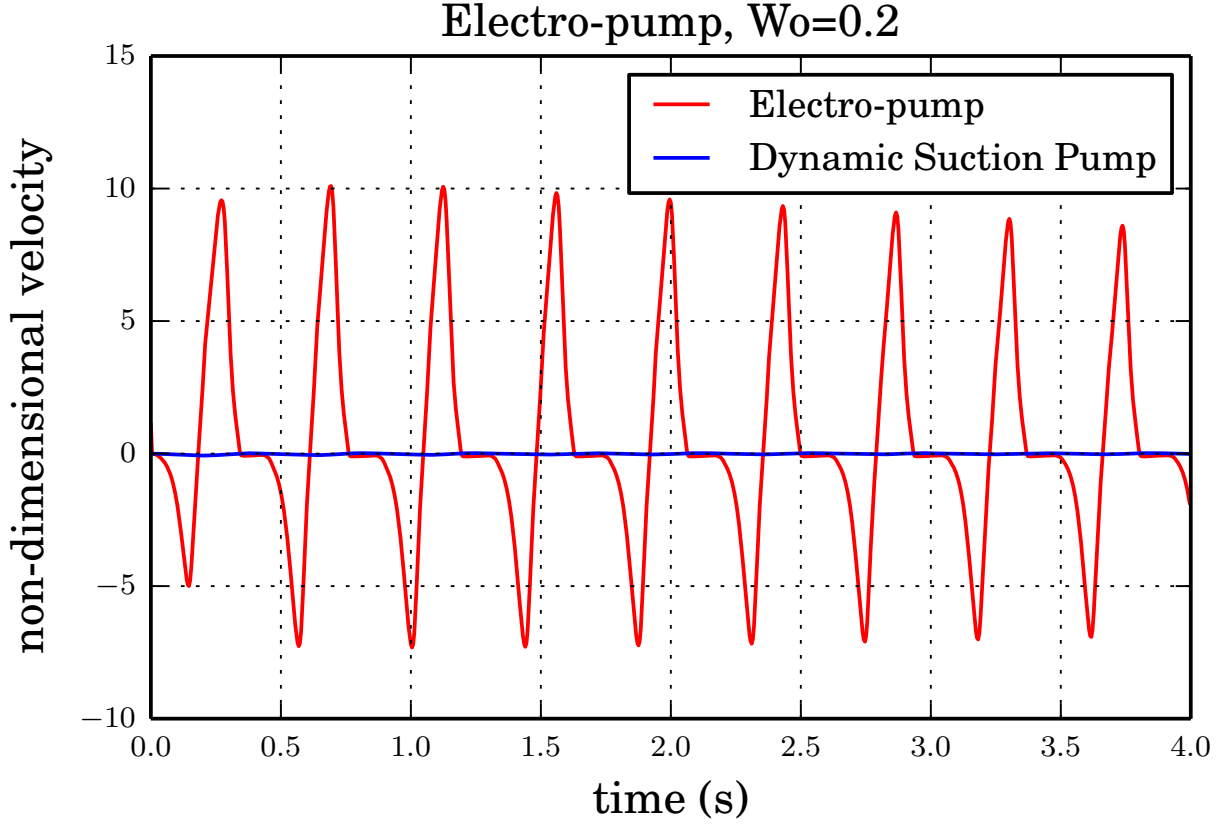
Figure 5.2.4: This graph allows one to compare traditional dynamic suction pumping to the neuromechanical pump. We non-dimensionalize the velocity by dividing dividing it by the characteristic velocity: $\mathcal{U} = \frac{\mathcal{T}}{d}$. $\mathcal{T}$ is the pumping period, or $\frac{1}{f}$ with $f = 2.5$Hz. It is very clear that neuromechanical suction pump out preforms our original dynamic suction pumping for $Wo = 0.2$.

kinks in the pumping region. Both of these issues are not apparent in observations of the Ascidian heart with an intact pericardium. Between this rigid enclosure and the elastic pumping heart tube is pressurized fluid. Preliminary experimental studies suggests that this structure is essential for driving net flow in smaller tubular hearts. Any disruption of this pericardium results in a significant drop in net flow and the generation of aneurysms or kinks in the heart tube.

To model this rigid enclosure, we place target points along a box enclosing the elastic pumping region. Fluid is present between the model pericardium and the elastic tube. As the elastic region deforms, pressure builds up in the region between the pericardial walls and the elastic tube (see figure 5.3.1). Adding this structure greatly reduces back flow at low Wo (see figure 5.3.1). The back flow is now on the same order as the peristaltic pump, see figure 3.1.1. We also see a reduction
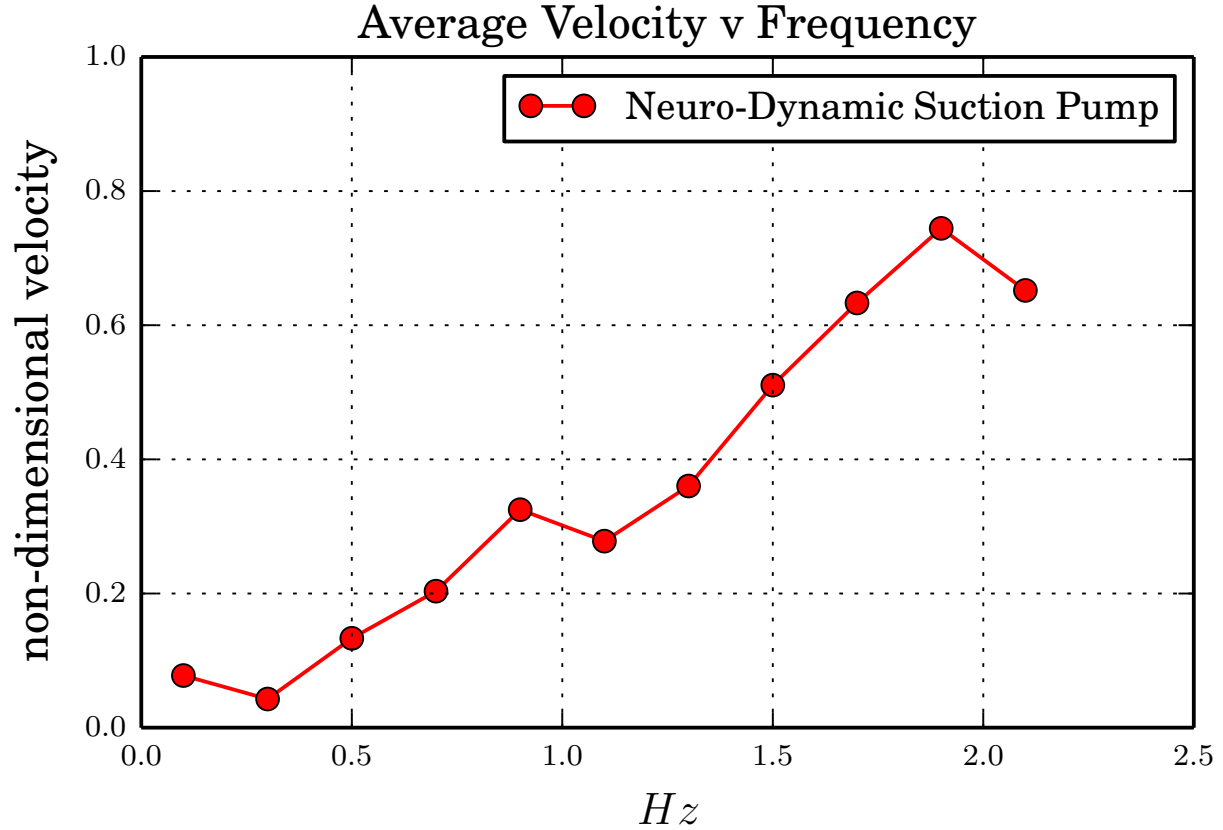
Figure 5.2.5: Average dimensionless flow rate vs. frequency of pumping with fixed viscosity and tube geometry.The frequency was done in order to investigate the non-linear frequency flow relationship of the electro-dynamic pump. It seems to exhibit some non-linear behavior for certain frequencies. This follows the dynamics of traditional impedance pumping and is a characteristic which differentiates this mechanism from peristalsis.

in the size of aneurisms produced and the resulting motion more closely matches the contractions observed in Ascidian hearts.

We run these simulations to mirror preliminary experimental results done for *Ciona intestinalis* by matching the non-dimensional number $Wo = 0.9$. Figure 5.3.3 shows magnitude of non-dimensional vorticity for pericardium neuromechanical pumping. The current is injected periodically in the top left frame and then the pumping dynamics are completely determined by the elastic structure of the tube wall and the dynamics of the FitzHugh-Nagumo equations. The traveling action potentials create bi-directional traveling waves along on the length of the straight tube in the top right and bottom left frames. As these waves reach the end of computational boundary their magnitude
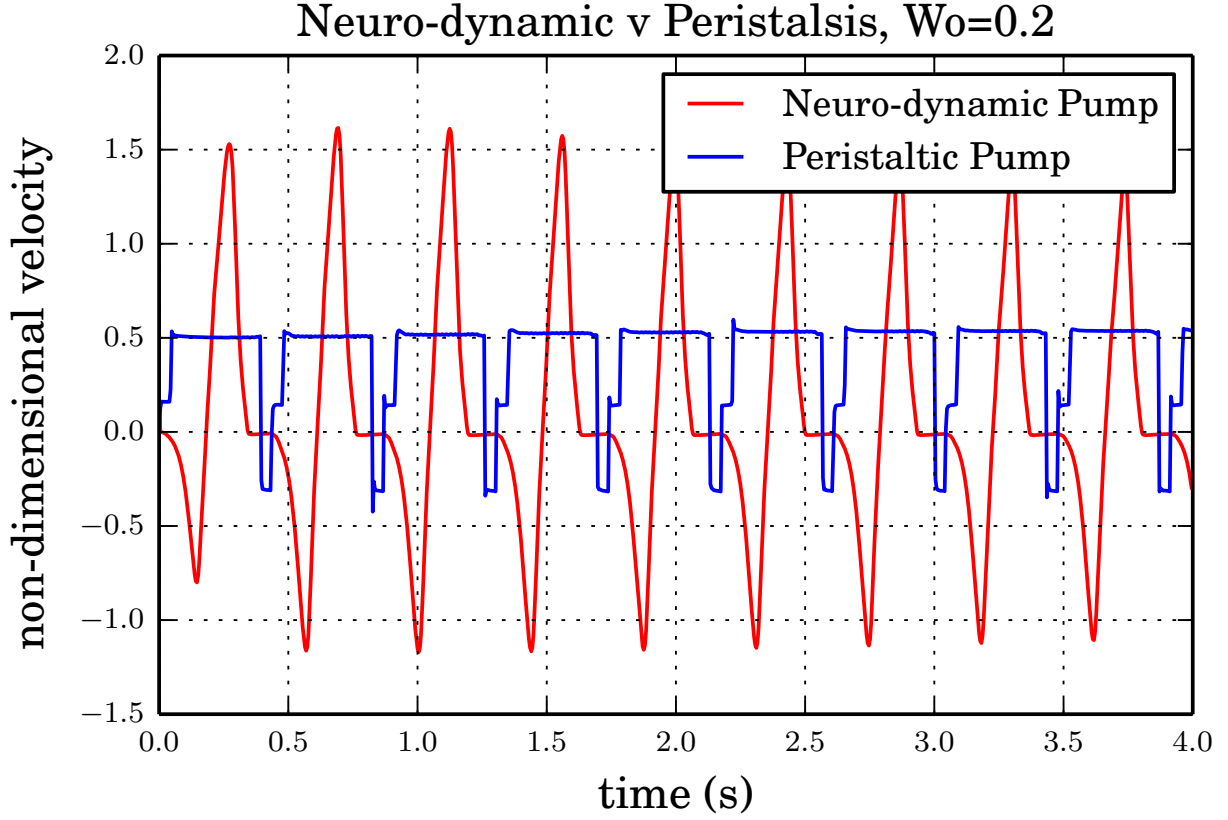
Figure 5.2.6: Dimensionless velocity averaged across a section of non-contracting tube as a function of time for both neuromechanical pumping and peristaltic pumping. We non-dimensionalize the velocity by dividing it by the characteristic velocity: $\mathcal{U} = \frac{d}{\mathcal{T}}$. Here $\mathcal{T}$ is the pumping period, or $\frac{1}{f}$ for $f = 2.5\text{Hz}$. The two pumping mechanisms drive flows of similar magnitude.

decreases and the system resets itself. The neutrally buoyant particles in the fluid display the flow induced by this pumping mechanism.

We also investigate how the width of the pericardium, $\mathcal{P}_{\text{width}}$, affects the bulk flow generated by neuromechanical pumping. In figure 5.3.2 we can see that, in fact, flow velocity is a function of the width of the pericardium with maximum flow occurring hen the pericardium s about 2.4 times the width of the heart time. This corresponds to some preliminary results taken from *Ciona intestinalis* that shows hat the maximum flow rate is produced when the pericardium is about 2.5 times the diameter of the heart tube.
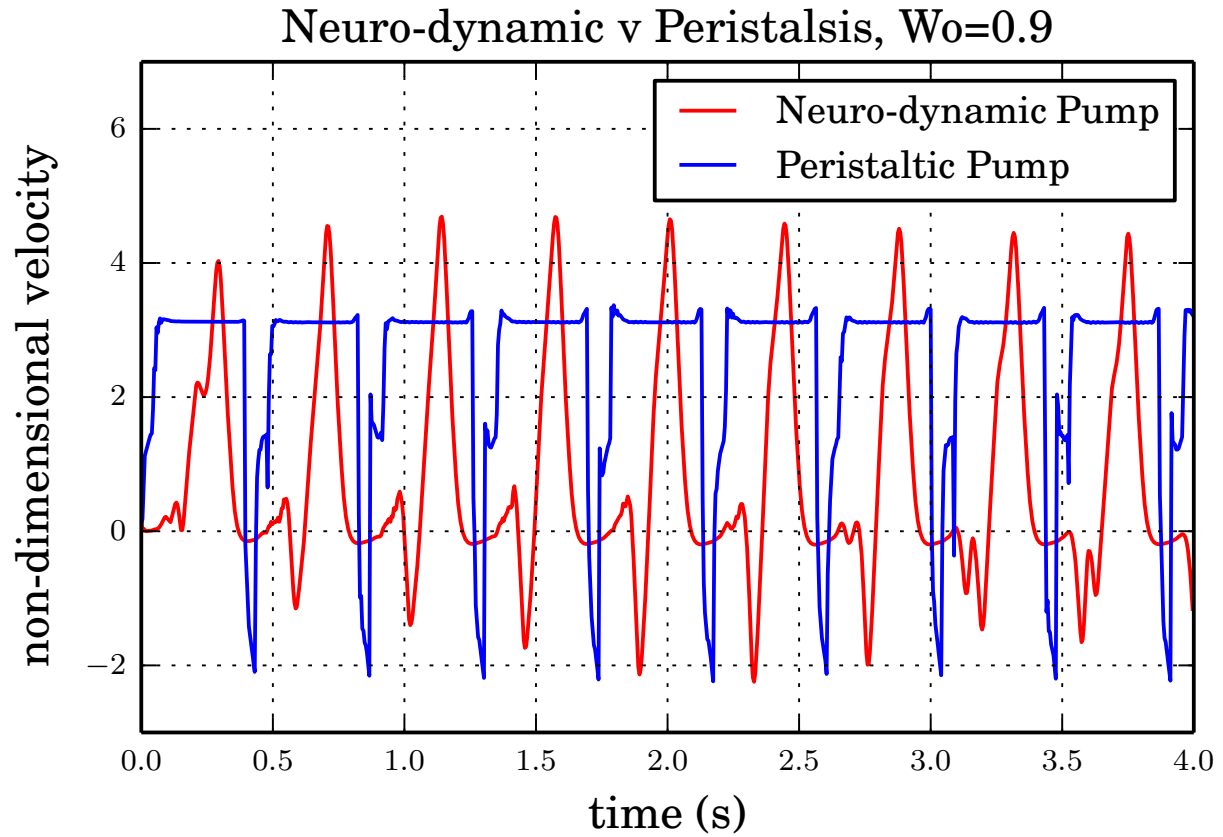
Figure 5.3.1: An neuromechanicalmechanism with pericardium is compared to peristaltic pumping. The back flow generated by the pump without the pericardium is greatly reduced and is on the order of the back flow produced by peristalsis.
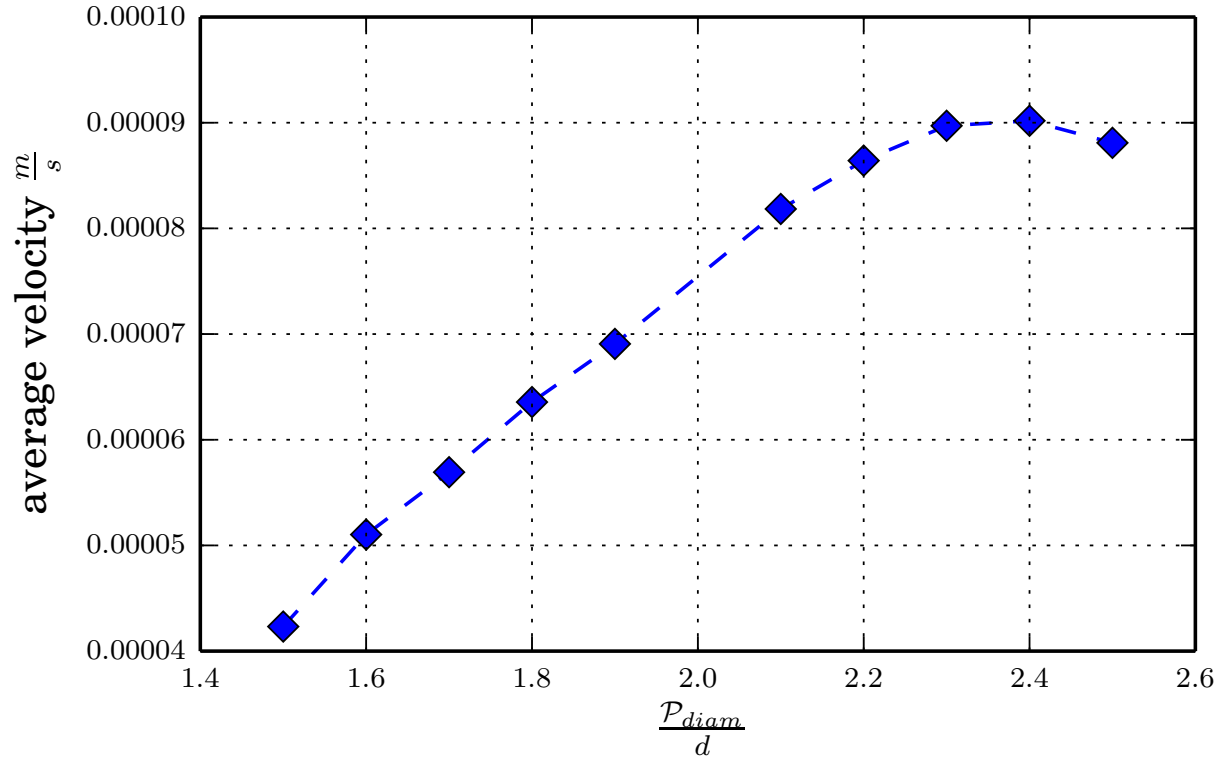
Figure 5.3.2: This figure displays the average velocity as a function of the non-dimensional length scale $\hat{\mathcal{P}} = \mathcal{P}d$. This shows how many diameters wide the pericardium is relative to the diameter of the tube. A clear peak is formed for a set pericardium size, showing that average flow is a function of the width of this rigid region. All data points were obtained for $Wo = 0.9$.
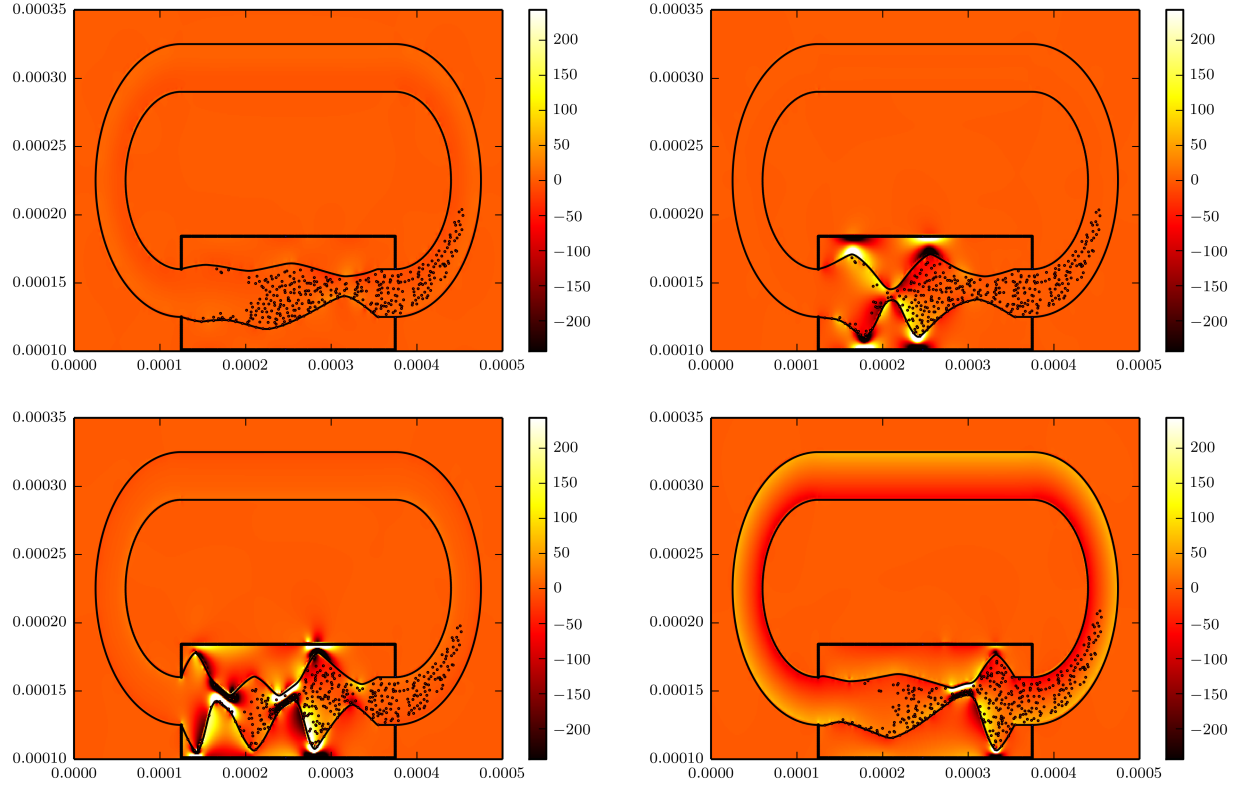
Figure 5.3.3: These frames show one period of neuromechanical mechanism when the elastic tube modeling the heart is enclosed by a rigid pericardium for $Wo = 0.9$ which is the same scale seen in *Ciona intestinalis*. The frames begin with the start of one pumping period. The top left frame displays the tube at rest for $t = 0.6$ simulation time and the pumping continues in the clockwise direction for $t = 0.7, t = 0.775, t = 0.85$ respectively.

# CHAPTER 6:   CONCLUSION

The main purpose of this dissertation was to model various valveless pumping mechanisms and answer the following questions: determine which pumping mechanism is used in small tubular hearts, similar to those found in developmental vertebrate hearts, does this mechanism depend upon the scale of the application, and what improvements can be made? We began by modeling impedance pumping, which is defined to have an isolated region of active contractions with passive traveling elastic waves generated from the pacemaker site. This mechanism was compared to peristalsis using non-dimensional matching to Ascidian heart tubes to determine efficacy. Peristalsis was simulated by using active forcing down the length of the tube to simulate muscle contractions traditionally seen in this mechanism. Average volumetric flow rate was computed for $Wo < 1$ for both impedance pumping and peristalsis and it was clear that the lack of inertia in the fluid due to the small non-dimensional scales rendered impedance pumping completely ineffective.

A new mechanism was modeled which incorporated the non-linearity of volumetric flow rates to frequency of pumping seen in impedance pumping and the active muscle contractions used to compress the tube seen in peristalsis. Similar parameters were computed and comparisons were made to peristalsis and impedance pumping. This mechanism was able to reach similar flow rates seen in peristalsis, but with significant back flows and aneurysms apparent in the tube. To reduce these issues we modeled a ridged outer layer around the elastic pumping region in an attempt to model the pericardium found in Ascidian hearts. The pericardium both reduced back flow and aneurysms in the pumping mechanism while still retaining significant flow.

## 6.1   Dynamic suction pumping vs. peristalsis for low $Wo$

Parameter sweeps for Womersley numbers ranging from 0.1 to 50 were numerically simulated for two different valveless pumping mechanisms: peristalsis and dynamic suction pumping. The motion of the active contraction regions for each case were prescribed in a model racetrack, and the fluid-structure interaction problem was handled using the immersed boundary method. The

ratio of the tube diameter to length and the Womersley number play a significant role in the net flow rates generated by dynamic suction pumping. For $Wo < 1$, negligible net flow was generated by dynamic suction pumping for the parameters considered in this this thesis. Intermediate $Wo$ between $10^0$ and $10^1$ were characterized by rapid reversals in the direction of net flow as the $Wo$ and the tube diameter were changed. Average flow speeds were reduced for tubes with larger diameter to length ratios. The $Wo$ range at which average flow was generated in the negative direction tended to decrease as the diameter to length ratio increased. In contrast, peristaltic pumping generated significant net flow in the positive direction for all $Wo$ considered. Since the $Wo$ was varied by changing the viscosity of the fluid only, the average flow velocities were relatively constant for $Wo < 1$. Due to the effects of inertia that allowed for flow between periods of active contraction for $Wo > 1$, the average flow speeds increased with increasing $Wo$.

## 6.2   Discussion of impedance pumping and flow direction

Previous work analyzing impedance pumping has considered a variety of parameters that affect the magnitude and direction of flow. Two of these parameters, pumping location and frequency of compression, have both been seen to affect the direction of flow. These previous studies have not directly determined why these parameters influence the net direction of flow. In this chapter of the thesis we focused on two parameters that influence the direction of flow: the frequency of actuation and the diameter to length ration of the elastic part of the tube. The dimensionless length scale $\hat{\mathcal{L}}$ was set to the ratio of the diameter to the length of the elastic section of tube. We changed $\hat{\mathcal{L}}$ by altering the diameter of the tube and kept the pumping frequency and non-dimensional material parameters, fixed. The transition from clockwise to counter clockwise flow is seen for two different non-dimensional length scales $Wo = \{5, 10\}$, and this has not previously been reported to affect flow direction.

We then investigated whether or not driving the tube at the resonant frequency of the short or long sections determines the direction of net flow. Loumes et al. [22] was one of the first studies to consider whether or not resonating the elastic tube produces maximum flow in the counterclockwise direction. To induce maximal net flow in the counterclockwise direction we pursue this work further by investigating the affects of not only resonating the entire tube but also considering the resonant

behavior of the sections on either side of the actuation site. Our hypothesis was that resonating either side of the tube would drive flow in that direction. We measure the first and second modes of the long and short sections of the tube by initializing the boundary with a displacement that will excite either the first or second mode and then allowing the tube to vibrate freely. The oscillations of the tube were recoded and a Fourier analysis was preformed to extract the resonant frequencies. Peak flows in each directions generally occur near a resonant of the short or long section. It's important to note that because of the non-linear effects of the surrounding fluid, the oscillations induced by the initial displacement do not exhibit a single clearly defined resonant frequency. The frequency of vibration is amplitude dependent, which is characteristic of nonlinear elastic systems. The resulting power specra shows a range of frequencies with large coefficients, indicating the resonant behavior spans a large bandwidth. In the graphs we highlighted regions around the maximal peaks for each resonant section. These highlighted regions overlap with the maximal flow in each direction for pumping locations which clearly create short and long flexible sections surrounding it.

The three main dimensionless parameters in our analysis, non-dimensional length scale, $\hat{\mathcal{L}}$, pumping location, $\alpha_2$, and pumping frequency were significant for determining the flow direction in impedance pumping. We were able to show that driving the flexible tube as its resonant frequency can often determine flow direction for. In the future we would like to extend this work or the smaller scales found in most tubular hearts, $Wo < 5$. Our results also show that one can tune the impedance pump to obtain strong flows t low pumping frequencies to optimize pump efficiency. This study could be extended by considering non-dimensional bending ($\hat{\kappa_{beam}}$ )and stretching stiffnesses ($\hat{\kappa_{spring}}$) separately to determine how each affects flow direction.

## 6.3 Electro-dynamic pumping and the role of the pericardium

To capture more of the dynamics of an actual heart tube, we added more complexity into our pumping mechanism. We began by adding traveling action potentials that had previously been recorded in *Ciona intestinalis* hearts [21]. A mathematical model of excitable cell dynamics as developed to drive the contraction of the heart tube. Specifically, we used the FitzHugh-Nagumo equations and chose parameters that would simulate the action potentials experimentally recorded in Ciona. The computed traveling action potentials were used to determine the effective spring

stiffness of simple model muscles. As an action potential arrived in a region of the heart tube, the spring stiffness increased which drove the contraction of the tube. As he electropotential returned to rest, the spring stiffness decreased. This resulted in the passive re-expansion of the heart tube until the next action potential arrived.

Peristaltic pumping has been shown to be effective at transporting fluid at the small scales seen in Ascidian hearts. It is defined as using an active traveling wave of contraction to push fluid. If the deformations are sufficiently small, the maximum flow velocities are less than or equal to the speed of the contraction wave. Recently, data recorded from *in vivo* experiments of zebrafish hearts how flow velocities exceed those of the contraction wave. A bi-directional contraction wave as well as a non-linear relationship between frequency and flow were also observed. These results supported the claim that tubular hearts use valveless suction pumping. We created a pump which captures dynamics of both peristalsis and dynamic suction pumping: bi-direction wave propagation, a non-linear frequency-flow relationship, and flow velocities that are higher than the contraction wave speed. This mechanism is also effective at small scales.

With this model we were able to see that for $Wo = 0.3$ and $Wo = 0.9$ electro-dynamics pumping outperformed traditional dynamic suction pumping and was able to achieve flow magnitudes equal to a peristaltic pump. This mechanism was able to effectively transport fluid at extremely small $Wo$ and incorporating some of the features of the contracting myocardial cells. Although this new model for the contractions of the boundary created promising results, many issues still remained: significant back flow and aneurisms along the boundary.

To mitigate these issues we turned back to the organism and noticed a rigid encasing around the pumping region. We incorporated this new structure into our model by creating a rigid boundary around the elastic pumping region. This boundary is connected to target points to keep it stiff. With the addition of this boundary, fluid was transported at a similar velocity to that of peristaltic pumping for $Wo = 0.3$ and $Wo = 0.9$. The vast majority of back flow was also eliminated. Aneurisms along the elastic tube was were substantially reduced, although work still needs to be done to fully duplicate the Ascidian heart tube.

## 6.4    Future work

Future work is needed to accurately simulate the dynamics of pumping in actual tubular hearts. For example, most tubular hearts contain helically wound muscle fibers which induce a distinctly three dimensional contractile motion. Compression tends to be a wrapping constriction, and the angle these muscles fibers contract relative to the x-axis is something which has been measured in previous experiments [21] but has not been explored mathematically. As such this three dimensional motion would be an ideal extension of our study. Also absent is any attempt to accurately model the muscle dynamics beyond prescribing the motion of the contracting sections of the tube. A variety of mathematical muscle models could be applied to drive the motion of the tube walls, yielding a more accurate model of tubular hearts. Another interesting area of future research would to be to explore the magnitude and direction of net fluid flow for dynamic suction pumps at intermediate Womersley numbers ($1 < Wo < 10$). The diameter to length ratio of the flexible heart tube also appears to be a critical parameter in determining the magnitude and direction of the fluid flow that could have interesting consequences for organisms.

## APPENDIX A: IMMERSED BOUNDARY METHOD

This appendix will describe a full derivation of the Navier Stokes equations and then detail the numerical and analytical description of the immersed boundary method. It is a means to get the finer details of how we describe a fluid in this thesis and how we couple the fluid to the movement of the boundary. The second appendix details coding implementation of the immersed boundary in python using the built in FFT modules.

### A.1    Conservation of Mass

The major idea of the conservation of mass is that mass in a fixed region cannot be created or destroyed. Therefore, and change in mass can only occur with infow or outflow of particles in the system. To derive the conservation of mass equations mathematically we begin with a fixed volume in space $V$ whose mass is defined to be

$$\int_V \rho dV \tag{A.1}$$

We can then determine the rate of increase of mass inside the fixed volume by taking a time derivative:

$$\frac{d}{dt}\int_V \rho dV = \int_V \frac{\partial \rho}{\partial t} dV \tag{A.2}$$

The derivative can be taken inside the integral since we are dealing with a fixed volume. We can then write the rate of mass flow out of the volume as:

$$\int_A \rho \mathbf{u} \cdot \mathbf{dA} \tag{A.3}$$

The dot product tells us how much two vectors are alike, or in this case, how much fluid is traveling across the boundary $A$ of our volume. also note that $\mathbf{u} = (u_1(x,y,z,t), u_2(x,y,z,t), u_3(x,y,z,t))$, this indicates that our fluid velocity in each spatial direction is a function of where it is in space

and time. We can now equate these integrals since fluid flux through the boundary is equal to the change in density of our fixed volume.

$$\int_V \frac{\partial \rho}{\partial t} dV = -\int_A \rho \mathbf{u} \cdot d\mathbf{A} \tag{A.4}$$

We now have an equation for change of mass in our fixed volume, but the integral on the right hand side is a surface area integral whereas, the left hand side integral is a volumetric one. We will now invoke the divergence theorem to get both integral in terms of volume.

$$\int_A \rho \mathbf{u} \cdot d\mathbf{A} = \int_V \nabla \cdot (\rho \mathbf{u}) dV \tag{A.5}$$

With this relation we can now right equation (4) as

$$\int_V \left[ \frac{\partial \rho}{\partial t} + \nabla \cdot (\rho \mathbf{u}) \right] dV = 0. \tag{A.6}$$

For this equation to equal zero, then the integrand must go to zero and this gives us the *continuityequation*. One of the more well known forms of this equation is written as:

$$\frac{1}{\rho} \frac{D\rho}{Dt} + \nabla \cdot \mathbf{u} = 0. \tag{A.7}$$

Note that the capital D in this equation is called the *materialderivative*, this operator is defined to be

$$\frac{D}{Dt} = \frac{\partial}{\partial t} + \mathbf{u} \cdot \nabla \tag{A.8}$$

This equation denotes time rate of change of an object moving through the fluid. Many things
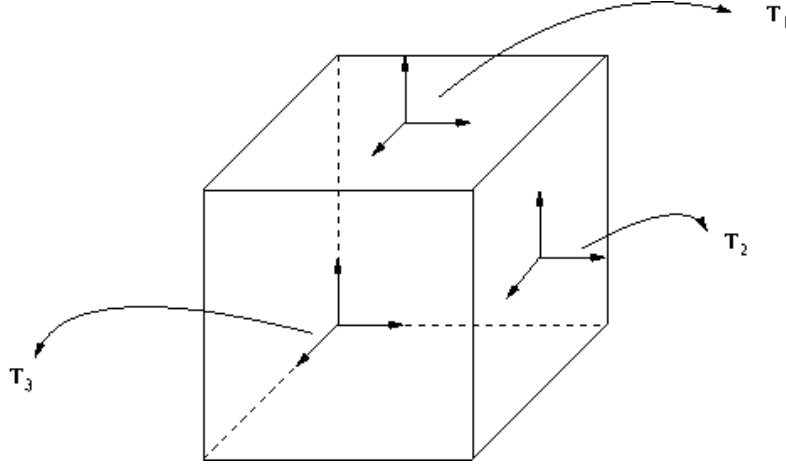
Figure A.2.1: Each $\tau$ vector corresponds to the stress in the x-direction on each side of the particle.

can have a meaningful material derivative. Density, velocity, temperature are some examples of objects which describe the fluid that can have meaningful material derivatives. For an incompressible fluid the continuity equation changes. This is because an incompressible fluid doesn't change its density due to a change of pressure. This causes $\frac{1}{\rho}\frac{D\rho}{Dt} = 0$ leading to the more familiar form of the continuity equations, for an incompressible fluid: $\nabla \cdot \mathbf{u} = 0$.

## A.2  Conservation of Momentum

Idea: Use Newtons second law stating that the force on an object is equal to mass*acceleration of our fluid element. To consider forces we need to figure out the stress on a fluid element. We then know that the forces on the fluid element must equal its force times its acceleration. The stress is a force being applied to the boundary of the fluid particle. Each side of our fluid element feels stress in each direction, x, y, z. We will only derive the stress in the x-direction but the other directions can be obtained similarly.

We will now sum the forces for each side.

$$
\begin{aligned}
&\left( \tau_{11} + \frac{\tau_{11}}{x_1}\frac{dx_1}{2} - \tau_{11} + \frac{\tau_{11}}{x_1}\frac{dx_1}{2} \right) dx_2 dx_3 \\
&+ \left( \tau_{21} + \frac{\tau_{21}}{x_2}\frac{dx_2}{2} - \tau_{21} + \frac{\tau_{21}}{x_2}\frac{dx_2}{2} \right) dx_1 dx_3 \\
&+ \left( \tau_{31} + \frac{\tau_{31}}{x_3}\frac{dx_3}{2} - \tau_{31} + \frac{\tau_{31}}{x_3}\frac{dx_3}{2} \right) dx_1 dx_2
\end{aligned}
$$

60

We can now cancel terms and reduce. Also notice that we are taking the stress at a point and multiplying by the area of the face that they are on. This will give us the stress on the entire face of the fluid particle. This gives us the equation:

$$\left(\frac{\tau_{11}}{x_1} + \frac{\tau_{21}}{x_2} + \frac{\tau_{31}}{x_3}\right) dx_1 dx_2 dx_3$$

We can write this in more general tensor notation:

$$\frac{\tau_{j1}}{x_j} d\mathcal{V}$$

In this notation the repeated indices mean to sum over our range of $j$'s, in three dimensions $j = [1, 2, 3]$. Also note that because the second index is a 1 this equation is only valid in the x-direction. More generally still, we can write this as:

$$\frac{\tau_{i,j}}{x_j} d\mathcal{V}$$

Note that $\tau_{i,j} = \tau_{j,i}$ and is a second degree tensor, in other words, it is a 3x3 matrix equation containing information about the stress in all directions for each surface. Now that we have a complete representation of the stress on the surface of our fluid element we can finally write the equation of motion for the given fluid element.

$$\rho \frac{\mathrm{D}u_i}{\mathrm{D}t} = \rho g_i + \frac{\tau_{i,j}}{x_j}$$
$$\frac{\mathrm{D}}{\mathrm{D}t} = \frac{}{t} + u \cdot \nabla$$

Note that $\rho g_i$ denotes the forces found in the body of the fluid. Since we are in 3-dimensions: $i, j = (1, 2, 3)$. Also note that the capital D found on the left hand side of this equation is the "material" derivative which is a operator which denotes the time rate of change of the object being differentiated as it travels with the fluid. For this equation the derivative is denoting acceleration of the fluid.

## A.3 Constitutive Equations

A constitutive equation is an equation relating stress and deformation in a continuum, an example being a newtonian fluid. First we want to consider stress acting on a fluid at rest. If we assume no movement then the only normal components of stress exist and our stress tensor is isotropic, or invariant under coordinate rotation. This makes sense because no matter which direction our fluid particle is facing because it's not moving there's no viscous forces and our only components of the stress tensor will be normal components. We can then write our stress tensor as:

$$\tau_{i,j} = p\delta_{i,j}$$

$$\delta = \begin{pmatrix} 1 & 0 & 0 \\ 0 & 1 & 0 \\ 0 & 0 & 1 \end{pmatrix}$$

Here p is the thermodynamic pressure which is an equation of state and non-constant. If we begin considering a moving fluid then we have stress created by viscosity, by fluid particles interacting with eachother. This imply's that we now have off diagonal enteries in our stress tensor $\tau_{i,j}$. We can write this new stress tensor describing a moving fluid as:

$$\tau_{i,j} = -p\delta_{i,j} + \sigma_{i,j}$$

In this equation $\sigma i, j$ is known as the divorac stress tensor. This tensor is intimately related to the fluid velocity gradients, $\frac{u_i}{x_j}$. We can decompose this velocity gradient into its symmetric and anit-symmetric components:

$$\frac{u_i}{x_j} = \frac{1}{2}\left(\frac{u_i}{x_j} + \frac{u_j}{x_i}\right) + \frac{1}{2}\left(\frac{u_i}{x_j} - \frac{u_j}{x_i}\right)$$

The second term in this equation represents the antisymmetric portion of the matrix $\frac{u_i}{x_j}$. This anti-symmetric portion of the matrix only represents fluid rotation, and thus isn't contributing to our off diagonal entries of the stress tensor, denoting deformation. This is when we can define the

strain rate tensor as:

$$e_{i,j} = \frac{1}{2}\left(\frac{u_i}{x_j} + \frac{u_j}{x_i}\right)$$

We can relate this strain rate tensor to the stress tensor as:

$$\sigma_{i,j} = \mathcal{K}_{i,j,m,n}e_{m,n}$$

Here the rank four tensor $\mathcal{K}$ has 81 components and can vary based on the fluid, but for a newtonian fluid only two terms of the 81 survive and we can write our stress tensor as:

$$\sigma = 2\mu e_{i,j} + \lambda e_{m,m}\delta_{i,j}$$

Here $e_{m,m} = \nabla \cdot \mathbf{u}$ is the volumetric strain rate. We now have a representation of our divorac stress tensor in terms of the fluid velocity and viscosity. We can plug this back into our equation for the stress tensor for our fluid and get:

$$\tau_{i,j} = -p\delta_{i,j} + 2\mu e_{i,j} + \lambda e_{m,m}\delta_{i,j}$$

We now need to get an equation for the pressure, since pressure in this sense is thermodynamic pressure and is non-constant and is related to the stress and strain of the fluid. We will see, however, that the difference between averaged pressure and thermodynatic pressure are only significantly different for large density changes. To get a representation of $p$ we will set $i = j$ and sum the repeated indices.

$$\tau_{i,i} = -3p + (2\mu + 3\lambda)e_{m,m}$$

Now we can solve for p.

$$p = -\frac{1}{3}\tau_{i,i} + \left(\frac{2}{3}\mu + \lambda\right)\nabla \cdot \mathbf{u}$$

This is our thermodynamic pressure, but we can get an average pressure by taking an average of the diagonal terms of our stress tensor. This allows us to define the average pressure as: $\bar{p} = \frac{1}{3}\tau_{i,i}$. Now we can explicitly write out how an average pressure and our thermodynamic pressure vary in the fluid:

$$p - \bar{p} = \left(\frac{2}{3}\mu + \lambda\right)\nabla \cdot \mathbf{u}$$

If we consider what is refered to as the bulk viscosity $\kappa = \frac{2}{3}\mu + \lambda$ we can start to understand the differences between thermodynamic pressure and average pressure. It turns out that this term is measurable and is very small unless $\frac{D\rho}{Dt}$ is very large, which only occurs in some select instances. Therefore, we can set this constant to zero and assume that the thermodynamic pressure is equal to the averaged pressure in the fluid. Setting this constant to zero and plugging in our pressure we get a new constitutive equation.

$$\tau_{i,j} = -\left(p + \frac{2}{3}\mu\nabla \cdot \mathbf{u}\right)\delta_{i,j} + 2\mu e_{i,j}$$

We can write this out in matrix form to get a better understanding of the stress tensor.

$$\tau_{i,j} = -\left(p + \frac{2}{3}\mu\left(\frac{u_i}{x_i}\right)\right)\begin{pmatrix} 1 & 0 & 0 \\ 0 & 1 & 0 \\ 0 & 0 & 1 \end{pmatrix} + 2\mu\frac{1}{2}\left(\frac{u_i}{x_i}\right)$$

This is our final form for the stress on a newtonian fluid and now that we have this we can substitute this into Cauchy's equation.

$$\rho\frac{Du_i}{Dt} = -\frac{p}{x_i} + \rho g_i + \frac{}{x_i}\left[2\mu e_{i,j} - \frac{2}{3}\mu(\nabla \cdot \mathbf{u})\delta_{i,j}\right]$$

This is now the general form of Navier-Stokes. $\mu$ is the viscosity and is in general a function of the thermodynamic state and displays strong dependance on temperature. If we can assure that

temperature differences in the fluid are small we can treat $\mu$ as a constant and simplify the equation.

$$\rho\frac{Du_i}{Dt} = -\frac{p}{x_i} + \rho g_i + 2\mu\frac{e_{i,j}}{x_j} - \frac{2}{3}\mu\frac{}{x_i}(\nabla\cdot\mathbf{u})$$
$$= -\frac{p}{x_i} + \rho g_i + \mu[\nabla^2 u_i + \frac{1}{3}\frac{}{x_i}(\nabla\cdot\mathbf{u})]$$

Finally for an incompressible fluid $\frac{D\rho}{Dt} = 0$ and we are able to obtain the more familiar form of the equations.

$$\rho\frac{D\mathbf{u}}{Dt} = -\nabla p + \rho\mathbf{g} + \mu\nabla^2\mathbf{u}$$

$$\nabla\cdot\mathbf{u} = 0$$

We now want to non-dimensionalize in order to get dimensionless parameters to work with. To do this we will make substitutions for velocity, pressure, time, and position.

$$\bar{x} = \frac{\mathbf{x}}{L}$$
$$\bar{u} = \frac{\mathbf{u}}{\mathcal{U}}$$
$$\bar{t} = t\frac{\mathcal{U}}{L}$$
$$\bar{p} = \frac{p}{\rho\mathcal{U}^2}$$

Plugging these substitutions into our equations we are able to get a non-dimensionalized form of the Navier Stokes equations.

$$\frac{\bar{u}}{\bar{x}_i} + \bar{u}\frac{\bar{u}}{\bar{x}_i} = g_i\frac{L}{\mathcal{U}^2} - \frac{\bar{p}}{\bar{x}_i} + \frac{\nu}{\mathcal{U}L}\frac{\bar{u}}{\bar{x}_j\bar{x}_j}$$

Notice that we are now using tensor notation to denote our operators, for example: $\nabla = \frac{}{x_i}$. If we define non-dimensional numbers we can rewrite the equations as:

$$\frac{\bar{u}}{\bar{x}_i} + \bar{u}\frac{\bar{u}}{\bar{x}_i} = \frac{1}{Fr} - \frac{\bar{p}}{\bar{x}_i} + \frac{1}{Re}\frac{\bar{u}}{\bar{x}_j\bar{x}_j}$$

65

Where the non-dimensional numbers are defined to be:

$$Fr = \frac{\mathcal{U}^2}{g_i L}$$

$$Re = \frac{\mathcal{U} L}{\nu}$$

Here Re represents Reynolds number: a dimensionless number that quantifies the ration of inertial forces to viscous forces in the fluid. For large scale fluid applications this number is large since $L$, our characteristic length scale, will be large, similarly, the Reynolds number will be small for very small scale fluid transport.

## A.4 Equations of Motion for an Elastic Incompressible Material

In this section we will describe the motion of an elastic material and how it interacts with our fluid equations. This material's motion will be described in Lagrangian coordinates to better describe its motion. For any elastic incompressible material filling three dimensional space we want to attach a coordinate frame $(q, r, s)$, such that, a fixed value of this coordinate frame $(q, r, s)$ labels a material point. A fixed pair $(q, r)$ designates a fiber. Now let

$$\mathbf{x} = \mathbf{X}(q, r, s, t)$$

be the position at time $t$ of a material point with label $(q, r, s)$. We now want to define the unit tangent to the fibers with respect to this function.

$$\tau = \frac{\mathbf{X}/s}{|\mathbf{X}/s|}$$

We now will denote $T(q, r, s, t)$ to be the fiber tension where $T dq dr$ would be the force from the fibers corresponding to a patch $dqdr$. Note that this force points in the fiber direction, $\pm \tau$.

Due to the elastic properties of the fibers we can say that the fiber tension is related to the fiber strain which is determined by $|\mathbf{X}/s|$. We can then write our tension in the form of a generalized Hooke's law relating stress and strain of a material.

$$T = \sigma(|\mathbf{X}/s|; q, r, s, t).$$

We now can consider the force the fibers apply to the fluid. To begin this derivation we want to begin by considering a collection of fiber segments: $[\mathcal{S} : (q, r) \in \Omega, s_1 \le s \le s_2]$. Here $\Omega$ is an arbitrary region of the $(q, r)$ parameter space. We now want to denote $\mathcal{F}$ as the force applied by the fiber segments in $\mathcal{S}$ to the fluid. There is an additional force from the fibers from the tension $T$. Since the total force acting on $\mathcal{S}$ has to be 0, since our fibers are massless, we can write the following force balancing equation.

$$0 = -\mathcal{F} + \int_\Omega (T\tau) dq dr |_{s=s_1}^{s=s_2}.$$

To get a more complete understanding of the force applied to the fluid by the fibers we can rewrite this equation as:

$$\mathcal{F} = \int_{s_1}^{s_2} \int_\Omega \frac{-}{s} (T\tau) dq dr ds.$$

We now have an expression for the force being applied to the fluid, but the right hand side of the equation is with respect to the Legrangian frame for the fiber points. We now want to define a Legrangian force from the right hand side of the equation

$$\mathbf{f} = \frac{-}{s} (T\tau)$$

Here $\mathbf{f}$ is the density of the force applied by the fibers to the surrounding fluid. We now need a relation between the forces in cartesian coordinates and the force in Lagrangian coordinates, thus

67

we require a vector field $\mathbf{F}(\mathbf{x}, t)$ such that we have the following relation:

$$\int_V \mathbf{F}(\mathbf{x}, t) d\mathbf{x} = \int_{\mathbf{X}^{-1}(V,t)} \mathbf{f}(q, r, s, t) dq dr ds.$$

For these equations $V$ is an arbitrary region in the fluid, or the physical space we are considering and $\mathbf{X}^{-1}(V, t) = [(q, r, s) : \mathbf{X}(q, r, st) \in V]$. This relation can be achieved if we define $\mathbf{F}$ as:

$$\mathbf{F}(\mathbf{x}, t) = \int \mathbf{f}(q, r, s, t) \delta(\mathbf{x} - \mathbf{X}(q, r, s, t)) dq dr ds.$$

Now that we have a relations which ties the forces on the fluid to the forces generated by the elastic properties of the fibers, we can write out the full set of fluid-structure interaction equations.

$$\rho \frac{D\mathbf{u}}{Dt} = -\nabla p + \rho \mathbf{g} + \mu \nabla^2 \mathbf{u} + \mathbf{F} \tag{A.9}$$

$$\nabla \cdot \mathbf{u} = 0 \tag{A.10}$$

$$\mathbf{F}(\mathbf{x}, t) = \int \mathbf{f}(q, r, s, t) \delta(\mathbf{x} - \mathbf{X}(q, r, s, t)) dq dr ds. \tag{A.11}$$

$$\frac{\mathbf{X}(q, r, s, t)}{t} = \mathbf{u}(\mathbf{X}(q, r, s, t), t) \tag{A.12}$$

$$= \int \mathbf{u}(\mathbf{x}, t) \delta(\mathbf{x} - \mathbf{X}(q, r, s, t)) d\mathbf{x}. \tag{A.13}$$

$$\mathbf{f} = \frac{}{s}(T\tau). \tag{A.14}$$

$$T = \sigma(|\mathbf{X}/s|; q, r, s, t). \tag{A.15}$$

$$\tau = \frac{\mathbf{X}/s}{|\mathbf{X}/s|}. \tag{A.16}$$

Equations 14-16 are the equations which contain the information about the fiber properties. Equations 12-13 are the interaction equations which describe how the Lagrangian coordinate described fiber equations relate to the eulerian frame description of the fluid. Equations 10-11 are the standard incompressible Navier-Stokes s derived above.

The standard fluid equations are in Eulerian form, meaning $\mathbf{x} = (x_1, x_2, x_3)$. Variables described with this frame are the fluid velocity: $u(\mathbf{x}, t)$ the fluid pressure: $p(\mathbf{x}, t)$ and the Eulerian fiber force

density: $\mathbf{F}(\mathbf{x}, t)$. This force density is the $\mathbf{F}$ found in the fluid equations.

The fiber equations are described with a moving attached set of variables $(q, r, s, t)$. each triple: $(q, r, s)$ describes a point of the fibers, and each pair: $(q, r)$ describes an entire fiber. This is known as a Lagrangian description of the fluid. The unknown variables in these equations are the fiber tension: $T(q, r, s, t)$, the fiber force density: $\mathbf{f}(q, r, s, t)$, the fiber configuration: $\mathbf{X}(q, r, s, t)$ and the unit tangent, $\tau$, to the fibers which can be found from the fiber configuration. If we are given the tension and configuration of the fibers we can derive the fiber force density by plugging equations 15 and 16 into equation 14. Note that since the movement of the fibers is unknown equations 12-13 is effectively a no slip boundary condition. It merely states that the fibers move at the local fluid velocity, it doesn't add any restrictions to the fluid.

## A.5 Numerical Method

### A.5.1 Discretized Lagrangian Fibers

Now that we have the equations of motion for the fluid-structure interaction we can begin to discuss how to solve this numerically. First thing we want to define is that for a $\Delta t$ time step we will denote

$$\mathbf{X}^n(q, r, s) = \mathbf{X}(q, r, s, n\Delta t).$$

Or the nth time step in our scheme for a descritized time stepping method. We also have a discrete collection of fibers: $(q, r) = (k\Delta q, l\Delta r), k, l \in \mathbb{N}$. Each fiber has a discrete number of points: $s = m\Delta s, s \in \mathbb{N}$. We also want to define the tension and tangent vectors at half integer points given by $s = (m + \frac{1}{2})\Delta s$. We can now define a destritized version of the s derivative as follows:

$$(\mathcal{D}_s \phi)(s) = \frac{\phi(s + \frac{\Delta s}{2}) - \phi(s - \frac{\Delta s}{2})}{\Delta s}$$

This denotes a centered difference scheme which is second order in approximating the derivative. We can now define a descritized version of the tension and tangent vectors:

$$T^n = \sigma(|\mathcal{D}_s \mathbf{X}^n|; q, r, s, n\Delta t)$$
$$\tau^n = \frac{\mathcal{D}_s \mathbf{X}^n}{|\mathcal{D}_s \mathbf{X}^n|}$$

We can now get a representation of the force that the fibers are generating. Using the equations derived above we have a form for the force in terms of the tension of the fiber configuration and the unit tangent. Using this definition we will place out discretize tension and tangent into the equation to get a numerical version of the force:$\mathbf{f}^n = \mathcal{D}_s(T^n \tau^n)$. Note that all of this framework is to get discrete approximations to the fiber equations. We have descritized time and the point describing the configuration of the fibers.

### A.5.2   Discretized Fluid Equations

Now that we have the framework in place for the lagrangian fibers we can now build up the tools we need to numerically solve our fluid equations. We want to begin by define our fluid velocity and pressure on a lattice defined to be $\mathbf{x} = \mathbf{j}h; \mathbf{j} = (j_1, j_2, j_3)$. for each j being an integer value. We now want to calculate the force field generated from the elastic fibers which is influencing the fluid motion. We do this by referring back to our interaction equations. We have a continuous formula for our force spreading and since integration is really a limit of partial sums we can descritize the integral and get our numerical force spreading.

$$\hat{\mathcal{F}}^n(\mathbf{x}) = \sum_{q,r,s} \mathbf{f}^n(q, r, s)\delta_h(\mathbf{x} - \mathbf{X}^n(q, r, s))\Delta q \Delta r \Delta s.$$

Here the summation, $\sum_{q,r,s}$ is a sum over our discrete lagrangian points: $(q, r, s) = (k\Delta q, l\Delta r, m\Delta s)$.

Now that we have a forcing term we can write out the discretized navier-stokes equations:

$$\rho\left(\frac{\mathbf{u}^{n+1} - \mathbf{u}^n}{\Delta t} + \sum_{\alpha=1}^{3} u_\alpha^n \mathcal{D}_\alpha^\pm \mathbf{u}^n\right) - \hat{\mathcal{D}}^0 p^{n+1} = \mu\sum_\alpha \mathcal{D}_\alpha^+ \mathcal{D}_\alpha^- \mathbf{u}^{n+1} + \hat{\mathcal{F}}^n$$

$$\hat{\mathcal{D}}^0 \cdot \mathbf{u}^{n+1} = 0.$$

Note here that $\hat{\mathcal{D}}^0$ is the central difference approximation to the differential operator $\nabla$. We can define it as follows:

$$\hat{\mathcal{D}}^0 = (\mathcal{D}_1^0, \mathcal{D}_2^0, \mathcal{D}_3^0).$$

Where for a given function of our Eulerian domain we can generate an approximation to its derivative.

$$(\mathcal{D}_\alpha^0 \phi)(\mathbf{x}) = \frac{\phi(\mathbf{x} + h\mathbf{e}_\alpha) - \phi(\mathbf{x} - h\mathbf{e}_\alpha)}{2h}$$

Here $\mathbf{e}_\alpha = (\mathbf{e}_1, \mathbf{e}_2, \mathbf{e}_3)$ standard basis of $\Re^3$. We also need to define the foreword and backward difference operators:

$$(\mathcal{D}_\alpha^+ \phi)(\mathbf{x} = \frac{\phi(\mathbf{x} + h\mathbf{e}_\alpha) - \phi(\mathbf{x})}{h}$$
$$(\mathcal{D}_\alpha^- \phi)(\mathbf{x} = \frac{\phi(\mathbf{x}) - \phi(\mathbf{x} - h\mathbf{e}_\alpha)}{h}$$

These operators approximate the derivatives $\frac{}{x_\alpha}$, found in our fluid equations. Also note that everywhere $\alpha = 1, 2, 3$. Using these forward and backward difference routines we can obtain an approximation to the laplacian operator.

$$\sum_{\alpha=1}^{3} \mathcal{D}_\alpha^+ \mathcal{D}_\alpha^-$$

As well as an approximation to advection term $\mathbf{u} \cdot \nabla$:

$$\sum_{\alpha=1}^{3} u_\alpha \mathcal{D}_\alpha^\pm.$$

Here the term contained in the sum stands for:

$$u_\alpha \mathcal{D}_\alpha^\pm = \begin{cases} u_\alpha \mathcal{D}_\alpha^- & u_{\mathbb{A}} < 0 \\ \\ u_\alpha \mathcal{D}_\alpha^+ & u_{\mathbb{A}} > 0 \end{cases} \qquad (\text{A.17})$$

We can now discuss solving the discretized form of the Navier Stokes equations. For this paper we will discuss solving using Fourier methods, although there are other ways to numerically solve the Navier-Stokes equations. The ultimate goal is: given the forces applied to the fluid from the immersed boundary, solve the N-S equations for $(u_{n+1}, p_{n+1})$. First step is to rewrite the equations as:

$$(\mathcal{I} - \frac{\mu \Delta t}{\rho} \sum_{\alpha=1}^{3} \mathcal{D}_{\mathbb{A}}^+ \mathcal{D}_{\mathbb{A}}^-) \mathbf{u}^{n+1} + \frac{\Delta t}{\rho} \hat{\mathcal{D}}^0 p^{n+1} = \mathbf{v}^{n+1} \qquad (\text{A.18})$$

$$\hat{\mathcal{D}}^0 \cdot \mathbf{u}^{n+1} = 0 \qquad (\text{A.19})$$

Here we define $\mathbf{v}$ to be:

$$\mathbf{v}^n = \mathbf{u}^n - \frac{\Delta t}{\rho} \sum_{\alpha=1}^{3} u_{\mathbb{A}}^n \mathcal{D}_\alpha^\pm \mathbf{u}^n + \frac{\Delta t}{\rho} \mathbf{F}^n. \qquad (\text{A.20})$$

After written in this form we can take the Fourier transform of these discretized equations. We first need to compute a discrete form for our operators:

$$\hat{\mathcal{D}}_\alpha^- \hat{\mathcal{D}}_\alpha^+ = \frac{-4}{h^2} \sin\left(\frac{\pi k_\alpha}{N}\right), \qquad (\text{A.21})$$

$$\hat{\mathcal{D}}^0 = \frac{i}{h} \sin\left(\frac{2\pi}{N} \mathbf{k}\right). \qquad (\text{A.22})$$

Note that a hat now denotes the fourier transform. Once we have the transform of the numerical

operators we can then take a transform of $\mathbf{v}^n$ and solve for our pressure and velocity terms, giving us:

$$\hat{\mathbf{u}}^{n+1}(\mathbf{k}) = \frac{\hat{\mathbf{v}}^n(k) - \frac{i\Delta t}{\rho h}\left(\sin\left(\frac{2\pi}{N}\mathbf{k}\right)\right)\hat{p}^{n+1}(\mathbf{k})}{A(\mathbf{k})}, \tag{A.23}$$

$$\hat{p}^{n+1}(\mathbf{k}) = \frac{\frac{i}{h}\left(\sin\left(\frac{2\pi}{N}\mathbf{k}\right)\right) \cdot \hat{\mathbf{v}}^n(\mathbf{k})}{\frac{\Delta t}{\rho h^2}\left(\sin\left(\frac{2\pi}{N}\mathbf{k}\right)\right) \cdot \left(\sin\left(\frac{2\pi}{N}\mathbf{k}\right)\right)}. \tag{A.24}$$

Now that we have a fourier transformed formulation for $\{\hat{\mathbf{u}}^{n+1}, \hat{p}^{n+1}\}$ we can take an inverse transform to to get our updated fluid velocity and pressure: $\{u^{n+1}, p^{n+1}\}$. Once obtained we can use this to update the location of the boundary:

$$\frac{\mathbf{X}^{n+1}(q,r,s) - \mathbf{X}^n(q,r,s)}{\Delta t} = \sum_{\mathbf{x}} \mathbf{u}^{n+1}\delta_h(\mathbf{x} - \mathbf{X}^n(q,r,s))h^3, \tag{A.25}$$

which is a discretized version of equation 12. This formulation then allows us to update our boundary position based upon the local fluid velocity. This will enforce a no-slip condition along the boundary. Once we've obtained $\mathbf{u}^{n+1}$ and $\mathbf{X}^{n+1}(q,r,s)$ we have completed one time step of the immersed boundary method. Details of the actual code implementation will be given in the proceeding appendix.

# APPENDIX B: PYTHON IMMERSED BOUNDARY SOLVER

In this section we will detail the code used to compute the immersed boundary. All code will be in python and will be a good representation of the actual implementation of the algorithm. We will not include minor details but instead include the main routine and the fluid solver. The FFT used in this code is the built in Numpy implementation of the FFT and can be seen to be similar to the Matlab version.

## B.1    Main routine

Here is a formulation of main routine for a python FFT fluid solver:

```
############################################################
#
# This is a two dimensional immersed boundary method code.
# The fluid solver uses an fft, so the domain
# must be periodic. New fluid solvers will be added as it gets updated.
# Right now the boundary is moved
# via target points (springs and beams forthcoming),
#geometry of target points can be specified.
# Preformance testing and error testing has been
#completed and documented (check documentation).
# this is a first order method near the boundary
# and a second order method away from the boundary.
# to run:
#     Be sure that a .txt file containing your boundary points is present,
#     then simply type:
#     python immersed_boundary.py
#
# movement of the boundary can be manipulated
# in the move_ib function within the code (see documentation)
```

```python
# a rubber band example, and a moving rod

# are both simple examples included in documentation.

#

# Written by: Austin Baird, UNC Chapel Hill.

#Part of a PhD thesis work on immersed boundary and pumping

# applications.

#############################################################


if __name__ == "__main__":


#############################################################

# Initialize parameters needed for computation

# dt, meshsize and other things may be changed here

#############################################################

    #import fluid_constants as f

    #ptime = 0

    k = 0  # frame number


#############################################################

    # Array initialization

#############################################################


    press = np.zeros((f.M,f.N))   #pressure size NXM matrix

    u = np.zeros((f.M,f.N))   #x-directed velocity

    v = np.zeros((f.M,f.N))   #y_directed velocity

    f1 = np.zeros((f.M,f.N))   #force in x_direction

    f2 = np.zeros((f.M,f.N))

    t = np.zeros(f.T)   #number of time steps

    mag = np.zeros((f.M,f.N)) #magnitude of velocity vector at each grid point
```

```python
#---------------------Precomputed matrices from paper--------------------#


w1 = np.zeros((f.M,f.N))

w2 = np.zeros((f.M,f.N))

a = np.zeros((f.M,f.N))

b = np.zeros((f.M,f.N))

c = np.zeros((f.M,f.N))

d = np.zeros((f.M,f.N))


#--------------------Matricies to store fourier transforms----------------#


uft = np.zeros((f.M,f.N))

vft = np.zeros((f.M,f.N))

pft = np.zeros((f.M,f.N))




#--------------------Cartesian coordinate matrices------------------------#


xcoord = np.zeros((f.M,f.N))   #holds the x-value in the (i,j) position

ycoord = np.zeros((f.M,f.N))   #holds the y-value in the (i,j) position

vort = np.zeros((f.M,f.N))
#--------------------Boundary arrays and tartget arrays-------------------#



b1 = np.zeros((f.Q,1))

b2 = np.zeros((f.Q,1))

b1t = np.zeros((f.Q,1))   #target points for the immersed boundary

b2t = np.zeros((f.Q,1))


fb1 = np.zeros((f.Q,1))   #storing forces for each boundary point
```

```python
    fb2 = np.zeros((f.Q,1))




    ###########################################################
    # Creating directories to store the output files
    ###########################################################


    os.makedirs("./velu")

    os.makedirs("./velv")

    os.makedirs("./pressure")

    os.makedirs("./vorticity")

    os.makedirs("./forcesx")

    os.makedirs("./forcesy")



    ###########################################################
    #Store cartesian values into array, for plotting
    ###########################################################


    for i in range(f.M):
        for j in range(f.N):
            xcoord[i,j] = j*f.dx
            ycoord[i,j] = i*f.dx


    #print xcoord



    ###########################################################
    #Precompute matrices used to calculate u_hat, p_hat
    #from Peskin and McQueen
    # 1996 eqns 14.52 and 14.51
    ###########################################################
```

```
for i in range(f.M):
    for j in range(f.N):
        if i==0 and j==0 or i==0 and j==f.N/2:
            a[i,j]==0
            b[i,j]==0
            c[i,j]==0
        elif i==f.M/2 and j==0 or i == f.M/2 and j==f.N/2:
            a[i,j] = 0
            b[i,j] = 0
            c[i,j] = 0


        else:
            a[i,j] = np.sin(2*np.pi*i/f.M)*np.sin(2*np.pi*i/f.M)/
            ((np.sin(2*np.pi*i/f.M)*np.sin(2*np.pi*i/f.M)+
            np.sin(2*np.pi*j/f.N)*
            np.sin(2*np.pi*j/f.N)))
            b[i,j] = np.sin(2*np.pi*i/f.M)*np.sin(2*np.pi*j/f.N)/
            ((np.sin(2*np.pi*i/f.M)*np.sin(2*np.pi*i/f.M)+
            np.sin(2*np.pi*j/f.N)*
            np.sin(2*np.pi*j/f.N)))
            c[i,j] = np.sin(2*np.pi*j/f.N)*np.sin(2*np.pi*j/f.N)/
            ((np.sin(2*np.pi*i/f.M)*np.sin(2*np.pi*i/f.M)+
            np.sin(2*np.pi*j/f.N)*
            np.sin(2*np.pi*j/f.N)))


for i in range(f.M):
    for j in range(f.N):
        d[i,j] = 1/(1+(4*f.nu*f.dt/(f.dx*f.dx))*np.sin(np.pi*i/f.M)*
        np.sin(np.pi*i/f.M)+np.sin(np.pi*j/f.N)*np.sin(np.pi*j/f.N))
```

```python
    #print d.shape, a.shape, b.shape, c.shape
##############################################################
    #To follow the matlab code I will be setting the
    #inital boundary here
    ###############################################################


    #boudary points for a rod


    for i in range(f.Q):
        b1[i,0] = f.width/2
        b2[i,0] = (f.width/4) + i*f.ds


    #Target points are just the boundary points


    for i in range(f.Q):
        b1t[i,0] = f.width/2
        b2t[i,0] = (f.width/4) + i*f.ds


############################################################
    # Time stepping routine (this is the main routine for IB method)
############################################################


    while f.time < f.time_final:
        #zero forces
        f1 = np.zeros((f.M,f.N))
        f2 = np.zeros((f.M,f.N))
        fb1 = np.zeros((f.Q,1))
        fb2 = np.zeros((f.Q,1))
```

```
b1t, b2t = moveIB(b1t,b2t,f.Q)



#calculate forces from the boundary being applied to the fluid:



fb1, fb2 = target_force(b1,b2,b1t,b2t,fb1,fb2,f.stiff,f.Q)



#spread the force to the fluid:



f1, f2 = forcespread(b1,b2,fb1,fb2,f1,f2,f.Q)



# Now solve for the new velocity and pressure:



u,v,press = fluidsolve(a,b,c,d,f1,f2,u,v,uft,vft,w1,w2,pft,f.time,press)



# Move boundary at the local fluid velocity



b1, b2 = move_boundary(b1,b2,f.Q,u,v)



# now we need to output the data:
#print u, v vorticity, pressure, forces:
if f.time>f.ptime:
    vort = vorticity(u,v,vort)
    record(u,v,vort,press,f1,f2,b1,b2,k)



    f.ptime = f.graphtime + f.ptime    #



f.time = f.time + f.dt    #update time
```

This algorithm follows the formulation of the problem introduced in the first appendix. The FFT fluid solver is a function which is detailed here:

```
##############################################################
# This file takes in the forces from the boundary and updates
# pressure (press) and fluid velocity (u,v) accordingly
##############################################################


def fluidsolve(a,b,c,d,f1,f2,u,v,uft,vft,w1,w2,pft,time,press):
    #import fluid_constants as f


    # First thing to do is to calculate w1, w2 and take the fft of them
    w1, w2 = makew(w1,w2,f1,f2,u,v)


    # After calculating w1,w2 we can now begin taking the fft of our arrays
    w1ft = np.fft.fft2(w1)
    w2ft = np.fft.fft2(w2)
    a = a + 0j
    b = b + 0j
    c = c + 0j
    d = d + 0j
    uft = uft + 0j
    vft = vft + 0j


    # calculate uft, vft from w's, from Peskin paper
    uft = (w1ft - (a*w1ft + b*w2ft))*d
    vft = (w2ft - (b*w1ft + c*w2ft))*d
```

```python
        pft = pft + 0j


        for i in range(f.M):
            for j in range(f.N):
                if i==0 and j==0 or i==0 and j==f.N/2:
                    pft[i,j] = 0
                elif i==f.M/2 and j==0 or i ==f.M/2 and j==f.N/2:
                    pft[i,j] = 0
                else:
                    pft[i,j] = ((f.p*f.dx/f.dt)*(np.sin(2*np.pi*i/f.M)*
                    np.imag(w1ft[i,j])
                    + np.sin(2*np.pi*(j)/f.N)*np.imag(w2ft[i,j])))/
                    ((np.sin(2*np.pi*i/f.N)*np.sin(2*np.pi*i/f.M)) +
                     np.sin(2*np.pi*j/f.N)*np.sin(2*np.pi*j/f.N))


                    pft[i,j] = pft[i,j] - np.sqrt(np.complex(-1))*
                    ((f.p*f.dx/f.dt)*(np.sin(2*np.pi*i/f.M)*
                    np.real(w1ft[i,j]) + np.sin(2*np.pi*(j)/f.N)*
                    np.real(w2ft[i,j])))/((np.sin(2*np.pi*i/f.N)*
                    np.sin(2*np.pi*i/f.M)) +
                    np.sin(2*np.pi*j/f.N)*np.sin(2*np.pi*j/f.N))



# We can now take the inverse transform to get u,v, and press


    u = np.fft.ifft2(uft)
    v = np.fft.ifft2(vft)
    press = np.fft.ifft2(pft)
```

```
u = np.real(u)

v = np.real(v)

press = np.real(press)


return u, v, press
```

Details of other functions are straight forward and follow from the work in the previous appendix.

## REFERENCES

[1] T. King A. Baird and L. A. Miller, *Numerical study of scaling effects in peristalsis and dynamic suction pumping*, Proceedings of the AMS Special Session on Biological Fluid Dynamics: Modeling, Computations, and Applications (submitted).

[2] D. Auerbach, W. Moehring, and M. Moser, *An analytic approach to the liebau problem of valveless pumping*, Cardiovascular Engineering: An International Journal **4** (2004), no. 2, 201–207.

[3] T. Bringley, S. Childress, N. Vandenberghe, and J. Zhang, *An experimental investigation and a simple model of a valveless pump*, Physics of Fluids **20** (2008), 033602.

[4] W. W. Burggren, *What is the Purpose of the Embryonic Heart Beat? or How Facts Can Ultimately Prevail over Physiological Dogma*, Physiological and Biochemical Zoology **77** (2004), 333–345.

[5] D. S. Mathioulakis C. G. Manopoulos and S. G. Tsangaris, *One-dimensional model of valveless pumping in a closed loop and a numerical solution*, Physics of Fluids (1994-present) **18** (2006), no. 1, 017106.

[6] H. D. Ceniceros and J. E. Fisher, *Peristaltic pumping of a viscoelastic fluid at high occlusion ratios and large weissenberg numbers*, Journal of Non-Newtonian Fluid Mechanics **171** (2012), 31–41.

[7] S. E. Fraser-M. E. Dickinson E. A. V. Jones, M. H. Baron, *Measuring hemodynamic changes during mammalian development*, American Journal of Physiology-Heart and Circulatory Physiology **287** (2004), no. 4, H1561–H1569.

[8] T. R. Elliott, *The innervation of the bladder and urethra*, The Journal of physiology **35** (1907), no. 5-6, 367.

[9] L. J. Fauci, *Peristaltic pumping of solid particles*, Computers and Fluids **21** (1992), no. 4, 583 – 598.

[10] R. FitzHugh, *Impulses and physiological states in theoretical models of nerve membrane*, Biophysical journal **1** (1961), no. 6, 445–466.

[11] A. S. Forouhar, M. Liebling, A. Hickerson, A. Nasiraei-Moghaddam, H. Tsai, J. R. Hove, S. E. Fraser, M. E. Dickinson, and M. Gharib, *The embryonic vertebrate heart tube is a dynamic suction pump*, Science **312** (2006), no. 5774, 751–753.

[12] V. Hamburger and H. L. Hamilton, *A series of normal stages in the development of the chick embryo*, Journal of morphology **88** (1951), no. 1, 49–92.

[13] A. I. Hickerson, D. Rinderknecht, and M. Gharib, *Experimental study of the behavior of a valveless impedance pump*, Experiments in fluids **38** (2005), no. 4, 534–540.

[14] A. L. Hodgkin and A. F. Huxley, *Propagation of electrical signals along giant nerve fibres*, Proceedings of the Royal Society of London. Series B, Biological Sciences (1952), 177–183.

[15] A. Iwaniec I.H. Hickerson and M. Gharib, *On the resonance of a pliant tube as a mechanism for valveless pumping*, Journal of Fluid Mechanics **555** (2006), 141–148.

[16] L Fauci J. Teran and M. Shelley, *Peristaltic pumping and irreversibility of a stokesian viscoelastic fluid*, Physics of Fluids **20** (2008), 073101.

[17] M. Y. Jaffrin and A. H. Shapiro, *Peristaltic pumping*, Annual Review of Fluid Mechanics **3** (1971), no. 1, 13–37.

[18] A. S. Forouhar G. Acevedo-Bolton S. E. Fraser M. Gharib J.R Hove, R. W. Köster, *Intracardiac fluid forces are an essential epigenetic factor for embryonic cardiogenesis*, Nature **421** (2003), no. 6919, 172–177.

[19] E. Jung, S. Lim, W. Lee, and S. Lee, *Computational models of valveless pumping using the immersed boundary method*, Computer Methods in Applied Mechanics and Engineering **197** (2008), 2329–2339.

[20] E. Jung and C. Peskin, *Two-dimensional simulations of valveless pumping using the immersed boundary method*, SIAM Journal on Scientific Computing **23** (2001), no. 1, 19–45.

[21] M. E. Kriebel, *Conduction velocity and intracellular action potentials of the tunicate heart*, The Journal of General Physiology **50** (1967), no. 8, 2097–2107.

[22] I. Avrahami L. Loumes and M. Gharib, *Resonant pumping in a multilayer impedance pump*, Physics of Fluids (1994-present) **20** (2008), no. 2, 023103.

[23] D. Lee, H. C. Yoon, and J. S. Ko, *Fabrication and characterization of a bidirectional valveless peristaltic micropump and its application to a flow-type immunoanalysis*, Sensors and Actuators B: Chemical **103** (2004), no. 12, 409 – 415, ¡ce:title¿The 17th Euopean Conference on Solid-State Transducers, University of Minho, Guimares, Portugal, September 21-24, 2003¡/ce:title¿.

[24] G. Liebau, *ber ein ventilloses pumpprinzip*, Naturwissenschaften **41** (1954), 327–327 (German).

[25] G Liebau, *Die stromungsprinzipien des herzens*, Z. Kreislaufforsch **44** (1955), 677.

[26] _____, *Die bedeutung der tragheitskrafte fur die dynamik des blutkreislaufs*, Z. Kreislaufforsch **46** (1957), 428.

[27] L. A. Miller and C. S. Peskin, *Flexible clap and fling in tiny insect flight*, Journal of Experimental Biology **212** (2009), no. 19, 3076–3090.

[28] R. Mittal, *Locomotion with flexible propulsors: Ii. computational modeling of pectoral fin swimming in sunfish*, Bioinspir. Biomim. **1** (2006), S35–S41.

[29] A. F. M. Moorman and V. M. Christoffels, *Cardiac chamber formation: Development, genes, and evolution*, Physiol Rev **83** (2003), 1223–1267.

[30] Johnny Tom Ottesen, *Valveless pumping in a fluid-filled closed elastic tube-system: one-dimensional theory with experimental validation*, Journal of mathematical biology **46** (2003), no. 4, 309–332.

[31] C. S. Peskin, *The immersed boundary method*, Acta Numerica **11** (2002), 479–517.

[32] C. S. Peskin and D. M. McQueen, *Fluid dynamics of the heart and its valves*, Case Studies in Mathematical Modeling: Ecology, Physiology, and Cell Biology (H. G. Othmer, F. R. Adler, M. A. Lewis, and J. C. Dallon, eds.), Prentice-Hall, New Jersey, 2nd ed., 1996.

[33] D. J. Randall and P. S. Davie, *The hearts of urochordates and cephalochordates*, Hearts and heart-like organs **1** (1980), 41–59.

[34] A. Santhanakrishnan and L. A. Miller, *The fluid dynamics of heart development*, (2011), *Cell Biochem. Biophys.* DOI: 10.1007/s12013-011-9158-8.

[35] A. Santhanakrishnan, N. Nguyen, J. G. Cox, and L. A. Miller, *Flow within models of the vertebrate embryonic heart*, Journal of Theoretical Biology **259** (2009), no. 3, 449 – 461.

[36] D. J. Sugarbaker, S. Rattan, and R. K. Goyal, *Mechanical and electrical activity of esophageal smooth muscle during peristalsis*, American Journal of Physiology-Gastrointestinal and Liver Physiology **246** (1984), no. 2, G145–G150.

[37] J. Teran, L. Fauci, and M. Shelley, *Viscoelastic fluid response can increase the speed and efficiency of a free swimmer*, Physical review letters **104** (2010), no. 3, 38101.

[38] E. D. Tytell, C. Hsu, T. L. Williams, A. H. Cohen, and L. J. Fauci, *Interactions between internal forces, body stiffness, and fluid environment in a neuromechanical model of lamprey swimming*, Proceedings of the National Academy of Sciences **107** (2010), no. 46, 19832–19837.

[39] J. R. Womersley, *Method for the calculation of velocity, rate of flow and viscous drag in arteries when the pressure gradient is known*, The Journal of physiology **127** (1955), no. 3, 553–563.